2015

Nanoparticle-assisted laser desorption/ionization mass spectrometry: novel sample preparation methods and nanoparticle screening for plant metabolite imaging

Gargey B. Yagnik
Iowa State University

Nanoparticle-assisted laser desorption/ionization mass spectrometry: Novel sample preparation methods and nanoparticle screening for plant metabolite imaging

by

Gargey B. Yagnik

A dissertation submitted to the graduate faculty

in partial fulfillment of the requirements for the degree of

DOCTOR OF PHILOSOPHY

Major: Analytical Chemistry

Program of Study Committee:
Young-Jin Lee, Major Professor
Robert S. Houk
Patricia Ann Thiel
Javier Vela-Becerra
Basil J. Nikolau

Iowa State University

Ames, Iowa

2015

TABLE OF CONTENTS

ACKNOWLEDGMENTS

First of all I would like to thank Dr. Young-Jin Lee for enrolling me as a part of his research team. I am truly thankful to him for his guidance, direction and generosity throughout my thesis research work. I would also like to acknowledge my committee members; Dr. Sam Houk, Dr. Patricia Thiel, Dr. Javier Vela, Dr. Basil Nikolau, and Dr. Ning Fang for their guidance and input during my time at Iowa State University. I am also grateful to Dr. Reuben J. Peters and Dr. Bing Yang for their support and guidance.

I am grateful to a number of individuals who helped to make this work possible. Many thanks to all the members of the Lee laboratory, especially Dr. Adam T. Klein, Adam D. Feenstra, Maria E. Dueñas and Rebecca Hansen for their ideas, support and guidance throughout my research work. I am especially grateful to former group member Dr. Andrew R. Korte for his ideas and continuous help to resolve scientific problems. I am deeply thankful to Dr. Feimeng Zhou, my master's adviser, for giving me my first research opportunity in the USA and to Dr. Carlos Gutierrez for their scientific guidance at California State University, Los Angeles. This research work was supported by the U.S. Department of Energy (DOE), Office of Basic Energy Sciences at the Ames Laboratory under contract number DE-AC02-07CH11358.

Finally, I would like to thank my family and friends for their support and encouragement; especially, my aunt for her continuous support throughout my education in the USA. I am very grateful to my mother and my wife for their continued encouragement and support throughout my education.

ABSTRACT

The main goal of the presented research is development of nanoparticle based matrix-assisted laser desorption ionization-mass spectrometry (MALDI-MS). This dissertation includes the application of previously developed data acquisition methods, development of novel sample preparation methods, application and comparison of novel nanoparticle matrices, and comparison of two nanoparticle matrix application methods for MALDI-MS and MALDI-MS imaging. Chapter 1 presents background information about MALDI-MS and a general workflow for MALDI-MS imaging experiments. Chapter 6 provides a summary of the presented work and possible future directions.

Chapter 2 describes a “multiplex” MALDI-MS imaging technique applied to study latent human fingerprints. In this study, we applied previously developed multiplex data acquisition techniques for the detection of endogenous and exogenous compounds with structural information in a single MALDI-MS imaging experiment. This study also depicts the importance of the sublimation matrix application method for analysis of very delicate samples such as latent fingerprints.

Chapter 3 presents the development of novel sample preparation methods for nanoparticle-assisted laser desorption/ionization-mass spectrometry -mass spectrometry (NALDI-MS) imaging of metabolites in plant tissues. In this chapter, we developed a novel fracturing method for MALDI-MS/ NALDI-MS imaging of rice leaf to study a plant-pathogen interactions. We successfully detected and imaged diterpenoids produced against the *Xanthomonas oryzae* pv. *oryzae* infection in rice leaves.

Chapter 4 is focused on novel nanoparticle (NP) matrix development for NALDI-MS of low-molecular weight plant metabolites. This large-scale NP screening was

inspired by the success of the metabolite detection/imaging in Chapter 3. In this work, we studied three different classes of NPs for desorption/ionization of a wide variety of plant metabolites and sought to shed some light on the NALDI mechanism.

Chapter 5 is a further extension of the study in Chapter 4, in which we compare two NP application methods for efficiency of desorption/ionization of plant metabolites and homogeneity of application. We compare application of a nanoparticle suspension by oscillating capillary nebulizer and solvent-free sputter coating of metal NPs. The work presented in Chapters 4 and 5 will be helpful for development of novel matrices for analysis and imaging of low-molecular weight metabolites that are difficult to ionize using traditional MALDI-MS matrices.

CHAPTER 1

MALDI-MS INTRODUCTION

Background

Mass spectrometric imaging is becoming an important technique for detection of chemical species with spatial resolution in biological samples. Matrix-assisted laser desorption/ionization mass spectrometry (MALDI-MS) enables sensitive detection and identification of a variety of chemical species from biological samples. MALDI-MS as a mass spectrometric imaging (MALDI-MSI) tool combines these capabilities with spatially-resolved sampling. MALDI-MSI allows for the two-dimensional visualization of the spatial distribution of biomolecules without extraction, purification, separation, or labeling of analytes. MALDI-MSI is a unique imaging technique for non-target-specific discoveries, since analyte molecules are ablated, ionized, and detected directly from the tissue without labeling of any specific targets. MALDI-MSI has been employed to visualize distributions of numerous biomolecules including proteins, peptides, metabolites, amino acids, lipids, carbohydrates, and nucleotides in a variety of biological systems, various tissue types, and in diverse fields such as medicine, agriculture, biology, pharmacology, pathology and forensic science.[1-5]

This thesis describes efforts to develop new MALDI-MSI techniques for the analysis of several different sample types. First, we have demonstrated that MALDI-MSI can be utilized as a tool for detection and imaging of various endogenous and exogenous compounds in human latent fingerprints. For this study we have utilized a previously-developed in-parallel data acquisition methodology ("multiplex MS

imaging")[6] that allows for the collection of high-mass resolution MS and structurally informative MS/MS data in a single experiment. This work exhibits the usefulness of multiplex MS imaging to explore chemical markers in limited sample specimens such as latent fingerprints.[7]

In plants, metabolism can be significantly different even between adjacent cells and tissues; therefore, high-resolution MSI methodologies are of great interest.[8] In a typical MALDI-MSI experiment, a cryosectioned tissue is mounted on a MALDI target plate, matrix is applied, and the sample is subjected to analysis. In the case of some specific tissues like leaves, cryosectioning is very difficult. Therefore, we have adopted an imprinting method and developed a novel fracturing method for sample preparation and applied them, for the first time, to visualize internal metabolites of leaves by MALDI-MSI.[6] This study provided localized molecular information for the chemical processes occurring during plant-pest interactions. For detection and imaging of internal metabolites, we employed nanoparticle-assisted laser desorption/ionization-mass spectrometry imaging (NALDI-MSI). In this experiment, we detected low-molecular weight phytochemical metabolites produced by rice plants as a defense against *Xanthomonas oryzae* pv. *oryzae* bacterial infection and could visualize their spatial distribution in the tissue. We were also able to detect other common plant metabolites present in the leaves. [9-11]

MALDI-MS or -MSI experiments typically use a low-molecular weight organic compound as a matrix. These matrices give strong background signals in the low mass region (m/z < ~500) and can interfere with the analysis of small metabolite compounds. Additionally, low-molecular weight plant metabolites tend to show a variety of

functionalities, and optimal ionization of all potential metabolites of interest by a single matrix is difficult. For these reasons, there is great motivation to develop new MALDI-MS matrices for low-molecular weight compound analysis. One promising avenue of research is the use of inorganic nanoparticles as MALDI matrices[12]

For the development of new matrices and to better understand the NALDI mechanism for ionization of low-molecular weight plant metabolites, we have investigated three different classes of nanoparticles (NPs): carbon-based, metal, and metal oxide. In NALDI-MS, the energy transfer from NPs to analytes has been suggested to occur via a thermally-driven process.[13-15] In addition to internal energy transfer from NPs to analyte, alternative mechanisms such as phase transition/ destruction desorption and significant effects of surface properties on the mechanism have also been proposed for NALDI processes.[16] The NALDI processes are still not completely understood and in this study we attempted to shed some light on the NALDI mechanism.

Due to the complexity of the process and the wide variety of analytes of interest, an empirical study of several NP matrix candidates was needed. In this study, we have screened different NPs for the ability to ionize several different classes of low-molecular weight plant metabolites. This metabolite screening, combined with the physicochemical properties of NP materials and theoretical calculations based on these properties, helped us to understand the NALDI-MS ionization mechanism and select appropriate nanoparticle matrices to ionize specific classes of metabolites.

MALDI-MSI: General Workflow

The workflow of a typical MALDI-MSI experiment in this dissertation is illustrated in Figure 1, and a brief description of the procedures employed herein is provided below.[5] Any MALDI-MSI experiment starts with a biological question to be addressed. This leads to the type of biological system to be studied and type of samples. The sample types determine sample preparation and analytes of interest determine choice of matrices.

For imaging of human latent fingerprints (LFP), sample preparation consisted of collection of the LFP on glass slides. For the rice-bacteria interaction, we adopted an imprinting sample preparation method and developed a novel fracturing sample preparation method. For fracturing, a section of the harvested rice leaf was stuck to transparent packing tape. The tape with the leaf section was subjected to vacuum drying and was folded over to enclose the section of leaf between the two adhesive sides of the tape. The tape and leaf sandwich was then passed through a rolling mill to fracture the leaf section. Finally, the two ends of the packing tape were pulled open, leaving one surface on each side of the folded tape and exposing the interior tissue.

For LFP imaging, a traditional organic matrix was applied by sublimation; the matrix is heated under vacuum and allowed to deposit onto the sample. For NP matrices for screening and imaging, application can be accomplished by spraying. The NP suspension was sprayed onto samples using a homemade oscillating capillary nebulizer (OCN). For the screening comparison between sprayed and physical vapor deposited metal NPs, two methods were employed: (1) metal NP suspensions were

mixed with standard metabolite solutions and sprayed a homemade OCN and (2) metals were sputter coated on standards sprayed by OCN on a glass slide.

After matrix application, the sample was inserted into a linear ion trap-orbitrap mass spectrometer with a MALDI ion source. A series of points over the sample surface were irradiated in a raster fashion by a focused laser beam and at each of these points a mass spectrum was recorded and stored. After scanning a specific area, an image for a specific *m/z* could be constructed from the signal intensity for an ion of interest at each x-y position.

Dissertation Organization

There are a total of six chapters in this dissertation. Chapter 1, above, provides an overview of MSI and our studies to develop and apply novel data acquisition methods and sample preparation techniques, and apply previously unused NALDI-MS matrices for the analysis of plant metabolites. Chapters 2 and 3 are reproductions of papers published in peer-reviewed journals. Chapter 2 presents an application of a "multiplex MALDI-MSI" method to image and detect endogenous and exogenous low-molecular weight compounds in latent human figure prints while providing structural information. Chapter 3 demonstrates novel sample preparation methods and presents an application of these methods for better understanding plant-pathogen interactions. Chapter 4 is a manuscript under preparation, describing the development of novel nanoparticle matrices and an investigation of the NALDI-MS mechanism. Chapter 5 is an extension of our nanoparticle matrix development study. In Chapter 5, we have compared metal nanoparticles applied by suspension spray and solvent free sputter

coating for ionization of various classes of plant metabolites. Finally, Chapter 6 summarizes all work presented in this dissertation and outlines future directions for developments and applications of the described matrices and methodologies.

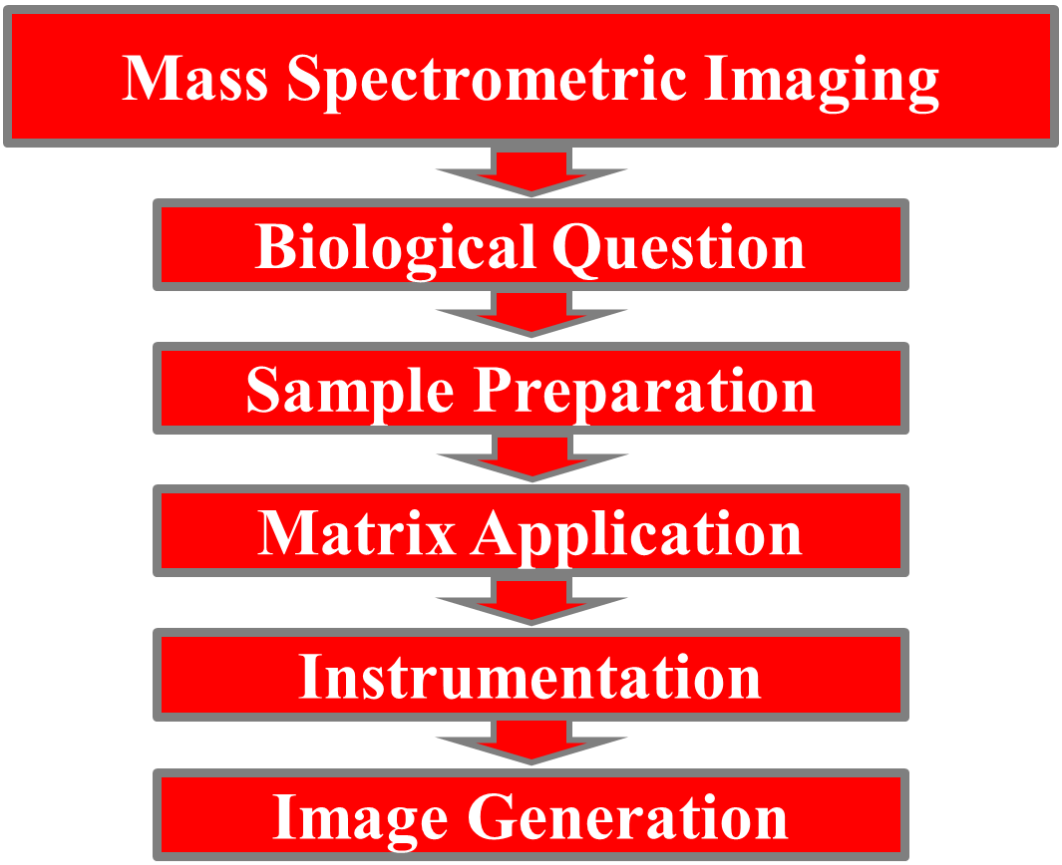

Figure 1: Flow chart of a MALDI-MSI experiment.[5]

CHAPTER 2

MULTIPLEX MASS SPECTROMETRY IMAGING FOR LATENT FINGERPRINTS

A paper published in *Journal of Mass Spectrometry*

J. Mass Spectrom., **2013**, 48, 100-104.
Reproduced by permission of John Wiley & Sons, Ltd.

Gargey B. Yagnik, Andrew R. Korte and Young Jin Lee

Abstract

We have previously developed in-parallel data acquisition of orbitrap mass spectrometry (MS) and ion trap MS and/or MS/MS scans for matrix-assisted laser desorption/ionization MS imaging (MSI) to obtain rich chemical information in less data acquisition time. In the present study, we demonstrate a novel application of this multiplex MSI methodology for latent fingerprints. In a single imaging experiment, we could obtain chemical images of various endogenous and exogenous compounds, along with simultaneous MS/MS images of a few selected compounds. This work confirms the usefulness of multiplex MSI to explore chemical markers when the sample specimen is very limited.

Introduction

Latent fingerprints (LFP) are deposits of sweat components in ridge and groove patterns, left after contact of human fingers with a surface.[17, 18] LFP are commonly used for personal identification purposes in forensic studies[19, 20] and access control.[21] LFP analysis has also been employed for medical diagnosis and drug metabolite

detection.[22, 23] Various techniques have been used for analyzing LFP including dusting with powders, spraying with reagent solutions for visual observation and spectroscopic techniques such as ultraviolet/visible,[24] fluorescence,[18] infrared [25] and Raman.[26] Mass spectrometry (MS) has been employed for analysis of sweat components from LFP.[27, 28] Compared to other LFP analysis techniques, MS methods offer the major advantage of chemically specific detection and identification of various endogenous compounds such as lipids and exogenous components from soaps, disinfectants, cosmetics, perfumes, drugs metabolites, and food residues in a single analysis. [20] The presence and absence of these compounds can be useful for forensic identification purposes[19, 20]and medical diagnostic and drug metabolite studies.[22, 23]

In recent years, MS imaging (MSI) has been used as a LFP imaging technique,[17, 24, 29-31] for forensic investigations, LFP left on different surfaces like walls, doors, windows, and objects can be lifted using CSI tape and transferred on microscope slides for MSI.[24] Successful identification of gender-specific biomarkers in volatile compounds of human sweat[32] and peptides and proteins on LFP[33] suggest the plausibility of MSI for forensic application. MSI has the additional advantage of providing chemical information about the sample with spatial resolution. Various ionization techniques such as matrix-assisted laser desorption/ionization MS (MALDI),[17, 24, 29] desorption electrospray ionization,[30] surface-assisted laser desorption ionization,[23] and secondary ion MS[31] have been applied for chemical imaging of LFP.

We have recently developed a multiplex MSI methodology utilizing a linear ion trap-orbitrap hybrid mass spectrometer.[34] In this approach, each MALDI raster step is composed of multiple smaller steps. While the ions produced from the first step are

being analyzed by the high mass resolution orbitrap mass analyzer, spectra from subsequent steps are acquired by the linear ion trap in either MS or MS/MS mode. Multiple ion trap MS scans in parallel to orbitrap MS scans allows 'high spatial resolution' MS images (in the linear ion trap) and 'high mass resolution' MS images (in the orbitrap), with significant time savings compared to using entirely orbitrap scans. When MS/MS scans are obtained in parallel to orbitrap scans instead of ion trap MS, structural isomers can be distinguished, and their distributions can be separately visualized, along with their high mass resolution chemical images.[34] More importantly, all these data can be acquired in a single imaging measurement, making the technique very useful when sample is limited.

Here, we present a novel application of multiplex MSI to LFP. Oftentimes, LFP left over in criminal scene are very limited. Therefore, it is desirable to obtain as much chemical information as possible from a single LFP. In this proof of concept experiment, we could successfully obtain chemical images of various endogenous and exogenous compounds along with structural information through MS/MSI.

Experimental

Materials and Sample Preparation

Verapamil hydrochloride (98 %) was purchased from Sigma-Aldrich (St. Louis, MO), and 2, 5-dihydroxybenzoic acid (DHB, 99 %) was purchased from Thermo Fisher Scientific (Waltham, MA, USA). The LFP was prepared by rubbing the thumb against the forehead and then in verapamil powder prior to deposition on glass microscope slides.[29] DHB matrix was applied by sublimation as described previously.[35]

MSI Data Acquisition

A linear ion trap-orbitrap mass spectrometer with MALDI ion source (MALDI LTQ-Orbitrap Discovery; Thermo Scientific, San Jose, CA, USA) was used for the current study. The instrument is modified to use an external frequency tripled, diode pumped Nd:YAG laser operating at 355 nm (UVFQ; Elforlight Ltd., Daventry, UK). A laser energy of about 2 mJ/pulse and 60 Hz repetition rate were used. The laser spot size was estimated to be 40 µm as determined from laser burn marks on a thin film of a-cyanohydroxycinnamic acid.

For multiplex MSI, four spiral steps were defined for each raster step with TunePlus software (Thermo), and an MS scan event corresponding to each spiral step was set up with Xcalibur (Thermo). One orbitrap MS and three ion trap MS/MS scans were used in the current study (Fig. 1). The raster step size and spiral step size were 100 µm and 50 µm, respectively. Each spectrum was collected with five laser shots per scan and one scan per spiral step. The orbitrap scans were acquired over an *m/z* range of 200 to 1200. MS/MS scans were acquired with normalized collision energies of 50, 35 and 45 for verapamil, triacylglycerol (TAG) at *m/z* 785.66 and at 827.71, respectively, with 1.8 Da isolation width.

Data Analysis

Image Quest software (Thermo) was used to produce chemical images of LFP marks. A mass tolerance of 0.01 Da was used for generating orbitrap MS images, and 0.3 Da was used for MS/MS images. Orbitrap MS images were normalized against total

ion count, and for all the images, maximum scale is arbitrarily adjusted to produce best images. Qual Browser (Thermo) was used to generate averaged mass spectra. Internal calibration was made using a matrix ion at *m/z* 313.032.

Safety Considerations for Verapamil HCl

Verapamil is an L-type calcium channel blocker of phenylalkylamine class active pharmaceutical ingredient. Verapamil is purchased and used as verapamil HCl salt in fine powder form. Therefore, it should be handled in a chemical fume hood to avoid inhalation, and fingers should be washed thoroughly with soap water after contacting the verapamil HCl powder.[29]

Results and Discussion

Figure 1 illustrates how multiplex MSI works. In this experiment, we adapted a simple raster pattern with four spiral steps for each raster step. First, a set of ions produced from the first spiral step is introduced to the orbitrap high-resolution mass analyzer located after the linear ion trap. During the orbitrap imaging current measurement, the MALDI plate is moved to the next spiral step, and a set of ions from the second spiral step are introduced to the linear ion trap for MS/MS. Two more MS/MS scans are obtained from the third and fourth spiral steps to complete a raster step. The MALDI plate is then moved to the next raster step to start a new set of spiral steps. This pattern of four scan events is continuously followed over the entire imaging area with 50 mm spiral steps size and 100 mm raster steps. We have chosen *m/z*

455.29 [verapamil+H]$^+$, 785.66 [TAG(45:1)+Na]$^+$ and 827.71 [TAG (48:1)+Na]$^+$ for MS/MS.

Typical small molecule analysis is performed with chromatographic separations, such as GC- or LC-MS, for authentic identification of unknown compounds. However, traditional chromatographic separation cannot be used for MSI, making the identification of unknown compounds very difficult. Accordingly, alternative information is essential in MSI to assist identification of unknown compounds. For this purpose, accurate mass information obtained through high-resolution mass spectrometric measurement is very useful. Commonly adapted high-resolution mass analyzers for MALDI-MS measurements include (reflectron geometry) time-of-flight (TOF), Fourier transform ion cyclotron resonance (FTICR) and orbitrap. Among those, orbitrap presents a compromise between scan speed and resolving power; it is faster than FTICR but slower than TOF and has higher mass resolving power than TOF but lower than FTICR.

Figure 2 shows the orbitrap mass spectrum averaged over the entire LFP. Most of the major signals could be assigned molecular formulas based on accurate mass information. The chemical images of a few selected compounds are also shown in Fig. 2. Several lipid compounds known to be present in fingerprint residue could be successfully detected and imaged, including cholesterol (as a water loss at *m/z* 369.352; 0.17 ppm), oleic acid (*m/z* 283.263; 0.70 ppm) and various TAGs (e.g. [TAG(45:1)+Na]$^+$ at *m/z* 785.666 (3.9 ppm) and [TAG(48:1)+Na]$^+$ at *m/z* 827.713 (3.7 ppm)). The first inset mass spectrum of Fig. 2 shows a zoomed in view of the *m/z* 500–900 range. Most of the peaks from *m/z* 750 to 900 correspond to various sodiated TAG species, and the peaks from *m/z* 500 to 750 are mostly in-source fragments of TAGs to

diacylglycerols (DAGs).[36] LFP are rich in lipids such as TAGs due to the high density of eccrine sweat glands on the hands.[20] Because of their high abundance, clear fragmentation patterns and variety of structural isomers, we have chosen TAGs as the target for the subsequent MS/MSI (Fig. 3, see below).

We could also detect some exogenous compounds such as benzyl dimethyl dodecyl ammonium (BDDA) at *m/z* 304.300 (0.5 ppm), dimethyl dioctadecyl ammonium (DDA) at *m/z* 550.626 (1.7 ppm) and verapamil at *m/z* 455.291 (1.1 ppm). Both BDDA and DDA have previously been detected in LFP.[24] Verapamil was intentionally applied to the finger before deposition as an example of a potential exogenous chemical marker for suspect identification or discrimination. DDA is an ingredient in common household disinfectants while BDDA is used as an antistatic agent in products like fabric softener, cosmetics and conditioners. The latter two compounds were unintentionally left over on the fingerprints, suggesting sensitive detection of exogenous compounds is possible by MSI.

The second zoomed-in inset mass spectrum at *m/z* ~ 550.5 demonstrates the power of high-resolution mass spectrometers in distinguishing isobaric ions. Within a 0.5 Da mass window of *m/z* 550.629 (DDA), there are three other mass peaks *m/z* 550.424, *m/z* 550.492 (13C isotope of DAG(32:1)) and *m/z* 551.016 (DHB3Na4). Hence, it might not have been possible to distinguish the four peaks with a low-resolution mass spectrometer, but now they can be clearly distinguished and separately imaged in high-resolution orbitrap.

Figure 3 shows MS/MS spectra of *m/z* 455.29 $[\text{verapamil+H}]^+$, 785.66 $[\text{TAG(45:1)+Na}]^+$ and 827.71 $[\text{TAG(45:1)+Na}]^+$ acquired by multiplex MSI, along with the

ion images of a few selected products. MS/MS spectra verified their structures, and the images of each product confirmed they have the same spatial distribution. If there are two or more LFP overlapping each other with a few chemical compounds present as structural isomers, the product ion image might be used to distinguish which chemical has come from which LFP. The MS/MS spectrum of verapamil is consistent with the known characteristic fragment ions at *m/z* 150, 165, 260 and 303.[37, 38] The loss of free fatty acid (–RCOOH) is commonly observed in MS/MS of TAGs[39] (Fig. 3B and 3C). MS/MS spectra of *m/z* 785.66 (TAG(48:1)+Na) and 827.71 (TAG(45:1)+Na) show peaks corresponding to the loss of at least four different free fatty acids each, indicating these signals arise from mixtures of two or more isomeric TAG species. TAG(45:1) and TAG(48:1) have 19 and 32 known isomers, respectively, according to Lipid Maps (www.lipidmaps.org). The presence of a particular fatty acid constituent in a TAG can be determined by MS/MS, while MS3 performed in our multiplex imaging set up for selected DAG fragments would allow for further investigation of structural details.

One intriguing feature in Fig. 2 is that LFP images for TAGs are slightly different from other lipids and exogenous compounds. In addition to the expected fingerprint ridge pattern, TAG images show scattered clusters of higher intensity that do not match the pattern. A similar pattern is observed for their product ion images as shown in Fig. 3. This distribution exactly matches that of a DHB-sodium cluster, $[3DHB\text{-}3H+4Na]^+$, at *m/z* 551.016. Based on this, we suspect these anomalies in ion intensities may result from local accumulation of sodium from sweat on the finger. Namely, intensities of sodiated species are dramatically increased where sodium is present in high

concentration. Variations in MALDI lipid intensity due to salt concentration differences have been previously observed in a rat brain imaging experiment.[40]

Conclusion

We successfully demonstrated that high-resolution MS combined with tandem MS can provide useful information in chemical imaging of LFP. Specifically, the multiplex MSI allowed the acquisition of both accurate mass and tandem MS-based structural information in a single experiment. This technique would be very valuable when the available sample is very limited, as is often the case with LFP. We could detect and image the chemical distributions of both endogenous (fatty acids, cholesterol and TAGs) and exogenous compounds (BDDA, DDA and verapamil). In the current proof of concept experiment, we have chosen only three compounds for MS/MS, but one can adapt, for example, nine spiral steps to acquire MS/MS images of five additional compounds. One can also incorporate data-dependent scans to obtain hundreds of MS/MS spectra on various positions, which can be very helpful for forensic identifications. The ability of this method to distinguish isobaric ions with high-resolution MS and structural isomers with tandem MS, while facilitating identification of unknown compounds adds great potential for chemical marker identification in forensic and medical science.

Acknowledgements

This work was supported by the U.S. Department of Energy (DOE), Office of Basic Energy Sciences, Division of Chemical Sciences, Geosciences and Biosciences. The Ames Laboratory is operated by Iowa State University under DOE Contract DE-AC02-07CH11358.

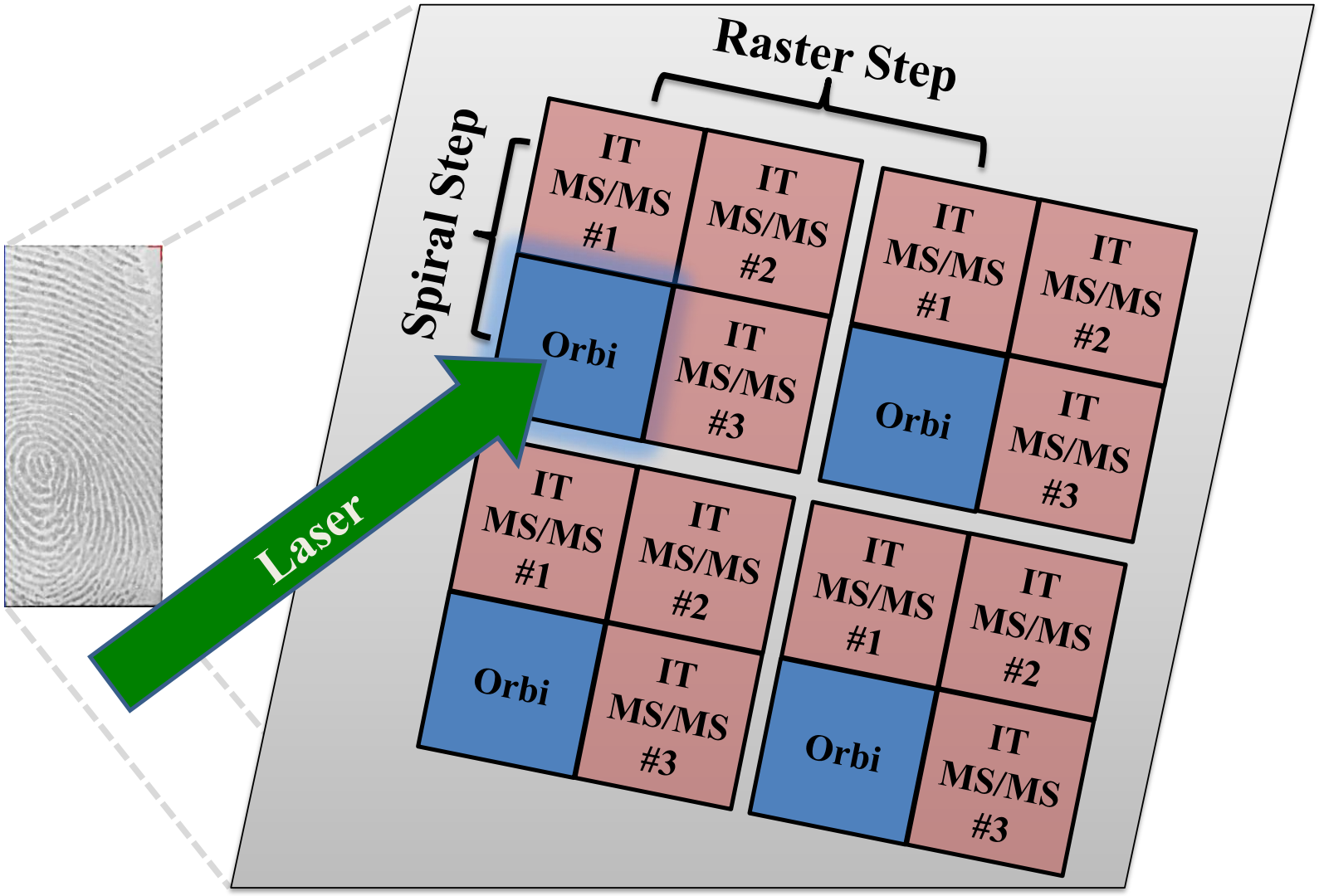

Figure 1: Illustration of spiral and raster step movement in multiplex MSI

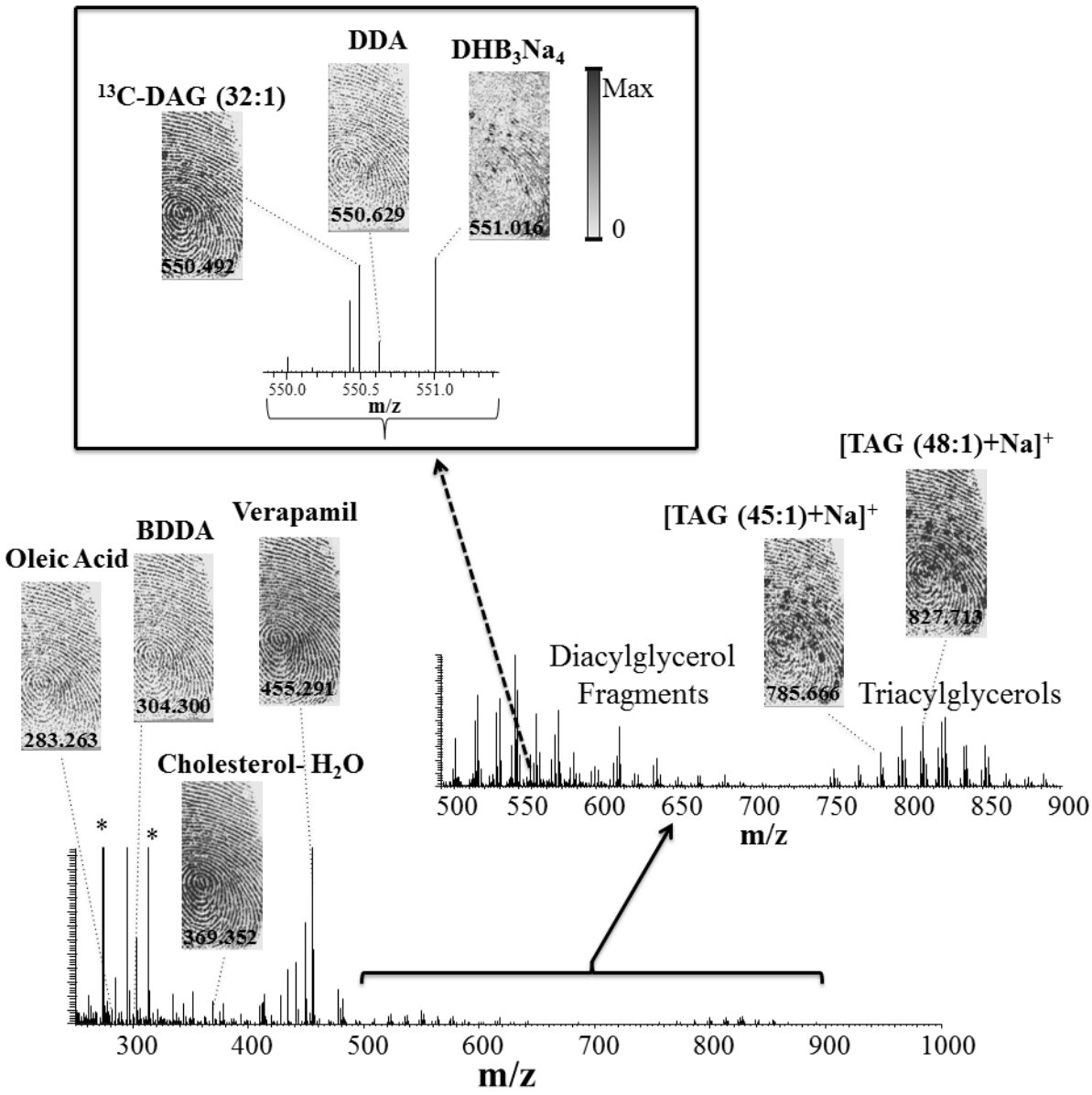

Figure 2: The orbitrap mass spectrum averaged over the entire LFP and MS images of a few selected compounds. All the assigned compounds are detected as the protonated form, $[M+H]^+$, except cholesterol as a protonated water loss, $[M-H_2O+H]^+$, and sodium adducts in case of TAGs and DHB cluster ions. MS images are normalized to the total ion count.

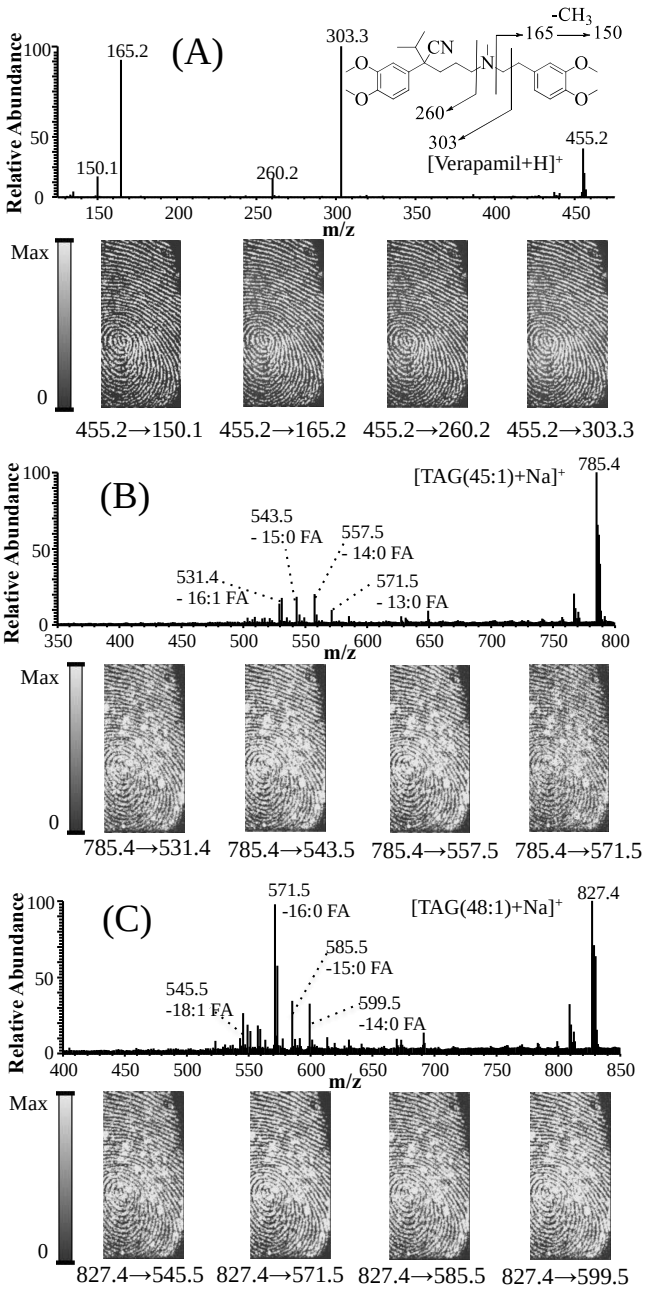

Figure 3: Ion trap MS/MS spectra of *m/z* 455.29 (A, verapamil), 785.66 (B, $[TAG(45:1)+Na]^+$ and 827.71 (C, $[TAG(45:1)+Na]^+$). MS/MS ion images of selected products are also shown.

CHAPTER 3

INVESTIGATION OF THE CHEMICAL INTERFACE IN THE SOYBEAN-APHID AND RICE-BACTERIA INTERACTIONS USING MALDI-MASS SPECTROMETRY IMAGING

A paper published in *Analytical Chemistry*

Anal. Chem., **2015**, 87 (10), pp 5294–5301
Reproduced by permission of American Chemical Society

Gargey B. Yagnik, Adam T. Klein, Jessica D. Hohenstein, Zhiyuan Ji, Jiachen Zi, Malinda D. Reichert, Gustavo C. MacIntosh, Bing Yang, Reuben J. Peters, Javier Vela, and Young Jin Lee

Abstract

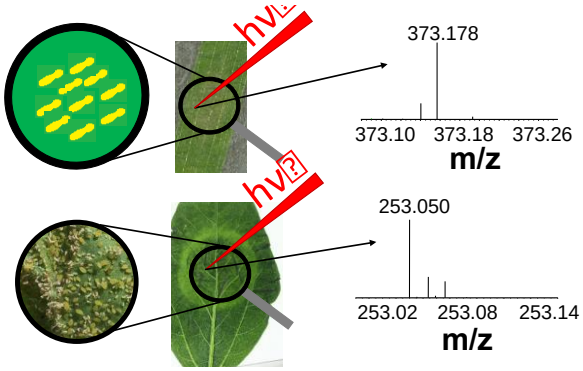

Mass spectrometry imaging (MSI) is an emerging technology for high-resolution plant biology. It has been utilized to study plant-pest interactions but is limited to the surface interfaces. Here we expand the technology to explore the chemical interactions occurring inside the plant tissues. Two sample preparation methods, imprinting and fracturing, were developed and applied, for the first time, to visualize internal metabolites of leaves in matrix-assisted laser desorption ionization (MALDI)-MSI. This is also the first time nanoparticle-based ionization was implemented to ionize diterpenoid phytochemicals that were difficult to analyze with traditional organic

matrices. The interactions between rice-bacterium and soybean-aphid were investigated as two model systems to demonstrate the capability of high-resolution MSI based on MALDI. Localized molecular information of various plant- or pest-derived chemicals provided valuable insight for the molecular processes occurring during the plant-pest interactions. Specifically, salicylic acid and isoflavone based resistance was visualized in the soybean-aphid system, and antibiotic diterpenoids in rice-bacterium interactions.

Introduction

In nature, plants encounter diverse pests including pathogens and insects; thus the plant-pest interface is a battlefield of continuous chemical attacks and defenses. Plants possess an innate immune system that detects conserved pathogen-derived molecules and trigger an array of defense responses. Conversely, these pests deploy effector molecules to suppress innate defenses and to manipulate the host metabolism for nutritional benefit.[41-44] Most current work on the chemical interactions between plants and pests involves *ex situ* extraction of metabolic or genetic materials with homogenization of various tissues and cell types.[45-48] This approach has many limitations. Firstly and most importantly, it fails to provide critical information on the spatial distribution of chemicals. Secondly, the homogenization process significantly dilutes analytical signals to levels that are sometimes indistinguishable from the background (false negative). Lastly, the lack of spatial information may cause chemical responses to non-target stimuli to be misattributed to plant-pest interactions (false positive).

Laser capture microdissection (LCM) has been applied for metabolic profiling of plant tissues.[49, 50] This method can circumvent the above limitations by precisely cutting out specific cells or tissues of interest. However, it has its own limitations including potential delocalization of small molecules during fixation and embedding. Most of all, in a typical LCM analysis, tens or hundreds of cells need to be collected, resulting in extended sample preparation time and the loss of asymmetric metabolic distributions among the same cell types. Liquid extraction surface analysis mass spectrometry (LESA-MS) is another method recently developed to overcome the lack of spatial information in traditional metabolic profiling.[51] In this approach, a robotic arm automatically extracts soluble materials from each localized area using a micropipette and introduces the sample directly into the mass spectrometer. This method minimizes sample preparation and allows imaging experiments[52]; however, its spatial resolution is limited to only about one millimeter size.

In situ imaging can provide fine details with high-spatial resolution. However, molecular imaging in plants is mostly limited to fluorescence,[53] which provides subcellular distributions but only those of macromolecules labeled as targets. Accumulation of small molecules is one of the most direct evidences of plant-pest interactions but the technology for their *in situ* chemical imaging is nearly nonexistent. Mass spectrometry imaging (MSI) is an excellent tool of choice for imaging small molecules.[54] It provides extremely high sensitivity, down to attomole (10^{-18} mole) levels[55], a high-degree of *in situ* chemical mixture separation (up to thousands of molecules in *m/z* space), and the ability to characterize novel molecules; thus, it is

extremely well-suited for metabolite imaging. MSI has recently been used extensively for imaging plant metabolites [56-58], including our own work.[59-61]

Most MSI applications for plant materials are made through direct interrogation on plant surfaces or thin sections obtained by cryosectioning.[44, 57] Unfortunately, neither method is applicable for visualization of the internal metabolite distributions of thin leaves or flower petals along the lateral dimension. Imprinting internal plant molecules onto Teflon or silicate surfaces has been proven to be an efficient sample preparation method for this purpose[62] and is extensively utilized for desorption electrospray ionization (DESI).[57] However, DESI is limited to polar compounds analysis and its spatial resolution is typically ~200 μm[63], although <50 μm resolution has been reported[64, 65]. NanoDESI enables up to 10 μm spatial resolution,[66] but is not commercially available. MSI using matrix-assisted laser desorption ionization (MALDI) is a versatile alternative as it allows much higher spatial resolution and analysis of wide classes of compounds. Combining cell-transfer by contact printing and carbon-substrate-based laser desorption ionization, Li et al. profiled and imaged trichome specialized metabolites of *Solanum habrochaites*.[67] Plant metabolites associated with pest defense have been investigated using MALDI-MSI[68, 69], however, no study has been made for MSI to interrogate internal metabolites induced by plant-pest interactions. Hamm et al. utilized MSI to image the chemical responses of *Cabernet Sauvignon* after infection by *Plasmorpara viticola*.[70] This work analyzed only limited target molecules, resveratrol and pterostilbene, on the surface of the leaf by direct laser desorption ionization.

Two biological systems are used to study the chemical interfaces in plant-pest interactions in the current work: soybean-soybean aphids (*Glycine max* colonized with *Aphis glycines*) and rice-bacterium (*Oryza sativa* infected with *Xanthomonas oryzae* pv. *oryzae* (Xoo)). Soybean aphids are native to Asia and are a recently introduced pest affecting soybean plants in North America. Soybean aphid infestation results in changes in the metabolome of soybean plants. Some of these changes include the accumulation of phytohormones such as salicylic acid, ethylene, and jasmonic acid that can mediate defense responses,[48, 71] changes in amino acids that may modify the nutritional capacity of the plant,[72] and changes in chlorophyll content.[73] However, our knowledge of the soybean metabolite changes in response to aphid colonization is limited, and their spatial distribution is unknown. Understanding how the metabolites are changing during plant-pest interactions can be crucial to understanding a plant's resistance or susceptibility to attack.

Xoo is the causal agent of bacterial blight of rice.[74] Many plants, including rice, produce secondary metabolites with antimicrobial activity as a part of their defense mechanism.[9] Phytochemicals produced as a defense against pathogen infection by rice plants include three types of diterpenoid phytoalexins; phytocassanes, oryzalexins and momilactones.[75] Chemical analysis of these phytochemicals has been mostly performed with *ex situ* extraction followed by MS or NMR analysis and there has been no direct *in situ* analysis nor imaging, although oryzalexins have been localized to infected (versus uninfected) leaves.[76] The diterpenoids produced by the rice plant as a part of defense mechanism are very difficult to analyze in MALDI-MS because

traditional organic matrices cannot efficiently ionize these unusual phytochemicals, presumably due to the lack of ionizable functional groups.

Here we demonstrate the utility of MALDI-MSI as a tool to investigate plant-pest interactions that are not limited to the surface but include the interior of the plant tissues where metabolism is significantly altered by the interactions. Specifically, the plant responses to two distinct pest classes, insect (aphid) and bacterium (Xoo), were investigated. To expose internal molecules for interrogation by the laser beam, we developed and applied 'imprinting' and 'fracturing' methods. The imprinting technique is used to squeeze out internal metabolites with minimal delocalization during the process. Fracturing is a simple method often used in optical microscopy to expose and visualize internal plant tissues, but here we applied this technique, for the first time, for MS imaging. Additionally, we successfully applied nanoparticle-assisted laser desorption ionization (NALDI), [77, 78] for characterization of diterpenoids. The soybean-soybean aphids (*Glycine max* colonized with *Aphis glycines*) study was performed by Adam T. Klein. The experimental details, results and discussion for soybean-soybean aphids system are submitted in Adam T. Klein's dissertation.

Experimental

Materials

Iron (II) chloride tetrahydrate (99.0%) and iron (III) chloride hexahydrate (> 97.0%) were purchased from Strem Chemicals Inc. (Newburyport, MA, USA). Ethanol (200 proof), nitric acid (Certified ACS Plus- 69.4%), and ammonium hydroxide (Certified ACS Plus) were purchased from Fisher Scientific (Waltham, MA, USA). Isopropyl

alcohol (LCMS Chromasolv) were purchased from Sigma Aldrich (St. Louis, MO, USA). Titanium (IV) n-butoxide (99.0%) was purchased for Acros Organics (Pittsburgh, PA, USA).

Bacterial Inoculation in Rice Plant

The bacterial strain used in this study was *Xanthomonas oryzae* pv. *oryzae* strain PXO86 and rice plants were IR24 and IRBB10 (*Oryza sativa*). IR24 is susceptible to PXO86 carrying *avrXa10*,[79] while IRBB10, which is a near-isogenic line containing *Xa10* gene in the IR24 genetic background,[80] is resistant to PXO86. All plants were grown in a growth chamber at a constant temperature of 28 ℃, relative humidity of 75%, and photoperiod of 12h. For bacterial inoculation, PXO86 was grown in nutrient broth (Difco Laboratories) at 28 ℃. The cells were harvested by centrifugation (4,000 rpm), washed twice, and re-suspended in sterile water to an optical density of 0.5 at 600 nm. Suspensions were infiltrated into rice leaves (3 weeks old) with a needleless syringe and the inoculated leaves were harvested 72 hours post inoculation for MSI.

Fe_3O_4 Nanoparticles Synthesis

For the synthesis of Fe_3O_4 NPs, 1 mL of 2 M $FeCl_2 \cdot 4H_2O$ and 4 mL of 1 M $FeCl_3 \cdot 6H_2O$ were mixed together. Under continuous stirring, 50 mL of 0.5 M NH_4OH was added drop wise and stirring continued for 30 min. The resulting solution was then centrifuged at 4500 rpm for 10 min and washed with deionized water. The washing and centrifugation steps were repeated until the supernatant was neutral. After washing

with water, the precipitate was washed once with methanol and allowed to dry overnight.[81]

TiO_2 Nanoparticles Synthesis

Titanium dioxide nanoparticles were synthesized as described by Shrivas *et al*.[78] Titanium (IV) n-butoxide (17 mL) and ethanol (8 mL) were mixed in a 50 mL round bottom flask by stirring for 10 min at room temperature, then cooled in an ice water bath. Concentrated nitric acid (375 µL) was mixed with 8 mL of ethanol and added drop wise to the titanium butoxide mixture under vigorous stirring while cooled in an ice water bath. Stirring was continued for 30 minutes after the addition was completed.

Nanoparticles Application with Oscillating Capillary Nebulizer

The synthesized Fe_3O_4 and TiO_2 NPs were suspended in isopropyl alcohol at 5 mM and 10 mM concentrations respectively, and 500 µL of suspension was sprayed on the fractured sample using a home-made oscillating capillary nebulizer (OCN).[59] The procedure for suspension solution application was as follows: (1) fill up the 500 µL syringe with suspension, (2) place a blank target plate 8-10 cm below the tip of the OCN, (3) start the nebulizing gas (N_2) flow and adjust the pressure to ~40 psi, (4) set the flow rate of the syringe pump at 50 µL/min and start the flow, (5) monitor the blank target plate surface to ensure matrix is being applied and wetting is minimal, (6) stop the syringe pump and place the PTFE membrane below the tip of the OCN, and (7) turn on the syringe pump and spray 500 µL of suspension that covers a ~2 cm sample uniformly.

MSI Data Acquisition and Data Processing

A linear ion trap-Orbitrap mass spectrometer with MALDI ion source (MALDI LTQ-Orbitrap Discovery; Thermo Scientific, San Jose, CA, USA) was used for the current study. The instrument was modified to use an external frequency tripled, diode pumped Nd:YAG laser operating at 355 nm (UVFQ; Elforlight Ltd., Daventry, UK). Laser energy of about 5-7µJ/pulse were used for MSI of rice leaf, at 60 Hz repetition rate. The laser spot size was estimated to be 30~40 µm as determined from laser burn marks on a thin film of α-cyanohydroxycinnamic acid. A raster step size of 100 was used for MSI of rice leaf, unless otherwise noted. Each spectrum was collected with 10 laser shots per scan and one scan per raster step. Orbitrap scans were acquired over the *m/z* range of 100 to 1200.

ImageQuest software (Thermo Scientific) was used to produce chemical images from MS imaging data sets. A mass tolerance of ±0.003 Da was used for generating Orbitrap MS images. All the MS images were normalized against total ion count at each pixel and the maximum scale was arbitrarily adjusted to produce the best quality images as indicated in the figure caption. All the image features shown in this manuscript were reproduced in at least two or three replicate experiments.

Results and Discussion

Fracturing Plant Leaf to Expose Internal Tissue.

For the study of the chemical interactions between rice and bacteria, we initially tried the 'imprinting method' introduced above, but we could not detect any diterpenes or other hydrophobic compounds that are of particular interest in this system.[75] This is

consistent with the results for the soybean-aphid study (see Adam T. Klein dissertation), in that only cytoplasmic hydrophilic compounds can be analyzed with the imprinting method. Thus, we have developed and applied a new 'fracturing method' for visualization of a wider range of compounds in rice-bacterial interactions.

The overall procedure for the fracturing method applied in the current study is summarized in Figure 1. A section of the harvested leaf was stuck to a piece of transparent packing tape (Figure 1A). The tape with the leaf section was placed under vacuum (~150 mtorr) for 4 - 5 hours depending on leaf size (Figure 1B). After vacuum drying, the tape with the leaf was folded over to enclose the leaf or section of leaf between the two adhesive sides of the tape (Figure 1C). The tape and leaf sandwich was then passed through a rolling mill (Figure 1D) to fracture the leaf section. The rolling mill pressure knob was kept finger tight and care was taken so that the ends of the tape did not pass through the rolling mill. Finally, the two ends of the packing tape were pulled open, leaving one surface on each side of the folded tape (Figure 1E). The leaf section on packing tape was adhered to a MALDI target plate with double-sided tape, and subjected to matrix application and MSI data acquisition.

The intact and fractured leaf surfaces were visually inspected under the macrozoom mode of an optical microscope (Zeiss Axio Zoom V16) (Figure 2) and scanning electron microscope (SEM; JEOL JSM 5800LV) (Figure 3). Macrozoom images of the leaf surface show distinguishing features before and after the fracturing. Particularly, the veins are clearly observed as white lines after fracturing in Figure 2C. In the high-resolution SEM image, the presence of protuberances (Figure 3A and 3B) is observed on the intact leaf surface, but are absent in the fractured leaf surface (Figure

3C and 3D). In contrast, SEM images on the fractured leaf show hollow tubes corresponding to vascular bundles, suggesting the tissues along the veins are most fragile and subject to fracture when dried. Most importantly, the fractured tissues seem to maintain their original anatomy relatively well, at least to a resolution of ~10 μm, which is sufficient for typical MALDI-MSI.

Rice-Xoo Interaction

Three week-old leaves of resistant and susceptible rice plants were infiltrated with Xoo and incubated for 72 hours, then subjected to NALDI-MSI after fracturing (Figure 1). Figure 4 shows metabolite images of these resistant and susceptible rice leaves acquired using NALDI-MSI with Fe_3O_4 NPs. The compound assignments were based on accurate mass searched against the Metlin database, available literature, and also MS/MS spectra when available (Figures 6 and 7). The ion with *m/z* 614.238 is tentatively assigned as a chlorophyll-*a* fragment, derived from in-source fragmentation of the phytyl group ($C_{20}H_{39}$ side chain),[82] and MS/MS analysis of extracted chlorophyll-*a* supports this assignment (Figure 6). We initially tried various organic matrices and nanoparticles, but only Fe_3O_4 and TiO_2 NPs were able to efficiently ionize the diterpene compounds from Xoo infected rice leaf tissues. TiO_2 NPs gave similar images to Fe_3O_4 NPs (Figure 5). It will be further investigated in the future as to why TiO_2 and Fe_3O_4 NPs are the only matrices that can ionize diterpenoids; however, a possible explanation is that they can be heated up to a very high temperature before exploding to form a laser plume because of their high heat capacity. Most of the diterpenes have high melting and/or boiling points compared to other small metabolites (e.g. the m.p. is 242

°C for momilactone B and 160-180 and 117-120 °C for sucrose and chlorophyll-*a*, respectively) and may not be easily evaporated by other matrices. As supporting evidence for this hypothesis, we noticed much higher laser energy is required for these NPs compared to organic matrices and increased molecular fragmentation was often observed in control analyses of authentic standards. Similar trends were observed in our systematic study of applying various nanoparticles to a wide range of plant metabolites.

The left four chemical images in Figure 4 represent common plant metabolites such as a phosphocholine, disaccharide (e.g. sucrose), chlorophyll-*a* and monogalactosyldiacylglycerol (MGDG). Phosphocholine ion signals have some contribution from fragmentation of phosphatidylcholine, but we cannot distinguish the fragments from naturally occurring phosphocholine. Phosphatidylcholines are completely fragmented in NALDI with TiO_2 or Fe_3O_4 NPs according to the standard analysis (data not shown) presumably due to the high temperature in NALDI conditions. In susceptible plant leaves, decreased levels of phosphocholine and disaccharide were observed, especially at the site of infection, in comparison to resistant plants, whereas the changes in ion abundances for chlorophyll-*a* fragment and MGDG are relatively minimal or ignorable. Similar results were observed for the second most abundant membrane lipid in plants, digalactosyldiacylglycerol (DGDG). Semi-quantitative comparison was made as shown in Figure 8, which depicts a significantly higher abundance of sucrose and phosphocholine in resistance rice, with no or minimal differences in other major lipids or metabolites.

The most notable observation in NALDI-MSI of Xoo-infected rice is the high abundance of phytoalexins, momilactones and phytocassanes, at the site of infection on resistant plant leaf samples (Figures 4 and 5). In contrast, the momilactones and phytocassanes are mostly absent in the susceptible rice. This is consistent in the semi-quantitative comparison presented in Figure 8. Identification of these phytoalexins are mostly based on accurate mass information, but also supported by MS/MS analysis, although phytocassanes A, D, and E are structural isomers and could not be distinguished (Figure 7). The production of these antimicrobial compounds in Xoo infected resistant rice plants has been reported by GC-MS analysis of leaf extracts, but not otherwise localized.[75] Further study is needed to better understand this rice-bacterial pathogen interaction, but this finding suggests a dynamic and complex nature for the production of diterpenoid phytoalexins by rice.

CONCLUSIONS

In this work, we have demonstrated that MSI can be a very useful tool to study the chemical interfaces in plant-pest interactions. Sample preparation is a critical bottleneck because it is almost impossible to cross-section thin leaves in the planar dimension. For the visualization of metabolites across the leaf, the imprinting and fracturing methods have been developed to expose internal metabolites of plant leaves. The two sample preparation methods are complementary to each other. Imprinting is efficient for the analysis of cytoplasmic hydrophilic compounds that can be squeezed out. The greatest advantage of this method is its versatility. It can be applicable to almost any plant leaves, regardless of their size or surface roughness. This method,

however, has a critical limitation that membrane-bound molecules, membrane lipids, or other hydrophobic compounds cannot be analyzed. Another limitation is the possible loss of spatial resolution during the imprinting process; however, this seems to be relatively minimal for most tissues. The fracturing method is effective for compounds that are present on the fracture-opened surface including phospholipids and chlorophylls that cannot be analyzed with the imprinting technique. One limitation is that we cannot control which layer will fracture-open. In the case of rice leaf, the mesophyll layers surrounding the veins seem to be most fragile and vulnerable to fracturing. Another limitation is that it is difficult to apply to a large size leaf, such as soybean leaf, because it tends to partially crack before it is completely dried. In-parallel control experiment with an uninfected leaf would be important in such experiments due to the possible metabolic turnover during sample processing.

Efficient ionization is often a critical obstacle in MSI depending on what types of analytes are the target molecules of interest. As is well known, the classes of compounds that can be ionized by MALDI are greatly affected by the matrix of choice. We have successfully developed and demonstrated the use of Fe_3O_4 and TiO_2 nanoparticles to efficiently ionize diterpenoid phytoalexin compounds that cannot otherwise be analyzed. We are currently screening various nanoparticles for a wide range of plant metabolites, to further understand ionization mechanisms and apply this to analyses of diverse classes of plant metabolites.

The demonstrated approach of using MSI to study the chemical interfaces of plant-pest interactions has many advantages compared to traditional metabolic profiling, especially in providing precise localization information with high sensitivity. The current

work demonstrates the power of this technology and we envision that application of this approach will open new opportunities in plant pathology.

Acknowledgements

This work was supported by the U.S. Department of Energy (DOE), Office of Basic Energy Sciences, Division of Chemical Sciences, Geosciences, and Biosciences through Ames Laboratory for MSI of rice-bacteria research and NALDI development (YJL and GBY) and by the Iowa State University Plant Sciences Institute for MSI of soybean-aphid research (YJL and ATK). This work was also supported by grants from the Plant Sciences Institute and the Iowa Soybean Association to GCM, a grant from USDA-NIFA (grant 2014-67013-21720) to RJP and BY, and a grant from the ISU Bioeconomy Institute and Iowa NSF EPSCoR to JV. We acknowledge Dr. Horner and Ms. Pepper at Microscopy and NanoImaging Facility for their assistance and valuable discussion in sample preparation and microscopic and SEM image acquisition. The Ames Laboratory is operated by Iowa State University under DOE Contract DE-AC02-07CH11358.

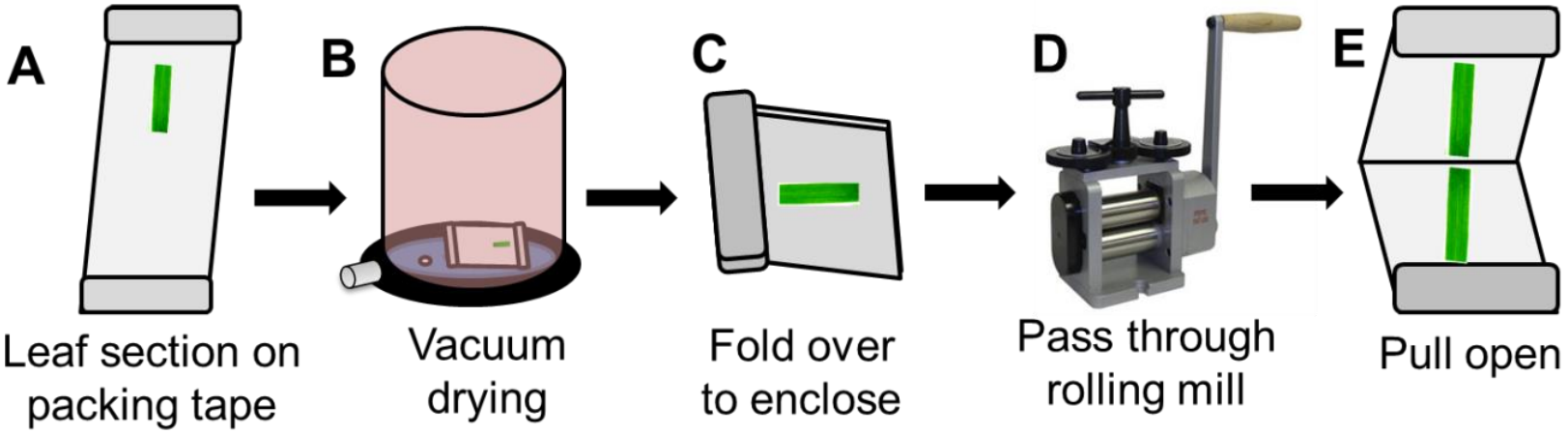

Figure 1: Step by step procedure for fracturing method.

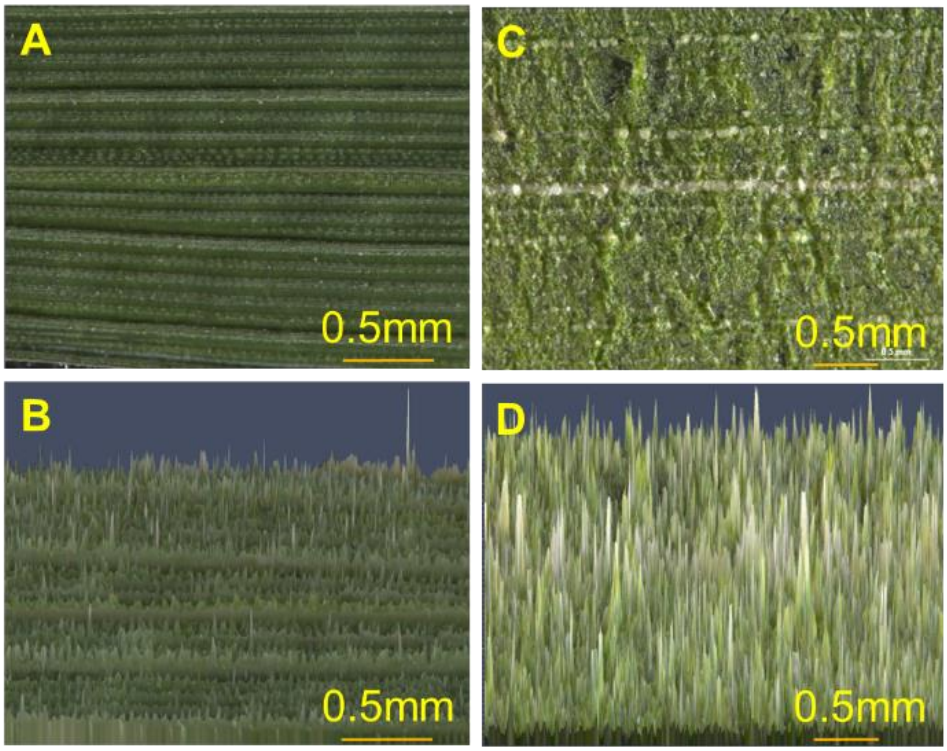

Figure 2: Macrozoom images of intact rice leaf surface (A, B) and fractured rice leaf surface (C, D). (B) and (D) are 3D constructed images.

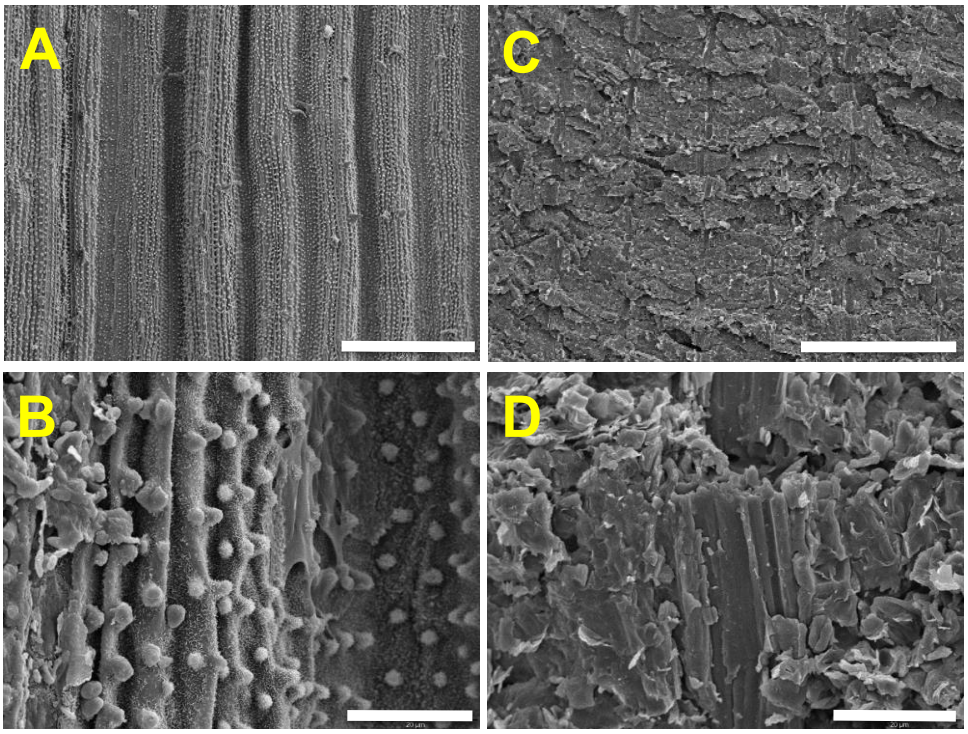

Figure 3: The SEM images of intact rice leaf surface (A, B) and fractured rice leaf (C, D). The scale bar corresponds to 200 µm for A and C and 20 µm for B and D.

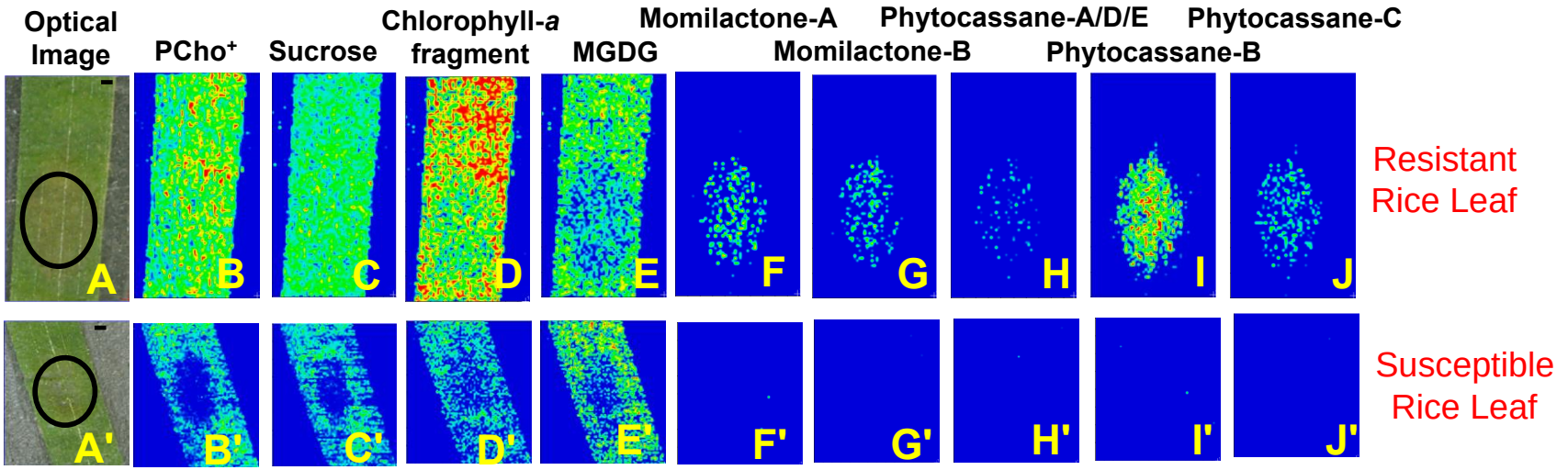

Figure 4: NALDI-MSI of fractured leaf section of three-week old resistant and susceptible rice infected by Xoo analyzed with Fe_3O_4 NPs. (A) Optical image of the rice leaf with the black circle representing the inoculated region. MSI images are shown for (B) phosphocholine (Pcho, *m/z* 184.074, 3.9 ppm; $5.0x10^{-2}$), (C) disaccharide, most likely sucrose, (*m/z* 381.079, 0.6 ppm; $2.5x10^{-1}$), (D) chlorophyll-*a* fragment (*m/z* 614.238, 1.5 ppm; $5.0x10^{-2}$), (E) MGDG (*m/z* 813.492, 1.2 ppm; $5.0x10^{-2}$), (F) momilactone-A (*m/z* 353.152; 1.6 ppm; $1.0x10^{-2}$), (G) momilactone-B (*m/z* 369.147; 1.1 ppm, $1.0x10^{-2}$), (H) phytocassane-A, D or E (*m/z* 355.167; 1.0 ppm, $1.0x10^{-2}$), (I) phytocassane-B (*m/z* 373.178; 1.1 ppm, $1.0x10^{-2}$), and (J) phytocassane-C (*m/z* 357.183; 1.3 ppm, $1.0x10^{-2}$). Phosphocholine was detected as a molecular cation (M^+) and the chlorophyll-*a* fragment was detected as the protonated ion ($[M- C_{20}H_{39} + H]^{+\cdot}$). All other compounds were detected as potassiated ions ($[M+K]^+$). A' to K' correspond to those in a susceptible rice leaf as a control. The scale bar corresponds to 0.5 mm.

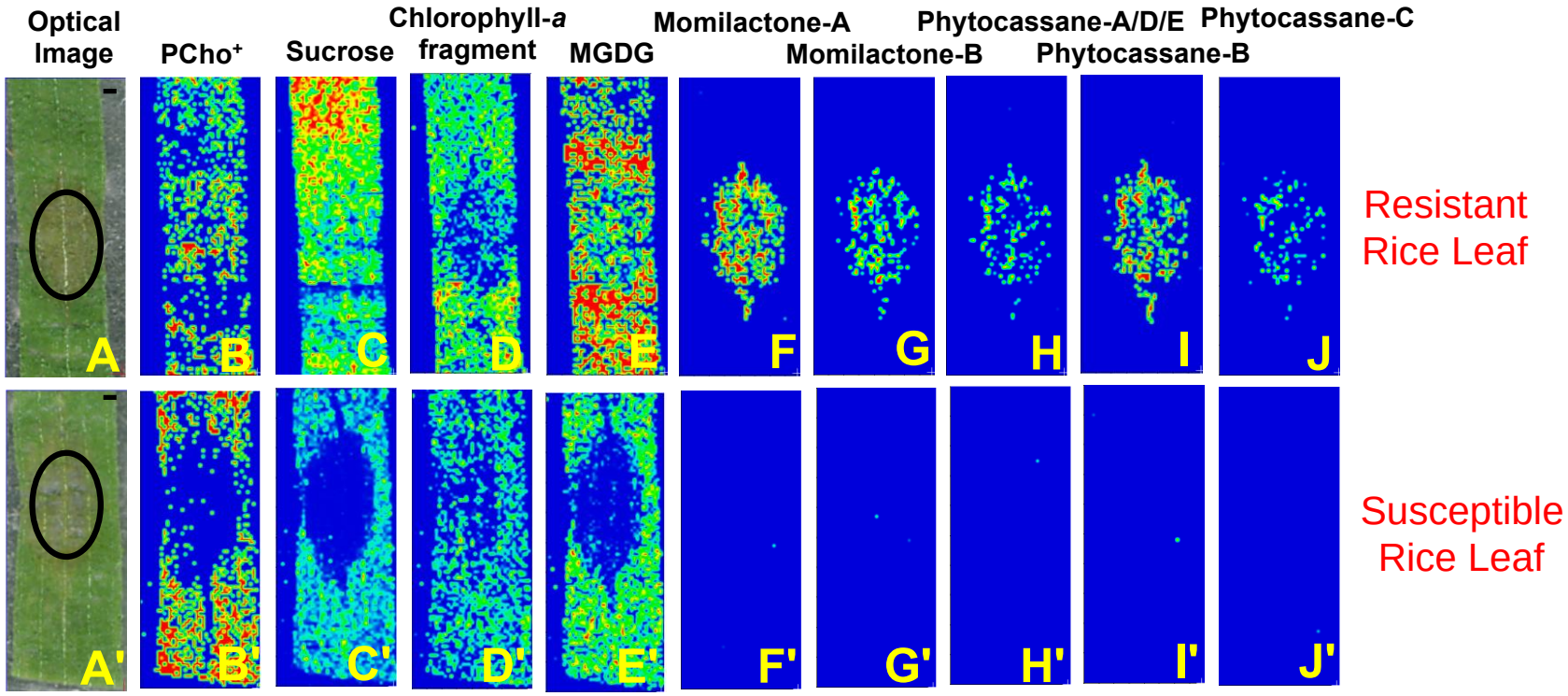

Figure 5: NALDI-MSI of fractured leaf section of three-week old resistant and susceptible rice infected by Xoo analyzed with TiO_2 NPs. (A) Optical image of the rice leaf with the black circle representing the inoculated region. MSI images are shown for (B) phosphocholine (*m/z* 184.074, 2.6 ppm; $1.0x10^{-3}$), (C) sucrose (*m/z* 381.079, 1.3 ppm; $2.0x10^{-1}$), (D) Chlorophyll-*a* fragment (*m/z* 614.238, 1.3 ppm; $1.0x10^{-2}$), (E) MGDG (*m/z* 813.494, 3.3 ppm; $2.5.0x10^{-2}$), (F) momilactone-A (*m/z* 353.152; 1.3 ppm; $2.5x10^{-3}$), (G) momilactone-B (*m/z* 369.147; 1.1 ppm, $2.5x10^{-3}$), (H) phytocassane-A, D or E (*m/z* 355.167; 1.4 ppm, $2.5x10^{-3}$), (I) phytocassane-B (*m/z* 373.178; 0.57 ppm, $2.5x10^{-3}$), and (J) phytocassane-C (*m/z* 357.183; 1.6 ppm, $2.5x10^{-3}$). Phosphocholine was detected as a molecular cation (M^+) and the chlorophyll-*a* fragment was detected as the protonated ion ($[M- C_{20}H_{39} + H]^{+\cdot}$). All other compounds were detected as potassiated ions ($[M+K]^+$). A' to K' correspond to those in a susceptible rice leaf as a control. The scale bar corresponds to 0.5 mm.

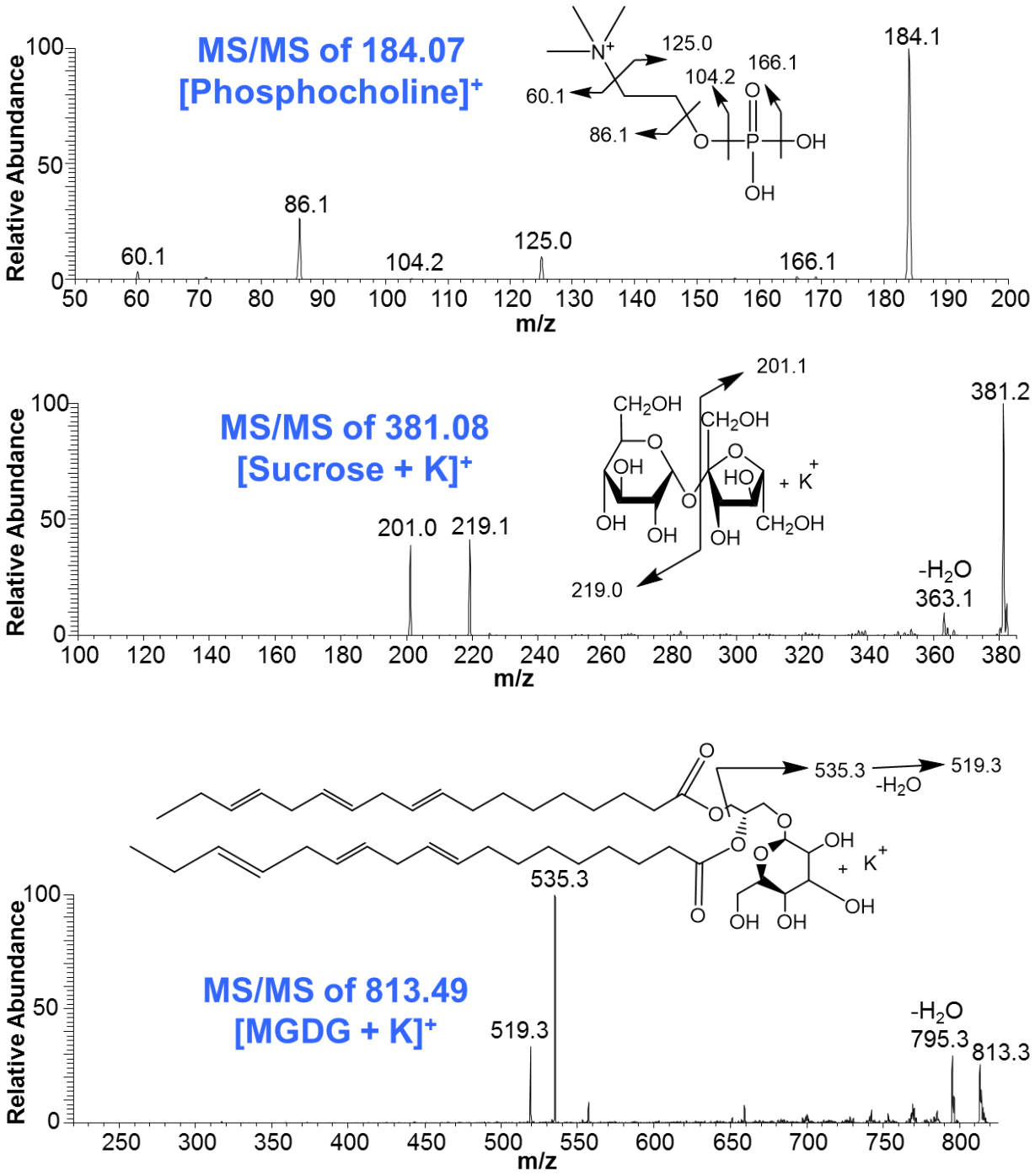

Figure continued

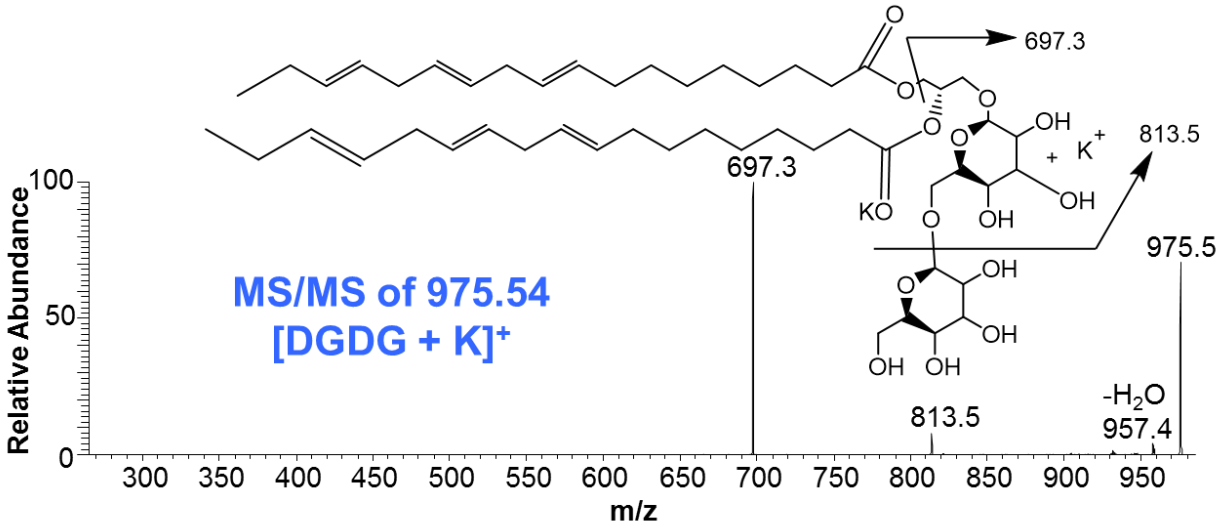

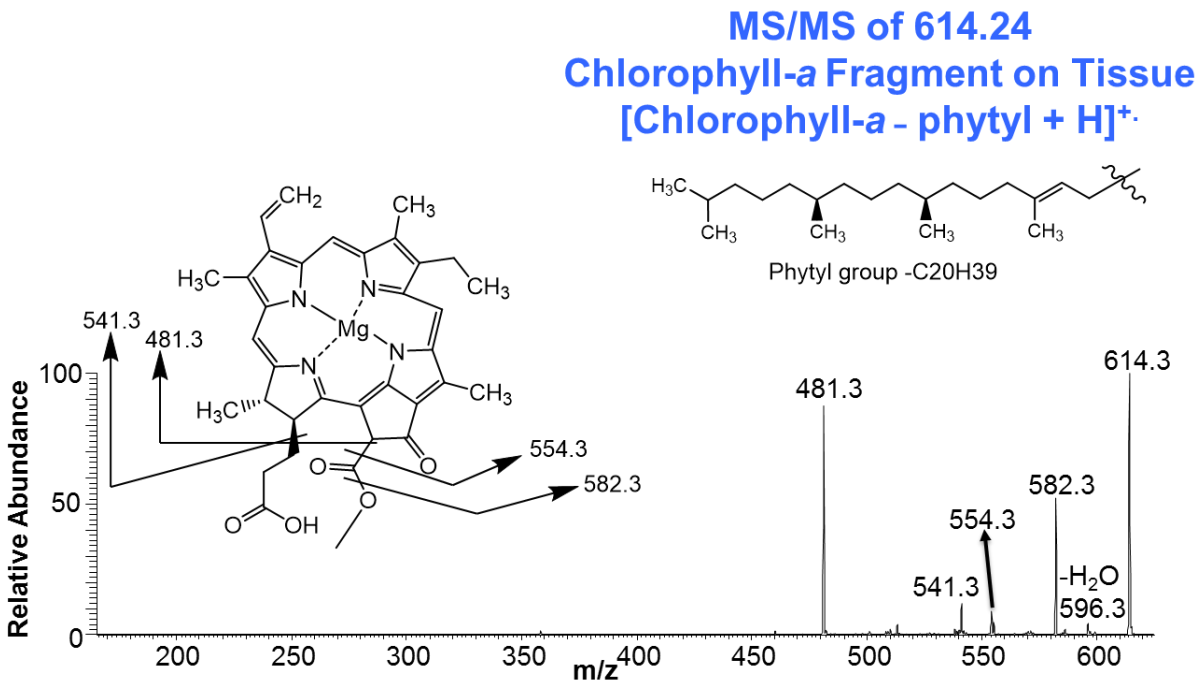

Figure 6: MALDI-ion trap MS/MS spectra of common plant metabolites phosphocholine, sucrose, MGDG, DGDG, and chlorophyll-*a* fragment[82] obtained directly on the fractured '*Xoo*' infected rice leaf surfaces. MS/MS spectra are matching with the standards (phosphocholine, sucrose), chlorophyll extract (chlorophyll-a fragment), or expectation (MGDG, DGDG).

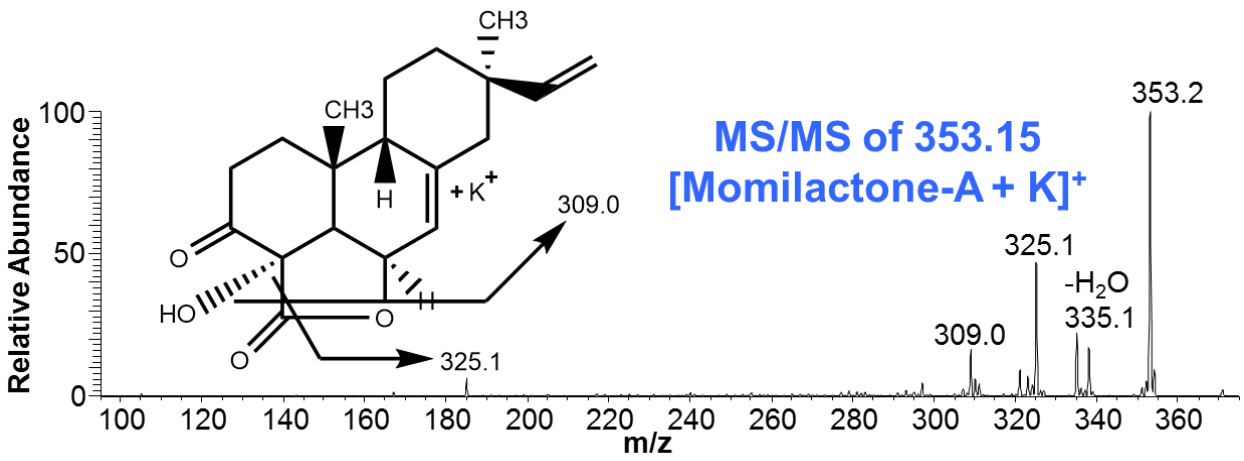

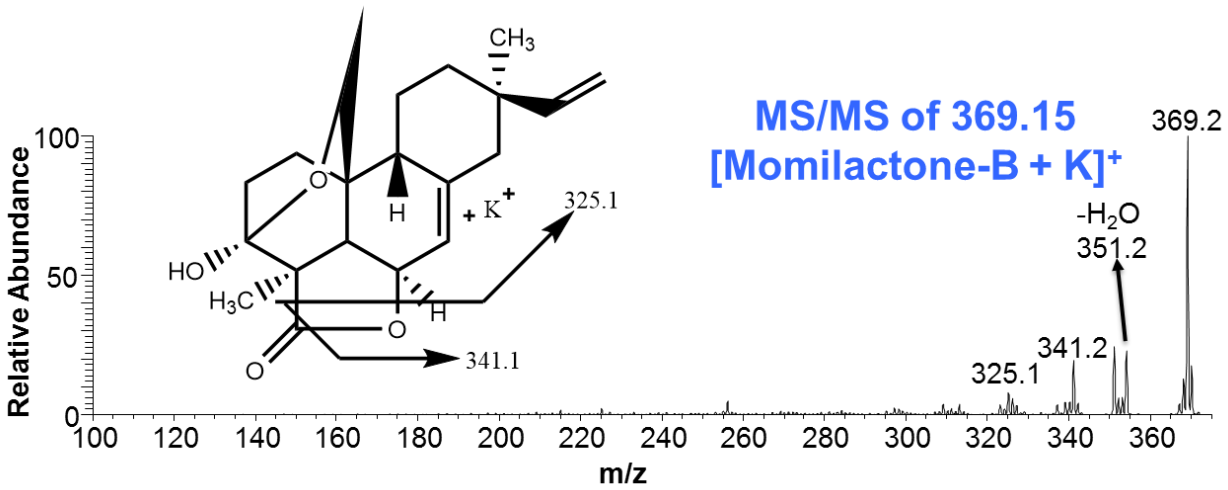

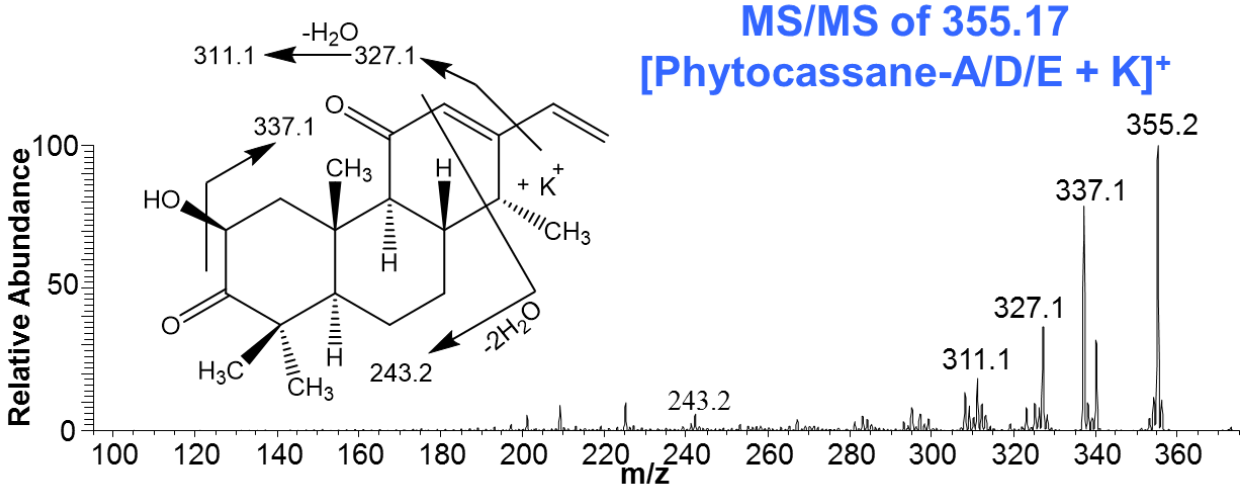

Figure continued

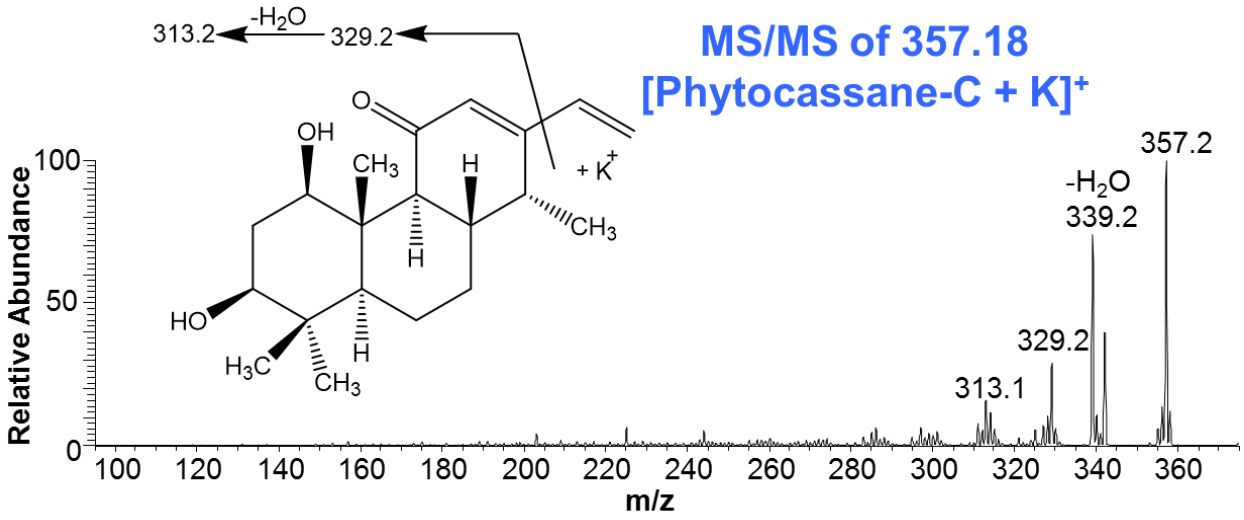

Figure 7: MALDI-ion trap MS/MS spectra of momilactone-A and B, and phytocassane-A/D/E, B, and C obtained directly on the fractured rice leaf surfaces after infection with '*Xoo*'. The MS/MS spectra are matching with the standard analysis of isolated diterpenes from the rice leaves.

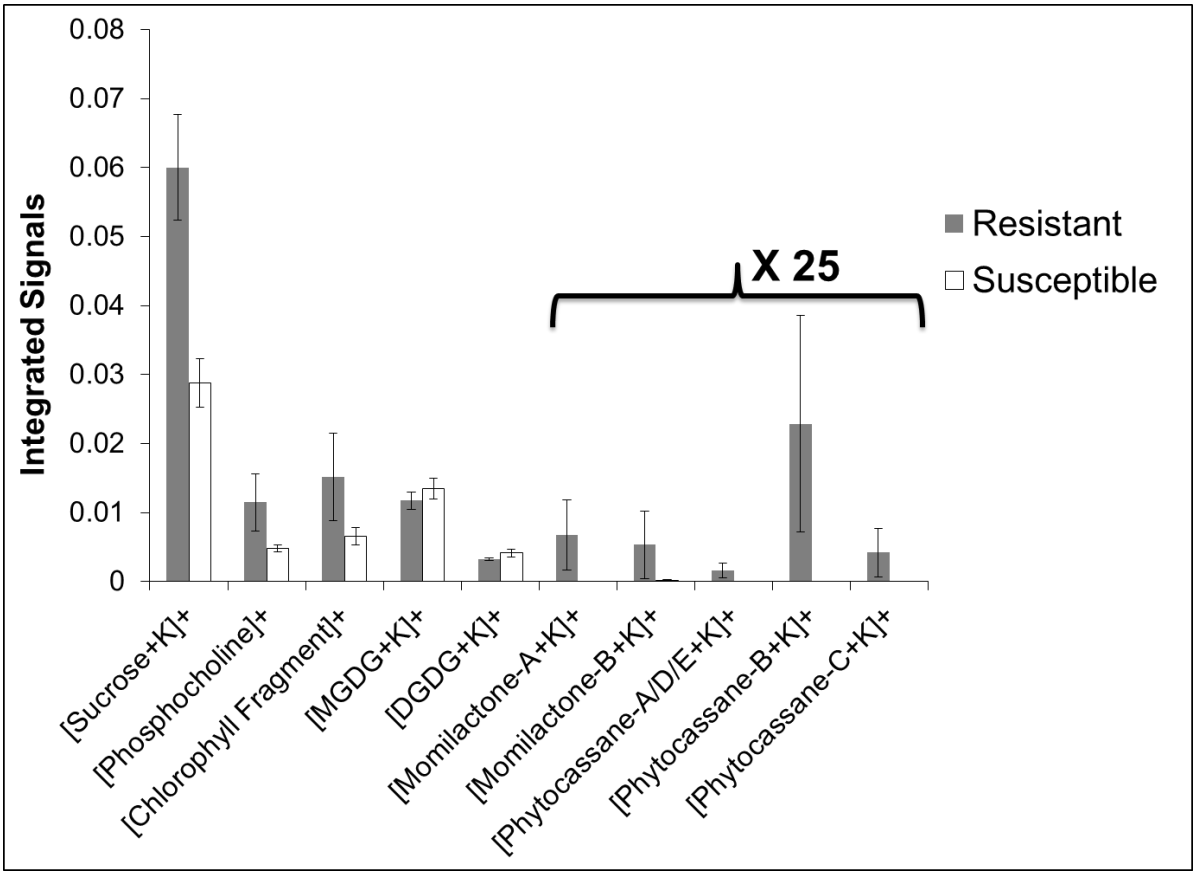

Figure 8: Semi-quantitative comparison of metabolite ion signals shown in Figure 4. Ion signals are integrated over the boxed region around the infected area with approximately 1:1 ratio between in- and outside the circle. Y-scale represents integrated ion signals normalized to the total ion count. Error bar represents standard deviation from three biological replicates. Diterpenoids are not detected in susceptible rice.

CHAPTER 4

NANOPARTICLE SCREENING FOR MASS SPECTROMETRY OF PLANT METABOLITES AND UNDERSTANDING OF THE NANOPARTICLE ASSISTED LASER DESORPTION IONIZATION MECHANISM

A paper in preparation

Gargey B. Yagnik, Andrew R. Korte, Malinda D. Reichert, Javier Vela, and Young Jin Lee

ABSTRACT

Nanoparticles have been applied in various fields of science due to their unique properties. These applications include many spectroscopic branches of analytical chemistry for a wide variety of analytical measurements. In the present study, thirteen nanoparticles have been compared with three popular organic matrices for nanoparticle/matrix-assisted laser desorption/ionization-mass spectrometry for the detection of low-molecular weight compounds. The chosen nanoparticles are potential matrices for detection of low-molecular weight compounds because of their absorptivity at the laser wavelength, low volatility, matrix homogeneity, and low background signal. We tested three deferent classes of nanoparticles including metals, metal oxides and carbon-based nanoparticles to desorb/ionize a variety of plant metabolites. This empirical study will be helpful for future selection of particular nanoparticle matrices for ionization of wide and/or particular classes of low-molecular weight compounds. Along with an empirical screening of nanoparticles, we employed physical properties to calculate desorption temperatures for nanoparticles and adapted the existing thermal

model. This study will shed some light on the nanoparticle-assisted laser desorption/ionization-mass spectrometry mechanism.

Introduction

Over the last three decades, nanoparticles (NPs) have found a wide range of chemical applications, including the conservation of art works, information storage, gas sensing, light-emitting devices, fuel and solar cells, and biomedical applications[83]. NPs have found some of their most significant applications as catalysts in synthetic organic chemistry and in the field of analytical and bioanalytical chemistry[83-85]. Zamborini et al. discuss recent developments in nanotechnology that have enabled the production of NPs with unique optical, electronic, magnetic, chemical, mechanical, and catalytic properties that can be tuned by the size, shape, and composition of the NPs. [86]

The unique properties and increased surface area of nanoparticles have given rise to several potential applications of NPs in analytical chemistry measurements[86]. These measurement techniques include various spectroscopic branches and sub-branches of analytical chemistry such as surface plasmon resonance spectroscopy, localized surface plasmon resonance spectroscopy, fluorescence spectroscopy,[87] surface-enhanced Raman spectroscopy, nuclear magnetic resonance (NMR) spectroscopy, magnetic resonance imaging, infrared (IR) spectroscopy and mass spectrometry. [84, 86] NPs have also proven useful in electrochemical detection, chemiresistive sensors, immunoassays, DNA detection and various chromatographic and electrophoretic separations.[84, 86] NP applications in mass spectrometric analysis have focused primarily on enrichment of particular analytes of interest and use as laser

desorption/ionization matrices. [88,12,15] Since the development of matrix-assisted laser desorption/ionization-mass spectrometry (MALDI-MS), NPs have been employed as matrices to aid desorption/ionization[15], and the unique properties of nanoparticle surfaces also enables the functionalization of NPs for selective capturing and MALDI-MS analysis.[89]

MALDI-MS enables sensitive detection of various chemical species from a solid surface.[1-5] MALDI-MS imaging (MALDI-MSI) combines this capability with spatially-resolved sampling and data acquisition. MALDI-MSI allows for the two-dimensional visualization of the spatial distribution of biomolecules without extraction, purification, or separation of analytes.[3] MALDI-MSI is a unique imaging technique for non-target specific discoveries since analyte molecules are ablated, ionized, and detected directly from tissue without labeling on any specific targets.[5] MALDI-MSI has been employed to visualize distributions of several biomolecules, including proteins, peptides, metabolites, amino acids, lipids, carbohydrates, and nucleotides, in various tissue samples and in diverse fields such as medicine, agriculture, biology, pharmacology, and pathology.[2, 3]

Low-molecular weight organic compounds, such as 2,5-dihydroxybenzoic acid (DHB) 1,5-diaminonaphthalene (DAN), 9-aminoacridine (9-AA), etc. are common MALDI-MS matrices. These MALDI-MS matrices tend to give strong background signals in the low mass region (m/z < ~500) and can interfere with analysis of small metabolite compounds.[12] In addition, low-molecular weight metabolites span a variety of chemical functionalities, and optimal ionization of all metabolites of interest by a single matrix is

almost impossible. For these reasons, the development of new MALDI-MS matrices for the analysis of low-molecular weight compounds is receiving a great deal of interest.

The use of nanoparticles as matrices instead of organic compounds, referred to as nanoparticle-assisted laser desorption ionization (NALDI-MS), is receiving increased interest because nanoparticles typically exhibit high laser absorptivity, low volatility, matrix homogeneity, and low background signals.[12],[90],[91] Recent developments in nanotechnology have made NPs of various sizes, shapes and compositions commercially available or easily synthesizable.[12] Three popular classes of NPs adopted in NALDI-MS include metals such as Pt,[14, 92, 93] Au,[14, 90-92, 94-100] Ag[14, 59, 101-103] and Cu,[14] metal oxides such as WO_3,[104] ZnO,[105] SiO_2,[92] TiO_2,[78, 92, 104, 106-109] and Fe_3O_4[77, 92, 110] and carbon-based nanoparticles made of diamond,[16, 108, 111] graphite/colloidal graphite,[16, 112] and graphene oxide.[113-118] The NPs in this study were selected based on the literature search and absorbance at 355 nm (3.47eV), as the system used for this study uses a frequency-tripled Nd:YAG laser operating at 355 nm.

In NALDI-MS, NPs absorb the incident photons and transfer energy to analytes, which leads to desorption and ionization of the analyte.[91] Most NPs give significantly reduced or no background signals compared to organic matrices, due to the high melting/boiling point of these inorganic materials. There are many variables that affect performance of NPs in NALDI: intrinsic properties such as chemical composition, heat capacity, and band gap; extrinsic properties such as size and morphology; and experimental variables such as laser fluence and the concentration, pH and ionic strength of the sample solutions.[91] . Ideal NPs should strongly absorb photons at the laser wavelength and transfer energy effectively to analytes for desorption and

ionization, while minimizing background signal and fragmentation of analyte molecules.[91] Some NPs have specific functionalities that can selectively capture and ionize certain analytes.[91] Ag and Au NPs, for example, are effective for thiol-containing molecules due to their strong adsorption to Ag and Au surfaces, while TiO_2 and Fe_3O_4 NPs are effective for enediol groups and phosphate groups respectively.[91]

The energy transfer from NPs to analytes is thought to occur via a thermally-driven process,[13, 14] similar to the “rapid heating” mechanism proposed by Tanaka et al.[15] The temperature at the sample surface peaks at the end of the laser pulse and depends on the laser fluence, absorption properties of the particles, and heat diffusion over the duration of the laser pulse.[13] Theoretical calculations can be performed to compare the relative peak temperatures for different nanoparticle matrices. In the previous calculations, the heat transport that takes place between the nanoparticles and the surroundings is neglected. [13, 14] Because this calculation assumes complete absorption of the incident light by the particle surface and neglects heat loss to the underlying MALDI plate or surrounding gas, these calculations are useful mostly as relative comparisons and fail to explain the relative effectiveness of one NP type over others.

In addition to internal energy transfer from NPs to analyte, alternative desorption mechanisms have also been proposed for NALDI processes.[16] The different binding affinities between analytes and NPs results in different partitioning of internal energy. The surface properties of the NPs affect desorption and ionization by lower-energy processes.[119] Also, phase transitions or destruction of the NPs are involved in the desorption mechanism(s) of metal oxides.[16] The amount of energy required to disrupt

the NP's surface structure affects their ionization ability.[112] In the case of metal NPs, the melting point affects the ionization efficiency.[14, 120] The processes involved in nanoparticle-assisted laser desorption/ionization are still not completely understood and in this study seeks to better understand the NALDI mechanism. However, because of the complexity of the process and the wide variety of analytes of interest, an empirical study of several NP matrix candidates is needed.

In this study, we have performed a large-scale screening of different nanoparticles for their effectiveness in ionization of a wide variety of plant metabolites. The nanoparticles we used for the screening include: metal nanoparticles (Au, Ag, Pt, Cu), metal oxide nanoparticles (TiO_2, SnO_2, ZnO, AZO [aluminum-doped zinc oxide], Fe_3O_4, WO_3), and carbon-based nanoparticles (boron doped nano-diamond, graphite, graphene oxide). Plant metabolites used for the screening include: small organic acids (malic acid, vanillic acid, ascorbic acid phosphoenolpyruvic acid, glycerol 3-phosphate, phosphocholine), sugars (sucrose, glucose 6-phosphate), amino acids (glutamic acid, isoleucine, asparagine), biotin (vitamin H) co-enzyme A, glycerolipids (including phospholipids), fatty acid (oleic acid), and terpene (parthenolide).The molecular structures of all the metabolites are shown in Figures 1 and 2 as water-soluble and water-insoluble compounds. We expect that this metabolite screening will improve our understanding of the NALDI-MS ionization mechanism, by comparing our empirical results with corrected calculations employing the physical and chemical properties of NPs.

EXPERIMENTAL

Materials

Iron (II) chloride tetrahydrate (99.0%), iron (III) chloride hexahydrate (> 97.0%), tin (II) chloride dehydrate (98%), and zinc (II) acetate dehydrate (98%) were purchased from Strem Chemicals, Inc. (Newburyport, MA, USA). Ethanol (200 proof), nitric acid (Certified ACS Plus- 69.4%), sodium hydroxide, methanol (Certified ACS Plus) and ammonium hydroxide (Certified ACS Plus) were purchased from Fisher Scientific (Waltham, MA, USA). Isopropyl alcohol (LCMS Chromasolv®), chloroform (HPLC Chromasolv® Plus), 2,5-dihydroxybenzoic acid (98.0%), 1,5-diaminonaphthalene (97.0%) and 9-aminoacridine hydrochloride monohydrate (98.0%) were purchased from Sigma Aldrich (St. Louis, MO, USA). Titanium (IV) n-butoxide (99.0%) was purchased from Acros Organics (Pittsburgh, PA, USA).

Commercially available NPs were purchased. Metal oxide NPs aluminum-doped zinc oxide (AZO; zinc oxide NPs doped with 2 wt% aluminum oxide, 99.99%, 15 nm) and tungsten oxide (WO_3; 99.95%, 23- 65 nm), metal NPs Au (99.95%, 15 nm), Ag (99.99%, 20 nm), and Cu (99.90%, 40 nm), and boron doped nano-diamond (BDND) NPs (Carbon conc. >98.3%, doped with 3wt% boron, 3-10 nm) were purchased from US Research Nanomaterials, Inc. (Houston, TX, USA). The BDND NPs have various functional groups (OH, CN, C=O, COOH, C-O-C) attached to the carbon atoms on their surfaces. Pt NPs (97.0%, 3-7 nm) were obtained from Strem Chemicals, Inc. (Newburyport, MA, USA). Colloidal graphite (5 wt% in isopropanol, aerosol spray) was purchased from Alfa Aesar (Ward Hill, MA, USA). The colloidal graphite has a wide size distribution; the majority of particles are between 400 and 1000 nm. The graphene oxide

(0.5 wt% in water; N002-PS-0.5) was purchased from Angstron Materials Inc. (Dayton, OH, USA) and contains ≥ 46% of carbon, ≤ 46% of oxygen, ≤ 3 % of hydrogen and ≤ 0.5 %of nitrogen. The average thickness is 1.0 – 1.2 nm and the average size is ~554 nm. It commonly contains -OH, C=O, COOH and C-O-C functional groups.

The metabolite standards malic acid, glucose, glucose 6-phosphate, sucrose, asparagine, glutamic acid, isoleucine, coenzyme-A trilithum salt, biotin (vitamin-H), glycerol tripalmitate, vanillic acid (Fluka) and oleic acid (Fluka) were purchased from Sigma Aldrich (St. Louis, MO, USA). Ascorbic acid was purchased from Fisher Science Education (Nazareth, PA, USA). Phosphoenolpyruvic acid monopotassium salt was purchased from Alfa-Aesar (Ward Hill, MA, USA). Rac-Glycerol 1-phosphate disodium salt hexahydrate was purchased from Santa Cruz Biotechnology, Inc. (Dallas, Texas, U.S.A.). Phosphocholine chloride sodium salt hydrate was purchased from Tokyo Chemical Industry Co. Ltd (TCI, Philadelphia, PA, USA). Parthenolide was purchased from Tocris Bioscience (Bristol, United Kingdom). Phospholipid mixture [L-α-Phosphatidylcholine, 20% (Soy) (Soy Total Lipid Extract)] was purchased from Avanti Polar Lipids, Inc. (Alabaster, AL, USA).

Fe_3O_4 Nanoparticle Synthesis

For the synthesis of Fe_3O_4 NPs, 1 mL of 2 M $FeCl_2 \cdot 4H_2O$ and 4 mL of 1 M $FeCl_3 \cdot 6H_2O$ were mixed together under continuous stirring, 50 mL of 0.5 M NH_4OH were added drop wise and stirring continued for 30 min. The resulting solution was then centrifuged at 4500 rpm for 10 min and washed with deionized water. The washing and

centrifugation steps were repeated until the supernatant was neutral. After washing with water, the precipitate was washed once with methanol and allowed to dry overnight.[6, 81]

TiO_2 Nanoparticle Synthesis

Titanium dioxide nanoparticles were synthesized as described by Shrivas *et al*.[78] Titanium (IV) n-butoxide (17 mL) and ethanol (8 mL) were mixed in a 50 mL round bottom flask by stirring for 10 min at room temperature and then cooled in an ice/water bath. Concentrated nitric acid (375 µL) was mixed with 8 mL of ethanol and added drop wise to the titanium butoxide mixture under vigorous stirring while being cooled in an ice/water bath. Stirring was continued for 30 minutes after the addition was completed.[6],

SnO_2 Nanoparticle Synthesis

Tin (II) chloride dihydrate (2.50 g) was added to deionized water (400 mL) and stirred at room temperature for 2 days. The material was precipitated out by centrifugation (4500 rpm, 10 min) and the precipitate washed with each water and ethanol (200 proof) twice.

ZnO Nanoparticle Synthesis

Zinc (II) acetate dihydrate (0.66 g) was dissolved in ethanol (200 proof) and stirred for 15 min. Sodium hydroxide (1.5 g) was added and the solution stirred for 6 h at room temperature. The material was precipitated by centrifugation (4500 rpm, 10 min) and washed two times with methanol.

Sample Preparation for Plant Metabolite Standard Analysis

For analysis, nanoparticles were suspended at concentrations ranging from 50 µM to 460 mM in isopropanol (see Optimization of Nanoparticle Concentrations), and these suspensions used to determine the optimal NPs concentration for the study. Each NP suspension was mixed with a standard solution containing either water-soluble standards (malic acid, vanillic acid, ascorbic acid, phosphoenolpyruvic acid, glycerol 3-phosphate, phosphocholine, glucose, sucrose, glucose 6-phosphate, glutamic acid, isoleucine, asparagine, biotin [vitamin H] and co-enzyme A) in water or water-insoluble standards (glycerol tripalmitate, assorted phospholipids, oleic acid and parthenolide) in chloroform. All standard compounds were present at 100 µM final concentration. The mixture of NPs and metabolites was sprayed onto a stainless steel MALDI target using a home-made oscillating capillary nebulizer.[121]

Nanoparticle Application with Oscillating Capillary Nebulizer

The details of matrix application using oscillating capillary nebulizer (OCN) is described in our recent method paper[121] and only briefly described here. Water-soluble and water-insoluble standards were dissolved in water and chloroform, respectively. Each NP suspension prepared in isopropyl alcohol was mixed with either of the standards in 10:1 volume ratio, to have 100 µM final concentration for standards. The metabolite standard and NP suspension mixture was sprayed on stainless steel MALDI target plates using a modified airbrush as OCN.[6], [121] The typical procedure for NP application was as follows: A 500 µL syringe was filled up with a mixture of NP

suspension and metabolite standards and a blank target plate was placed ~8 cm below the tip of the OCN. The nebulizing gas (N_2) flow was started and pressure was adjusted to ~40 psi. The flow rate of the syringe pump was set at 50 µL min^{-1} and the blank target plate surface was monitored to ensure matrix is being applied and wetting is minimal. The pump was stopped and blank plate was replaced by the MALDI target plates below the tip of the OCN. Finally the syringe pump was turned and spray 500 µL of suspension and mixture of 100 µM standards sprayed that covers a ~2 cm uniformly.[6], [121]

Optimization of Nanoparticle Concentrations

To find optimal NP concentrations for water-soluble and water-insoluble metabolite standards in both positive and negative mode, we tested various concentrations of NPs at 100 µM final concentration for metabolite standards. The soy lipid extract is a mixture of various phospholipids and the final concentration of soy lipid extract was kept at 0.1 mg mL^{-1}. The NPs were suspended in isopropyl alcohol for various concentration ranges selected based on preliminary experiments and/or from the literature. The metal oxide concentrations screened were 0.25, 0.50, 1.0, 2.5, 5.0, and 10.0 mM; the concentrations studied for BDND NPs were 0.1, 0.25, 0.50, 1.0, 2.5, 5.0, 10.0, 25.0, 50.0, 100 and 200 mM; those for graphene oxide were 0.50, 1.0, 5.0, 10.0, 25.0, 50.0, 100.0 and 150 mM; and those for colloidal graphite were 5.0, 10.0, 25.0, 50.0, 100.0, 150.0, 200 and 462 mM.

In the initial study of metal NPs, we employed colloidal solutions of Pt (10 ppm), Au (20 ppm), Ag (20 ppm), and Cu (10 ppm) form Purest Colloids

(www.purestcolloids.com). The optimum concentration is, however, higher than the original concentrations. Therefore, we tried NP aqueous dispersions of Pt (1000 ppm), Au (1000 ppm), Ag (2000 ppm), and Cu 40 nm from US Research Nanomaterials instead. The NP aqueous dispersions, however, required surfactants to be remain dispersed in water, which produced significant backgrounds in low mass region (m/z < 500). This was overcome by employing Pt NPs (3-7 nm obtained from obtained from Strem Chemicals, Inc.) and Au (15 nm), Ag (20 nm) Nano-powder from US Research Nanomaterials, Inc. The concentration studied for the metal NPs were 0.1, 0.25. 0.50, 1.0, 2.5, 5.0, 10.0, 20.0 and 40.0 mM.

For MS analysis, three replicates of 250 spectra were collected from two standard samples with each NP concentration. Table 1 summarizes the optimum NP concentrations determined and used for the main study. It should be noted that minor changes in NP concentration do not affect the final results.

MS Data Acquisition

A linear ion trap-orbitrap mass spectrometer with MALDI ion source (MALDI LTQ-Orbitrap Discovery; Thermo Scientific, San Jose, CA, USA) was used for this study. The instrument was modified to use an external frequency-tripled, diode-pumped Nd:YAG laser operating at 355 nm and 60 Hz (UVFQ; Elforlight Ltd., Daventry, UK). Conditions such as laser energy and number of shots were individually optimized for each type of NP (Table 2), and 250 spectra were collected with 3 replicates each from two independent samples for each NP concentration. The laser spot size was estimated to be ~20 μm as determined from laser burn marks on a thin film of α-

cyanohydroxycinnamic acid. Orbitrap scans were acquired over the *m/z* range of 50 to 1200.

Optimization of Laser Energy

The laser energy was individually optimized for each type of NP. For optimization best suitable concentration found in the preliminary experiments was used. Laser energy was optimized by scanning over an area of the sprayed mixture of NPs and standard plant metabolites and increasing the energy stepwise over the course of the scan. The energy was optimized for water-soluble and water-insoluble plant metabolites in both positive and negative mode. For each NP, the laser pump diode energy was increased from 80% to 90% in increments of 0.5% at 10 laser shots per MS scan and each energy setting was maintained for 1 min (~ 50 scans). The pulse energies were measured at the laser aperture and due to some inevitable energy loss at each of the beam steering and focusing elements, the actual fluences at the sample surface are expected to be slightly lower.[122] Table 2 summarizes the threshold and the optimum laser energy for both positive and negative mode and both water-soluble and water-insoluble used for plant metabolites analysis for each type of nanoparticle employed in this study.

RESULTS AND DISCUSSION

Results

In positive mode, most metabolite standards were detected as alkali metal adducts, primarily $[M+Na]^+$ and $[M+K]^+$. Some compounds also showed appreciable lithium adduct signal, $[M+Li]^+$, likely due to the lithium present as a counter-ion in the co-

enzyme A standard. In the case of Ag NPs, some metabolites were also detected as the $[M+Ag]^+$ species. For ion yield comparisons in positive mode, alkali adduct and protonated signals were summed. Experiments were performed in two stages. First, we optimized experimental conditions for each NP matrix, namely finding optimal laser energy and concentration. The final data set was acquired using the optimized experimental conditions in three additional replicate experiments. Experiments for water-soluble and water-insoluble standard compounds were performed separately from one another.

Table 3 summarizes ion intensities for positive-mode screening of water-soluble and water-insoluble metabolite standards. For water-soluble compounds, Fe_3O_4, AZO, BDND, and Cu NPs were most effective for a broad range of compounds. Fe_3O_4 NPs, in particular, gave the broadest coverage for the investigated classes. BDND NPs showed the next broadest coverage, comparable to Fe_3O_4 NPs except for ascorbic acid and phosphates, probably due to excess energy transfer to labile compounds. In contrast, graphene oxide NPs provided strong signals for phosphorylated compounds, even slightly better than Fe_3O_4 NPs. AZO and Cu NPs are comparable, better than the rest of other NPs but inferior to Fe_3O_4 or BDND NP. It is important to note that the organic matrices DHB and DAN were largely ineffective for small molecules except for phosphocholine and choline, the only standards detected as protonated species. This is attributed to the competition of matrix molecules with analytes for alkali ion adduct formation. Figure 3 shows NALDI/MALDI-MS spectra for water-soluble standards obtained with selected Fe_3O_4, AZO, WO_3, BDND, graphene oxide, Ag NPs and DHB in positive mode.

In the analysis of water-insoluble compounds, TiO_2 NPs were most efficient for a wide range of compounds, including parthenolide, a terpenoid which is very difficult to detect using any organic matrices. Parthenolide could also be effectively detected by BDND and graphene oxide NPs, but they were virtually ineffective for most other water-insoluble compounds. TiO_2 and Fe_3O_4 NPs were efficient for glycerolipids but they are complementary to each other; Fe_3O_4 NPs were more effective for TAG and PA, and TiO_2 NP was more effective for DAG. WO_3 NPs were effective for some compounds including biotin and coenzyme A, but appear to cause extensive fragmentation for glycerolipids, as apparent from high fragment ion signals for DAG and PC. Other NPs were mostly ineffective for water-insoluble compounds. The organic matrix DHB outperformed all NPs for PC but was comparable with Fe_3O_4 NP for PA.

Table 4 summarizes ion intensities for negative-mode screening of water-soluble and water-insoluble metabolite standards. In negative-mode analyses, all compounds were detected as the deprotonated form, $[M-H]^-$. WO_3 NPs were not used for negative mode screening because they generate significant background peaks with almost no analyte ion signals in negative mode according to a preliminary study. Metal oxide NPs were generally not efficient in negative mode. Parthenolide, a terpene compound difficult to ionize using any other matrices, was weakly detected with TiO_2 NP; however, its ion signal was two orders of magnitude lower than in positive mode. Among carbon-based NPs, BDND and colloidal graphite produced good signals for amino acids, biotin, and low-molecular weight acids (LMWA; i.e., malic and vanillic acids), while graphene oxide showed effectiveness for phosphate compounds, fatty acid, and adenine fragment of coenzyme-A. Among metal NPs, silver was most effective for phosphate compounds,

ascorbic acid, oleic acid, and lyso-PI, suggesting it is more effective overall then other NP matrices for fragile compounds. By comparison, the organic matrix DAN was found to be the most efficient matrix for a wide class of compounds. It is noteworthy that some NPs are comparable to DAN for select classes of compounds (i.e., BDND for LMWA and amino acids; silver for phosphate compounds, ascorbic acid, oleic acid, and lyso-PI; and colloidal graphite for biotin and oleic acid), suggesting they can be used for selective detection of certain classes of compounds.

Overall, Fe_3O_4 and BDND NPs offer the best performance in positive mode, while TiO_2 and graphene oxide NPs are better for selected compounds. These NP matrices outperformed the organic matrix DHB, except for the phosphocholine and phospholipid standards. In negative mode, however, the organic matrix DAN is superior to NP matrices overall, although carbon-based NPs and silver NPs are as effective for selected compounds. It is worth mentioning the possibility of ion suppression effects in the mixtures of standards, which were not investigated in this study. For example, ion suppression of TAG by PC is well known with DHB matrix. This ion suppression effect was easily overcome by Fe_3O_4 NP showing high TAG signal, probably because it does not produce ion signals for PC. Figures 3, 4, 5 and 6 show spectra for the best-ionizing NPs and organic matrices in positive mode and negative mode for both water soluble and water-insoluble plant metabolites.

Discussion

Carbon Nanoparticles.

Carbon exists in different allotropic forms and diverse types of synthetic substrate materials with different physicochemical properties, such as thermal conductivity, specific heat capacity, and melting point.[123, 124],[124] A rapid laser-induced heating of substrates, leading to the desorption/ionization of analytes, is widely regarded as the NALDI mechanism.[16] A study by Tang *et al.* suggests diamond NPs, with the highest extent of internal energy transfer, induce significant fragmentation of the benzylpyridinium thermometer ion. They proposed that the higher ionization energies of diamond NPs (6.9-8.07 eV) relative to graphite NPs (4.39eV)[16] might lead to diamond's high ionization efficiency for LMW metabolites (< *m/z* 500) and lower ionization efficiency for lipids due to greater ion fragmentation. This hypothesis is supported by our observation of lower glucose 6-phosphate signal with BDND in comparison to graphene oxide. The results of the Tang *et al.* study also indicated that increased internal energy transfer is not the only factor behind increased desorption/ionization efficiency. This further confirms that the thermal desorption mechanism can only partly account for the ionization efficiency of NPs.[16]

Graphite was found to produce a high carbon cluster background in comparison to BDND and graphene oxide in both positive and negative mode (Figures 7 and 8). This might be due to the lower laser fluence threshold for graphite ablation (approximately 4 times lower than that for diamond).[125] The weaker bonding/interaction (*i.e.* sp^2-hybridized carbon with interlayer π-π interaction in colloidal graphite vs. strong three-dimensional sp^3-hybridized carbon-carbon bond network in diamond NPs) might

favor the phase transition/destruction of NPs upon laser irradiation[16], which also produces a high carbon cluster background in the *m/z* <500 region. This high carbon cluster background significantly reduces the usefulness of colloidal graphite as a matrix below *m/z* 500. Additionally, the phase transition/destruction of NPs dissipates the laser energy and results in decreased internal energy transfer,[16] which might explain the lower ionization efficiency of colloidal graphite for LMW metabolites.

The electrical and thermal conductivity of graphene oxide have been suggested to aid the ionization efficiency.[115] Similar to colloidal graphite, graphene oxide has sp^2-hybridized carbon, which might favor the phase transition/destruction of NPs upon laser irradiation.[16] The carboxylic acid and hydroxyl groups at the surface of graphene oxide NPs facilitate proton transfer to and from analytes, similar to organic acid matrices. Interestingly, graphene oxide produced significantly lower carbon cluster background in comparison to colloidal graphite in both positive and negative modes. The reason for this low background is not fully understood. The greater phase transition/destruction of NPs upon laser irradiation and lower internal energy transfer in comparison to BDND NPs may explain graphene oxide's lower efficiency for LMW metabolite ionization and higher efficiency for more labile, higher MW lipids. This is further supported by the higher signals observed for labile LMW metabolites such as glucose 6-phosphate, phosphoenolpyruvic acid and glycerol 3-phosphate

Metal and Metal Oxide Nanoparticles.

Crystalline nanoparticles (metals and semiconductor metal oxides) absorb light, which can be transformed to and released as heat. A laser optically excites electrons in

either metals or semiconductor NPs, and the energy thus gained turns into heat that diffuses away from the nanocrystals leading to an increase in the temperature of the surrounding medium. For metal nanoparticles such as silver, gold and copper, in the region of plasmon resonance, heat generation is strong due to the combined motion of many electrons in metals.[126, 127],[127] For semiconductor metal oxide NPs such as titanium dioxide (TiO_2), tin dioxide (SnO_2), zinc oxide (ZnO), aluminum-doped zinc oxide (AZO), iron(II,III) oxide (magnetite) (Fe_3O_4) and tungsten trioxide (WO_3), heat generation is due to excitation of electrons from the valence band to the conduction band,[108], [126] followed by radiation-less deactivation (thermalization), which significantly increases the local temperature of the NP surface.[108] This heat or internal energy generated at the NP surface is then transferred to the analytes that are in contact with the NP surface, causing desorption/ionization.[108] In positive mode ionization, this causes the formation of adducts between the analytes and alkali metal ions.

In negative mode, the analytes are usually thought to lose H^+ (proton) to the photo-ionized matrix.[108] In our experiments, none of the nanoparticle matrices were as efficient in ionizing plant metabolites in negative mode as the organic matrix DAN, which we have previously shown to be an effective matrix for LMW metabolites.[122] The likely reason for the effectiveness of DAN is the presence of two primary amine groups, which readily deprotonate analyte molecules. By comparison, the surface of semiconducting metal oxide NPs do not typically feature functionalities that could readily deprotonate analytes. Furthermore, metal oxides such as TiO_2 and WO_3 (Figure 9) produce a high background of oxide clusters. These oxide clusters suppress ionization of metabolite standards and generally result in very low-intensity signals. Among metal NPs, Ag was

the most efficient negative mode NALDI-MS matrix. The use of Au and Pt NPs was complicated by their tendency to aggregate and settle out of suspension during the application process. Further investigations of these materials using sputter-coating for deposition are discussed in Chapter 5.

Theory for Thermal Desorption Model:

As discussed in the introduction, the energy transfer between matrix and analyte that is required for NALDI is thought to occur via a thermally driven process. The temperature on the NP surface after laser pulse, ΔT, can be calculated by the following equation (1). [13]

$$\Delta T = E_P/(\rho A d C_p) = E_P/(\rho V C_p) \quad (1)$$

E_p: laser energy

A: area of the laser spot

C_p: heat capacity of the nanoparticle material

ρ: density of the nanoparticle material

d: depth of the area heated during laser irradiation

V: volume of heated material under laser spot (A*d)

The physical properties of the nanomaterial such as heat capacity, heat conductivity and bulk density can be obtained from the literature (Table 5). The volume of the heated area is affected by several factors: the penetration depth of the laser light, the heat diffusion length of the nanoparticle material, and the heat diffusion length of the underlying steel substrate. Heat diffusion length (d_{diff}) is defined as “within a

homogeneous medium, the distance heat applied as a pulse (e.g. a laser pulse) will diffuse over a given time".[128] The heat diffusion length can be calculated using laser pulse length as the diffusion time, thermal conductivity, density and specific heat capacity of the NP material (Table 5).[13] The heat diffusion length equation for a single material is presented below:

$$d_{diff} = 2\ (\tau\lambda/\rho C_p)^{1/2} \qquad (2)$$

τ: laser pulse duration (~ 4ns)

λ: heat conductivity of the nanoparticle material

C_p: specific heat capacity of the nanoparticle material

ρ: density of the nanoparticle material

Performing these calculations for the nanoparticle matrix material alone, however, neglects the penetration of incident laser irradiation beneath the matrix surface and subsequent heat transfer to the stainless steel support. In our ultraviolet (UV) absorption study (data not shown), we were able to measure transmission at the optimal concentration of NPs used for NALDI-MS analysis indicating that not all the incident 355 nm light was absorbed. Additionally, some amount of light will be scattered/reflected by the nanoparticle surface. Because of these major omissions, which neglect heat loss to the underlying MALDI plate and overestimate the deposited energy, preliminary calculations gave very high temperature estimates for all NPs, failing to explain why some NPs are better at ionizing plant metabolites.

We therefore developed a refined thermal desorption model by modifying Schoenberg's model [13]. We made the following corrections in the model to account for additional factors.

1) We did not assume that all the laser energy was absorbed by the first layer of NPs and using the bulk property we found the absorbance coefficient, ε, for the nanoparticle material. From the absorbance coefficient (ε), the laser penetration depth can be calculated (1/ε). We summed the heat diffusion length (d_{diff}) and half of penetration depth (1/2ε) to calculate volume of the area heated after laser pulse to solve equation 1.
2) The thickness of the NPs suspension sprayed on the stainless steel target plates can be calculated using concentration, volume, and density of the NPs sprayed, and the area covered by the OCN spray. Table 6 gives the thickness calculated for each NP at the optimal concentration.
3) There are the following two cases for change in temperature (ΔT) after the laser pulse.
    a. Thickness of sprayed NPs is higher than sum of half of penetration depth (1/2ε) and heat diffusion length (d_{diff}) of NPs
    b. Thickness of sprayed NPs is lower than sum of penetration depth half of (1/2ε) and heat diffusion length (d_{diff}) of NPs
4) If the thickness is higher than the sum of heat diffusion length (d_{diff}) and half of penetration depth (1/2ε) then the volume heated after each laser pulse can be calculated using equation 1, using the sum of d_{diff} and 1/2ε as the 'd' term.

$$\Delta T' = E_P/(\rho A d C_p) = E_P/(\rho V C_p) \quad (1)$$

E_p: laser energy

A: area of the laser spot

C_p: heat capacity of the nanoparticle material

ρ: density of the nanoparticle material

d: the sum of d_{diff} and 1/2ε

5) If the thickness is less than the sum of heat diffusion length (d_{diff}) and half of penetration depth (1/2ε), thermal energy will be dissipated to the stainless steel plate. The use of half the penetration depth rather than the full depth provides a more accurate approximation of the amount of heat diffused to calculate the heated volume. The temperature increase after each laser pulse can then be calculated by the following equation;

$$\Delta T'' = E_P/[(\rho VC_p)_{NPs} + (\rho VC_p)_{SS}] \quad (4)$$

$(\rho VCP)_{NPs}$: density, volume, and heat capacity of NPs

$(\rho VC_p)_{SS}$: density, volume, and heat capacity of stainless steel

6) To calculate $(\rho VC_p)_{SS}$ we have to calculate volume of stainless steel plate heated, and for that the heat diffusion length for stainless steel ($d_{diff}SS$) needs to be calculated. This can be calculated by the following equation;

$$d_{diff,ss} = 2\,(\tau_2 \lambda/\rho C_p)^{1/2} \quad (5)$$

τ_2: Laser pulse duration (4nS) – τ_1; duration of dissipation of heat into stainless steel

λ: heat conductivity of the stainless steel: 46 W/m K

C_p: specific heat capacity of the stainless steel: 500 J/kg K

ρ: density of stainless steel: 7889 kg/m^3

7) The time required for the laser energy to penetrate the nanoparticle layer and diffuse to the surface of the plate can be calculated by the following equation:

$\tau_1 = d_1^2 \rho C_p / 4\lambda$ (5)

d_1: difference between thickness of sprayed NPs and laser penetration depth ($1/\varepsilon$)

λ: heat conductivity of the NP material

C_p: specific heat capacity of NP material

ρ: density of the NP material

Following the above steps, we have corrected the thermal model. New temperature values $\Delta T'$ and $\Delta T''$ and are listed for each NP matrix in table 7. The laser energy used for calculations was 0.5 µJ, which in this instrument yields fluences typical of MALDI processes.[129, 130] The temperature increase for colloidal graphite and graphene oxide was not calculated because absorbance coefficients could not be found in the literature.

As shown in Table 7, the calculation for WO_3 gives very high local temperatures (3013 K) upon laser irradiation, leading to extensive fragmentation (and thus low intact ion yield) for various plant metabolites. TiO_2 shows a ΔT value of 1920 K, which also produces significant amount of fragmentation along with the highest intensity signal for terpene compound among all other metal oxides. The ΔT value for Fe_3O_4 is 1260 K, correlating to a typical MALDI temperature and possibly explaining why it appears to be the best NP for desorption/ionization of most metabolites in positive mode. The high ionization energy, electronegativity, and electron affinities of all metal oxides (Table 5) make them less suitable as negative mode matrices. The boron doped nano-diamond

(BDND) produces significantly better signal in comparison to other carbon based NPs which might be attributed to the presence of functionalities such as OH, CN, C=O, COOH, C-O-C and the reduced background due to the stable sp^3 structure.

Among the metal NPs, Cu works best for *m/z* < 500 in positive mode. Ag works well for both positive mode and negative mode and forms an $[M+Ag]^+$ adduct at unsaturation sites of parthenolide and oleic acid. Au and Pt were not efficient matrices due to the fact that they are difficult to keep suspended in solution during sample preparation. Physical vapor deposition of metal NPs and a comparison of this technique to the NP suspension spray technique used here is presented in Chapter 5.

CONCLUSIONS

In this study, we employed thee different types of nanoparticles for the NALDI-MS screening including metal nanoparticles, metal oxide nanoparticles and carbon-based nanoparticles. The empirical screening and corrected thermal desorption/ionization model employing the physical and chemical properties improves our understanding of the NALDI-MS ionization mechanism. The revised model presented here provides a more accurate calculation of the desorption temperature range, enabling rational selection of NP matrices for the thermally-driven NALDI process.

The empirical results of NP screening show that Fe_3O_4, BDND, TiO_2 and graphene oxide NPs are relatively better for ionizing plant metabolites in comparison to other NPs and traditional organic matrices. The better desorption/ionization efficiency of Fe_3O_4 and TiO_2 are supported by the revised thermal model. Future work will be

focused on theoretical calculations for comparison of carbon-based NPs and understanding the thermal desorption mechanism employing the corrected model. In negative mode, the organic matrix DAN is superior to NP matrices overall, although BDND graphene oxide NPs and silver NP are as effective for selected compounds. Interestingly, TiO_2 produces the highest signal intensity for parthenolide in negative mode and this is behavior is unique among all NPs and organic matrices.

In addition to screening the matrices for their general utility in plant metabolite analysis, we used the most suitable NPs for NALDI-MSI of bacterial infections in plant tissue. This study provides information about plant-pathogen interactions, including localized information about metabolic changes and defense responses, and will hopefully assist in controlling the loss of feed-crops due to pathogen infection.[6]

ACKNOWLEDGEMENTS

This work was supported by the U.S. Department of Energy (DOE), Office of Basic Energy Sciences, Division of Chemical Sciences, Geosciences and Biosciences. The Ames Laboratory is operated by Iowa State University under DOE Contract DE-AC02-07CH11358.

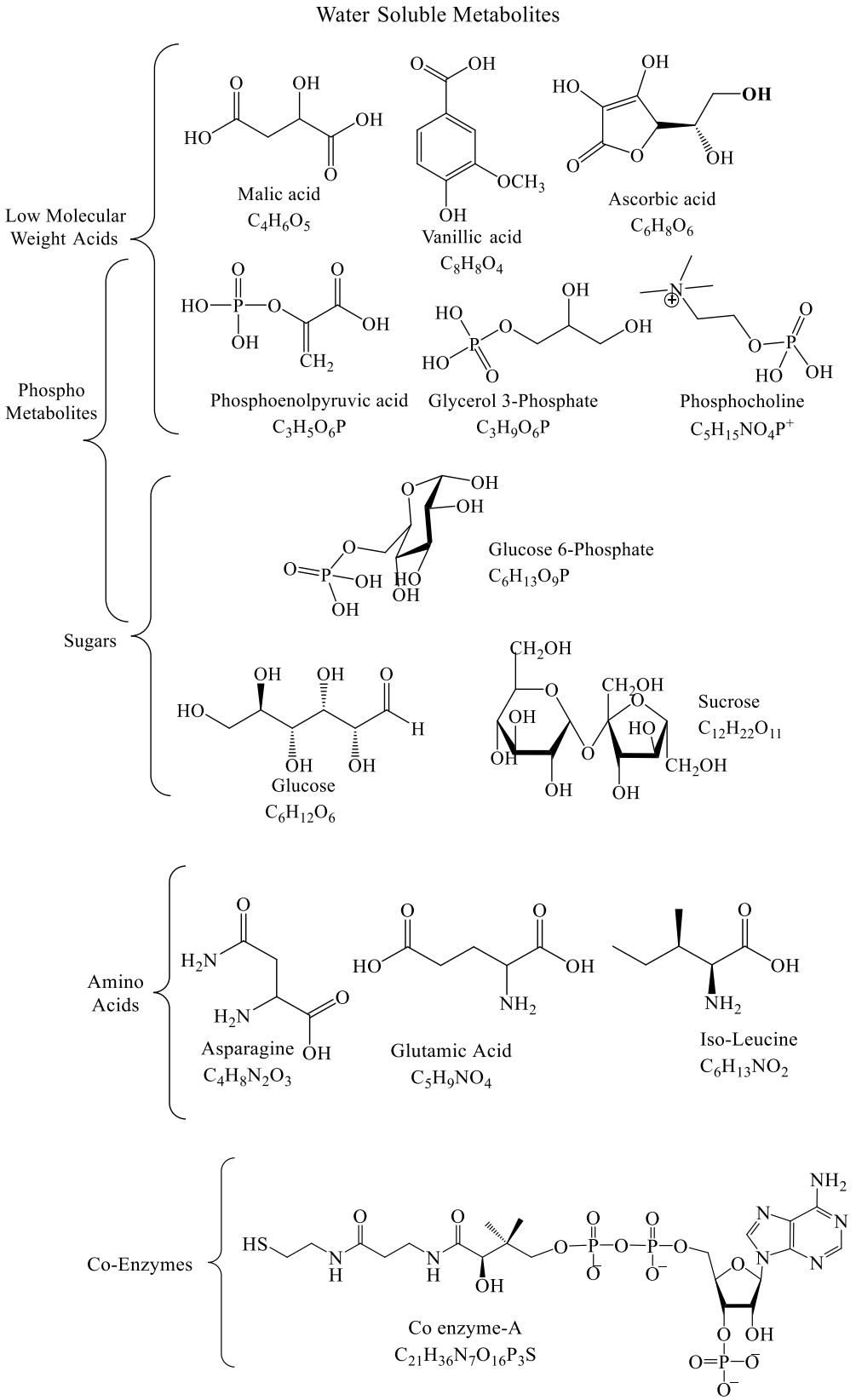

Figure continued

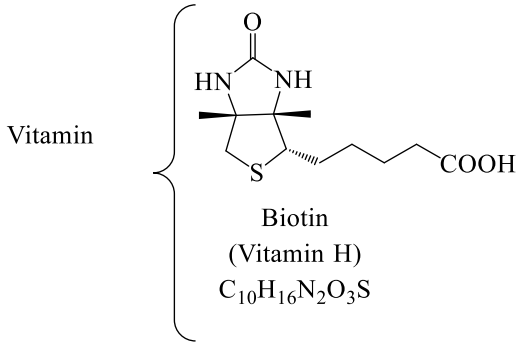

Figure 1: Molecular structure of water-soluble plant metabolites used in this study.

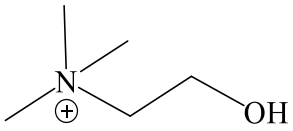

Chemical Formula: $C_5H_{14}NO^+$

*Choline from phosphocholine

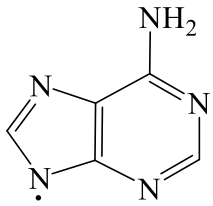

Chemical Formula: $C_5H_4N_5^{\bullet}$+ Na/K

*Adenine from Co enzyme-A

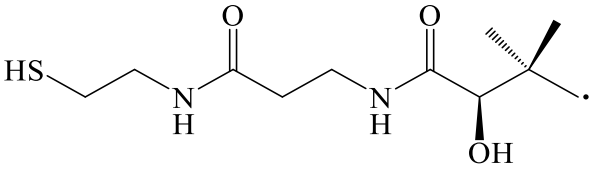

Chemical Formula: $C_{11}H_{21}N_2O_3S^{\bullet}$ + Na/ K

*Side chain from Co enzyme-A

*** Major fragments detected in water-soluble compounds and shown in Table 1.

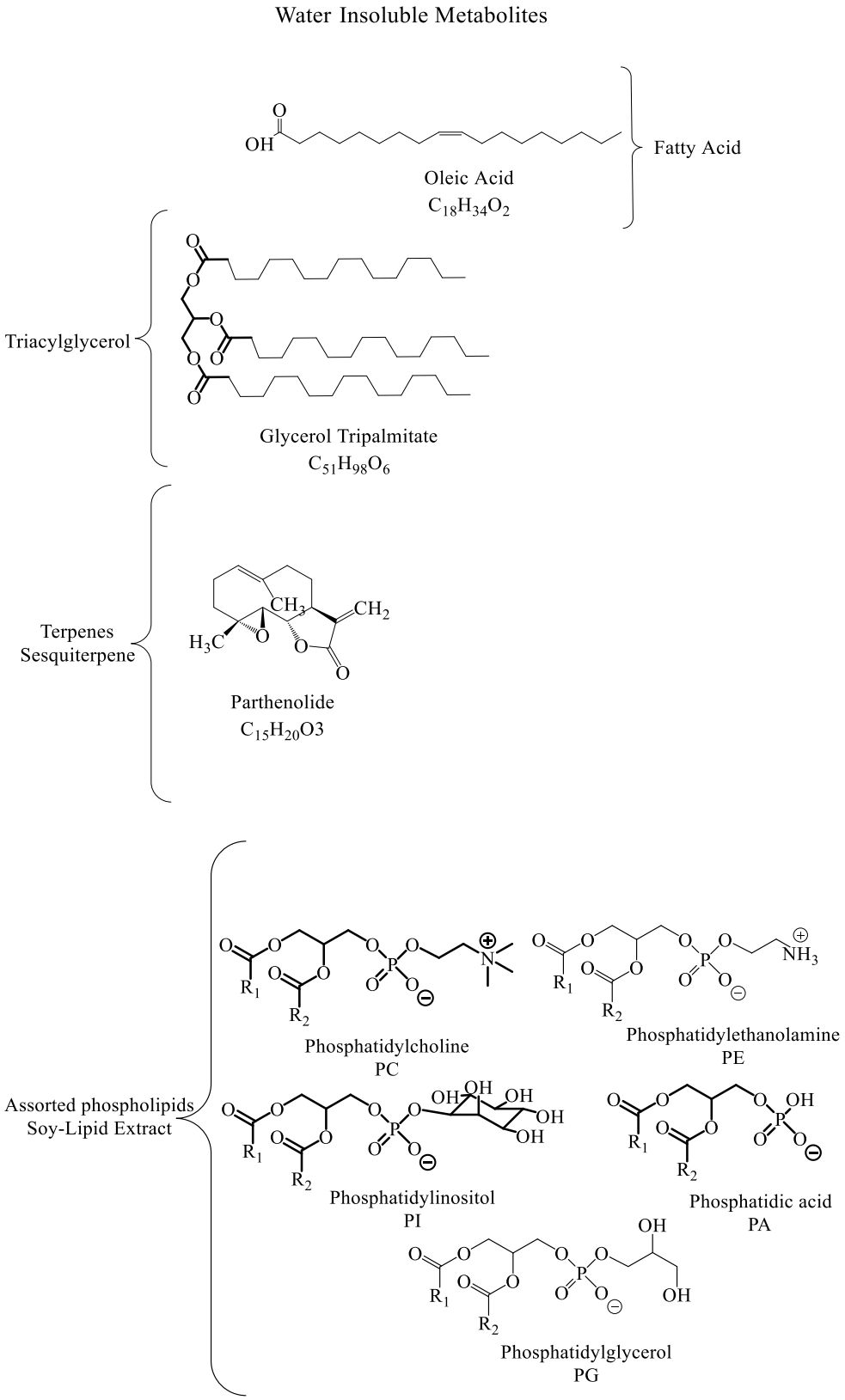

Figure 2: Molecular structure of low-molecular weight water-insoluble plant metabolites

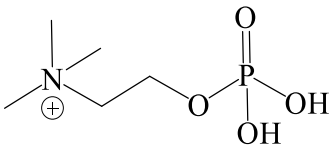

Chemical Formula: $C_5H_{15}NO_4P^+$

*Phosphocholine from phosphatidylcholine

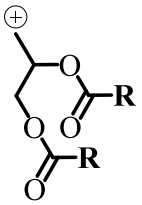

*DAG fragments from Glycerol Tripalmitate and Phospholipids

*** Major fragments detected in water insoluble compounds and shown in Table 2.

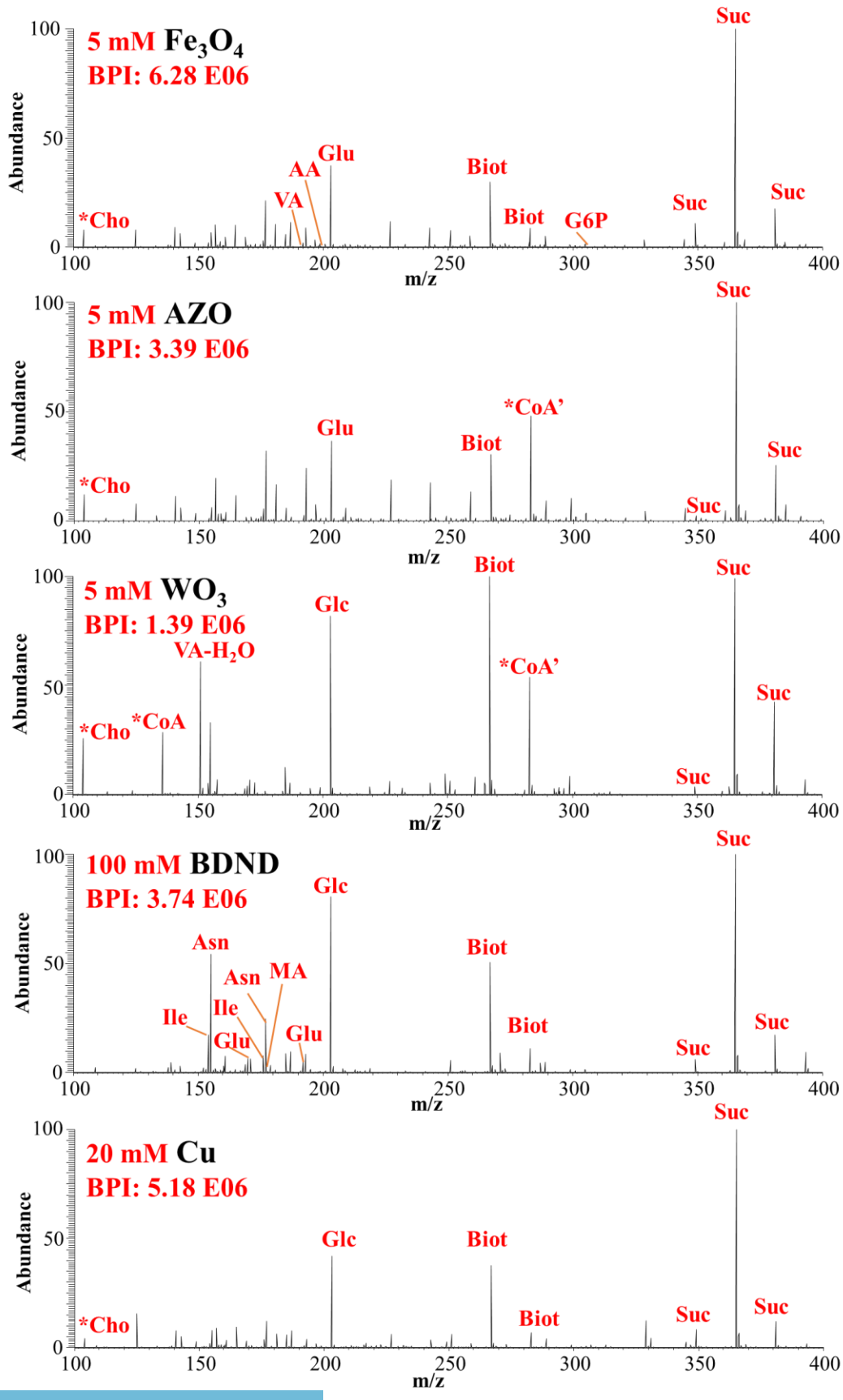

Figure continued

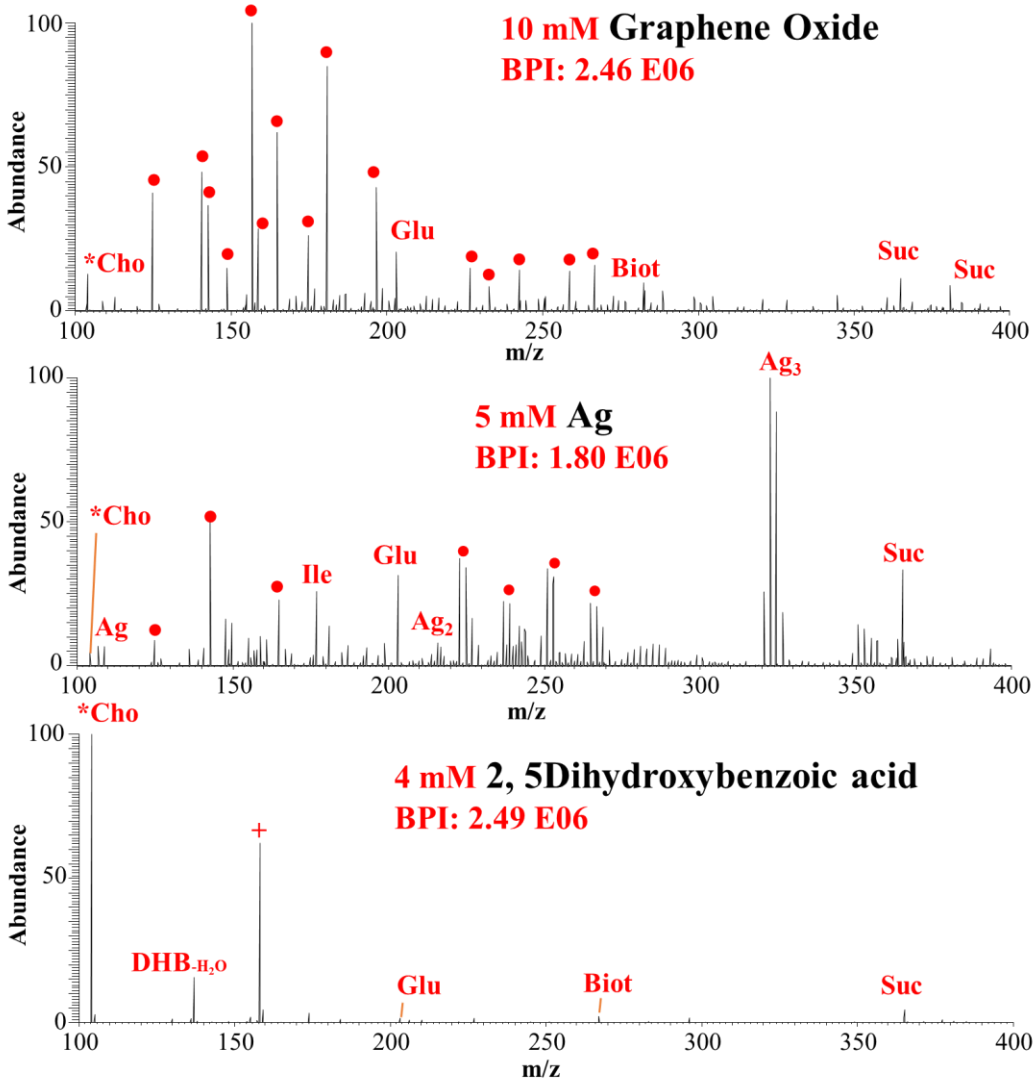

Figure 3: NALDI/MALDI-MS spectra for water-soluble standards obtained with selected NPs and DHB in positive mode. Water-soluble metabolite ions are primarily detected as alkali metal adducts $[M+Na]^+$, $[M+K]^+$ and $[M+Li]^+$. Low-molecular weight acids, amino acids, vitamin H and coenzyme A fragments are also detected as di-alkali metal adducts. *Cho, *CoA, *CoA', VA, MA, AA, Ile, Asn, Glu, Glc, Suc, G6P and Biot represent choline fragment of phosphocholine, adenine fragment of co-enzyme A, slide chain fragment of fragment of co-enzyme A, vanillic acid, malic acid, ascorbic acid, isoleucine, asparagine, glutamic acid, glucose, sucrose, glucose 6-phosphate, and biotin (vitamin-H), respectively. The phosphate fragments with alkali metal adducts were observed and are represented by ●. The contamination pack from is represented by +. BPI is base peak intensity.

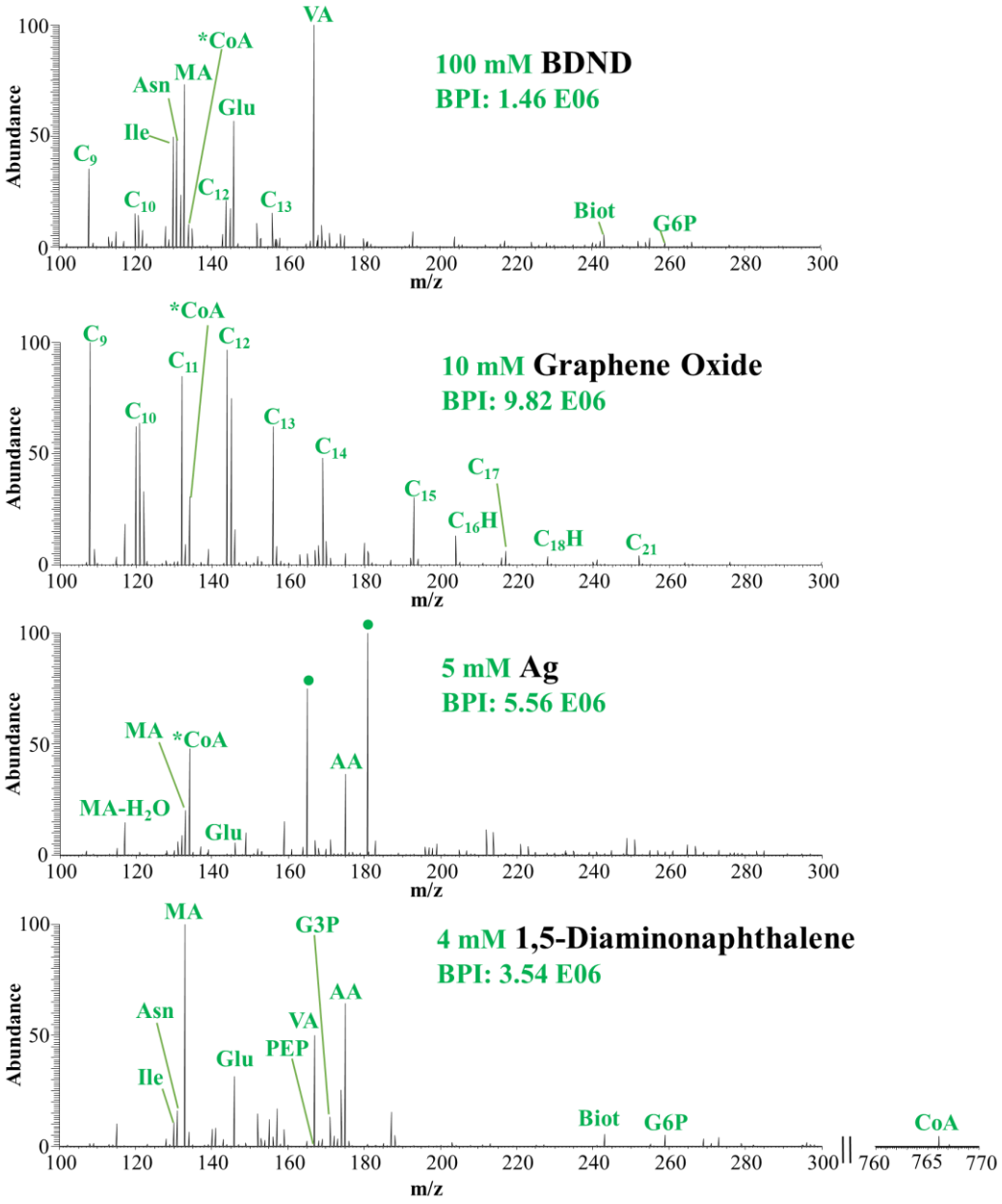

Figure continued

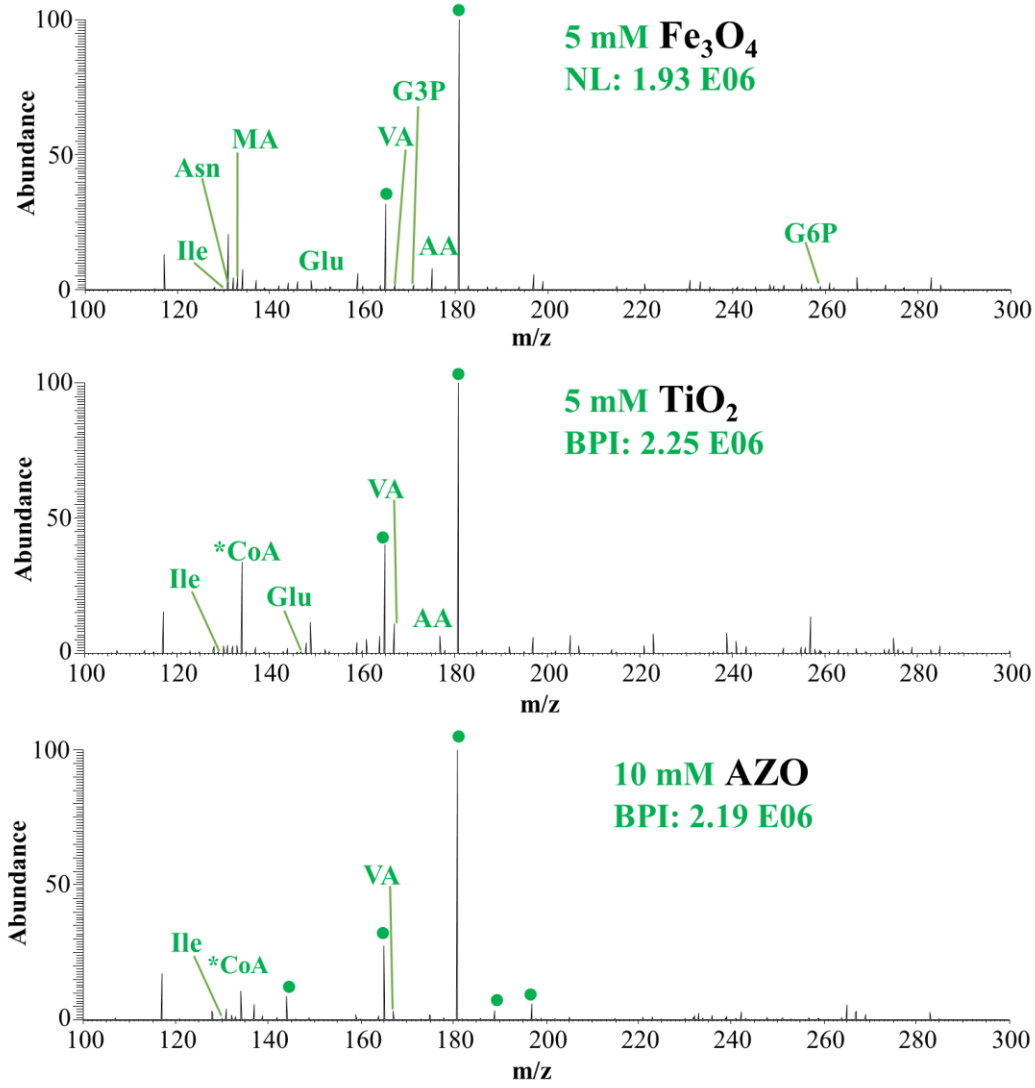

Figure 4: NALDI/MALDI-MS spectra for water-soluble standards in negative mode obtained with selected NPs and DAN. All water-soluble metabolites ions are detected as $[M-H]^-$. *CoA, VA, MA, AA, Ile, Asn, Glu, G6P, Biot and CoA represent adenine fragment of co-enzyme A, vanillic acid, malic acid, ascorbic acid, isoleucine, asparagine, glutamic acid, glucose 6-phosphate biotin (vitamin-H) and co-enzyme A, respectively. The phosphate fragments with alkali metal adducts were observed and are represented by ●. BPI is base peak intensity.

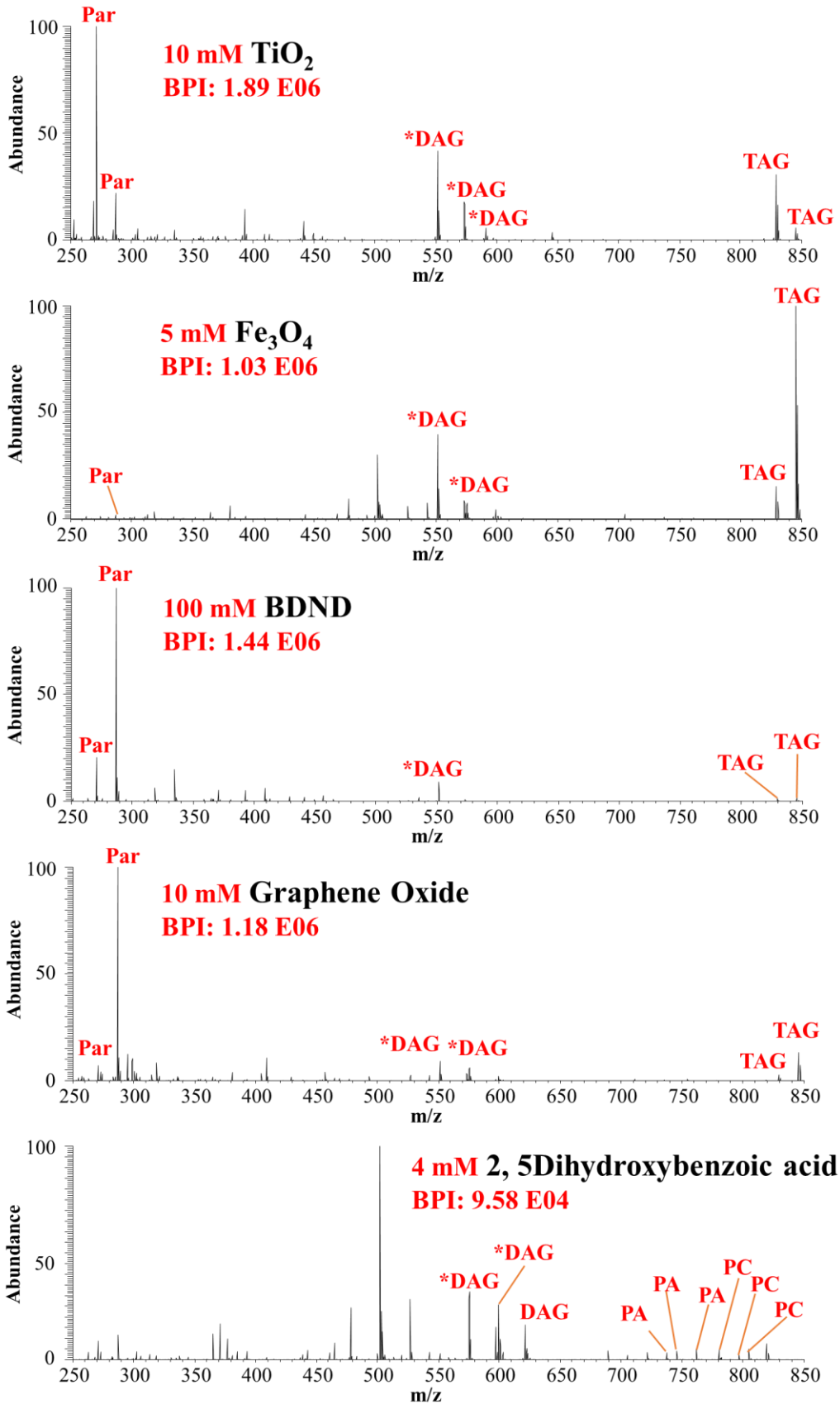

Figure continued

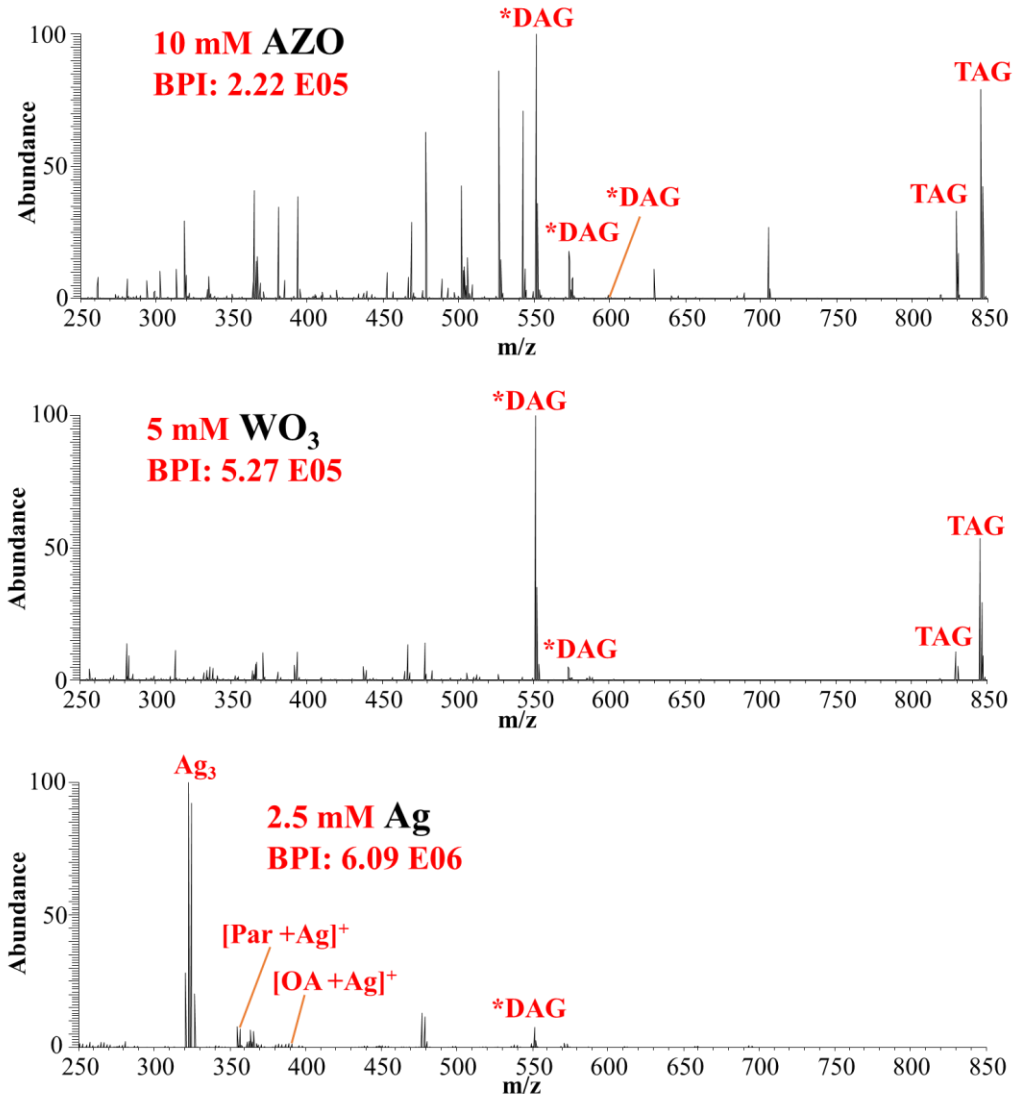

Figure 5. NALDI/MALDI-MS spectra for water-insoluble standards in positive mode obtained with selected NPs and DHB. Water-insoluble metabolite ions are primarily detected as alkali metal adducts $[M+Na]^+$, and $[M+K]^+$. Par, *DAG, TAG, PA and PC represent parthenolide, diacylglycerol fragments, triacylglycerol, phosphatidyl-ethanolamine and phosphatidylcholine, respectively. BPI is base peak intensity.

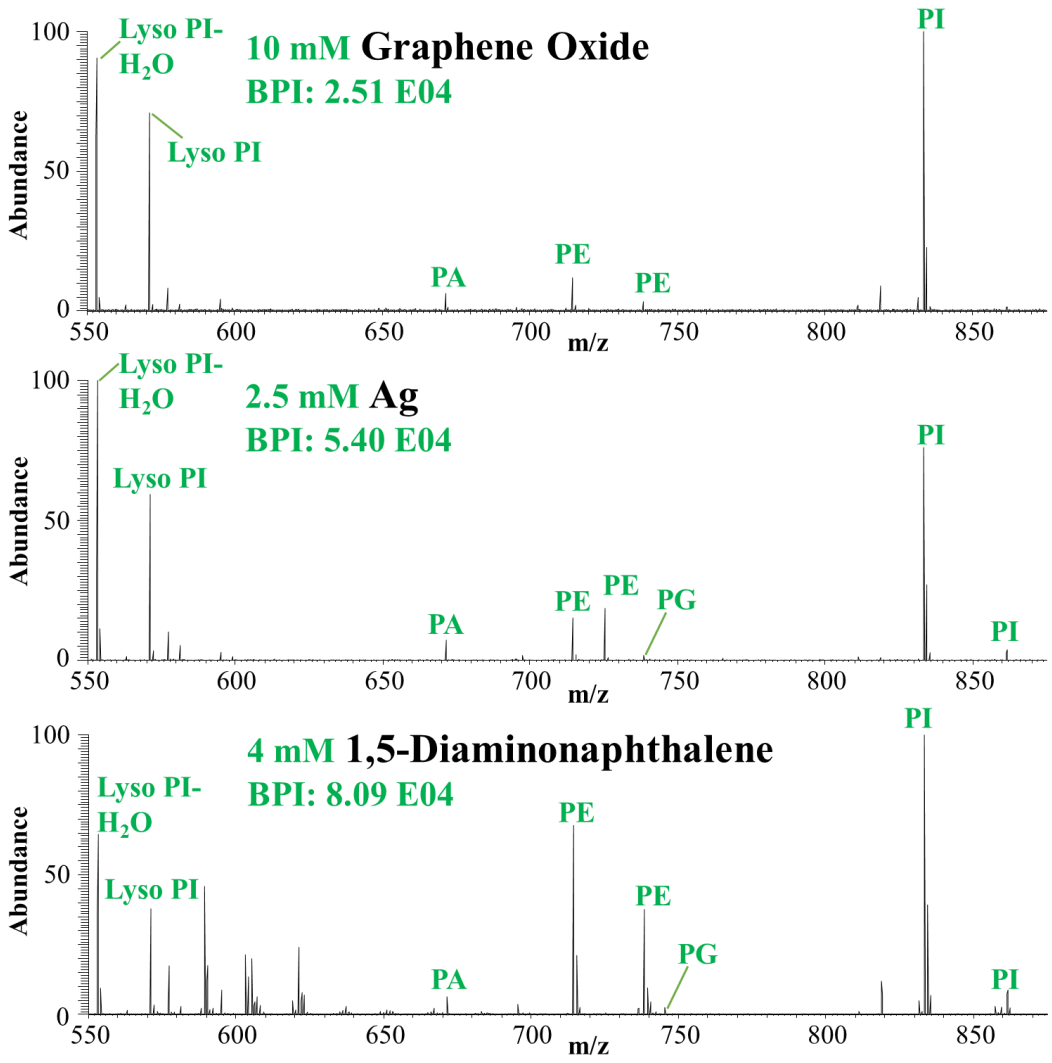

Figure continued

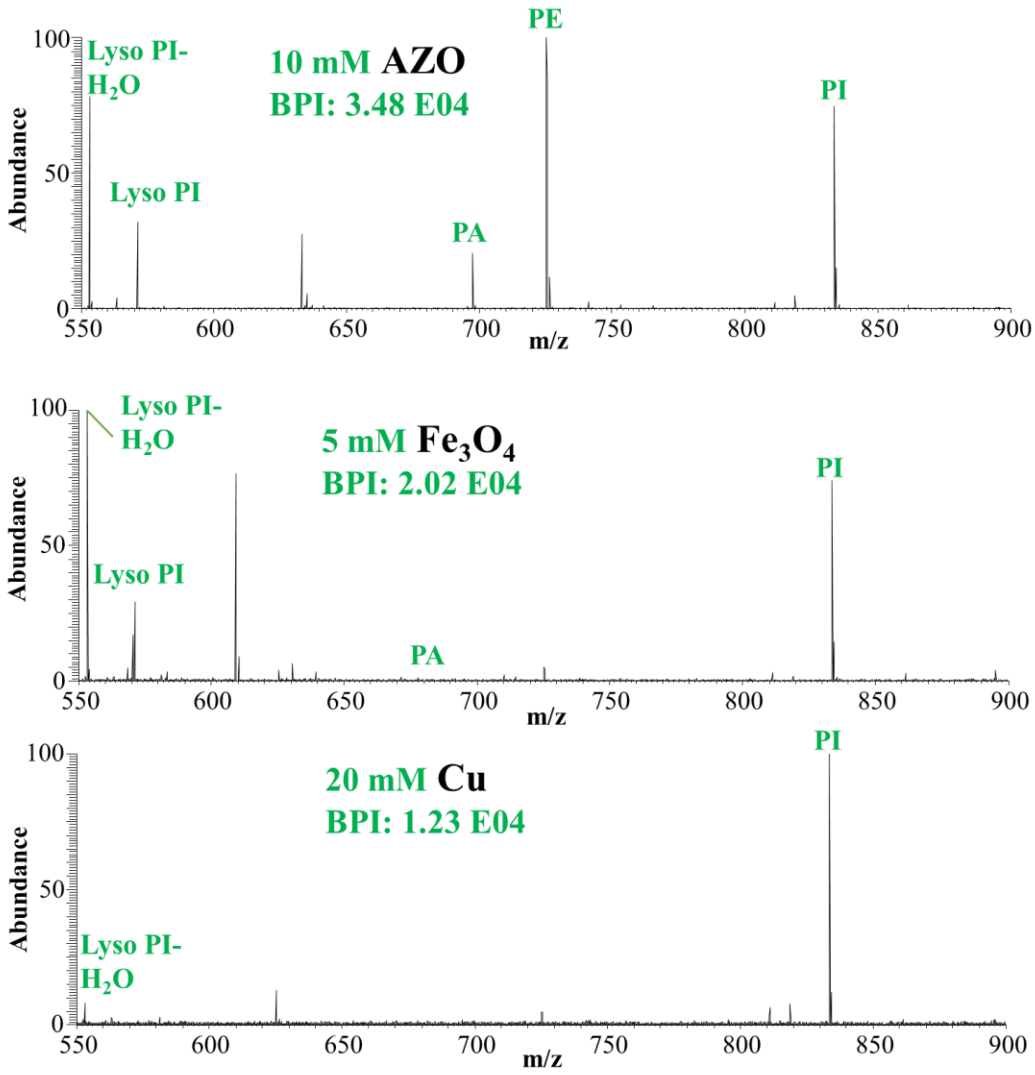

Figure 6: NALDI/MALDI-MS spectra for water-insoluble standards in negative mode obtained with selected NPs and DAN. All water-insoluble metabolites ions are detected as [M-H]-. PA PE, PG, PI and Lyso-PI represent phosphatidic acid, phosphatidylethanolamine, phosphatidylglycerol, phosphatidylinositol and lyso-phosphatidylinositol, respectively. BPI is base peak intensity.

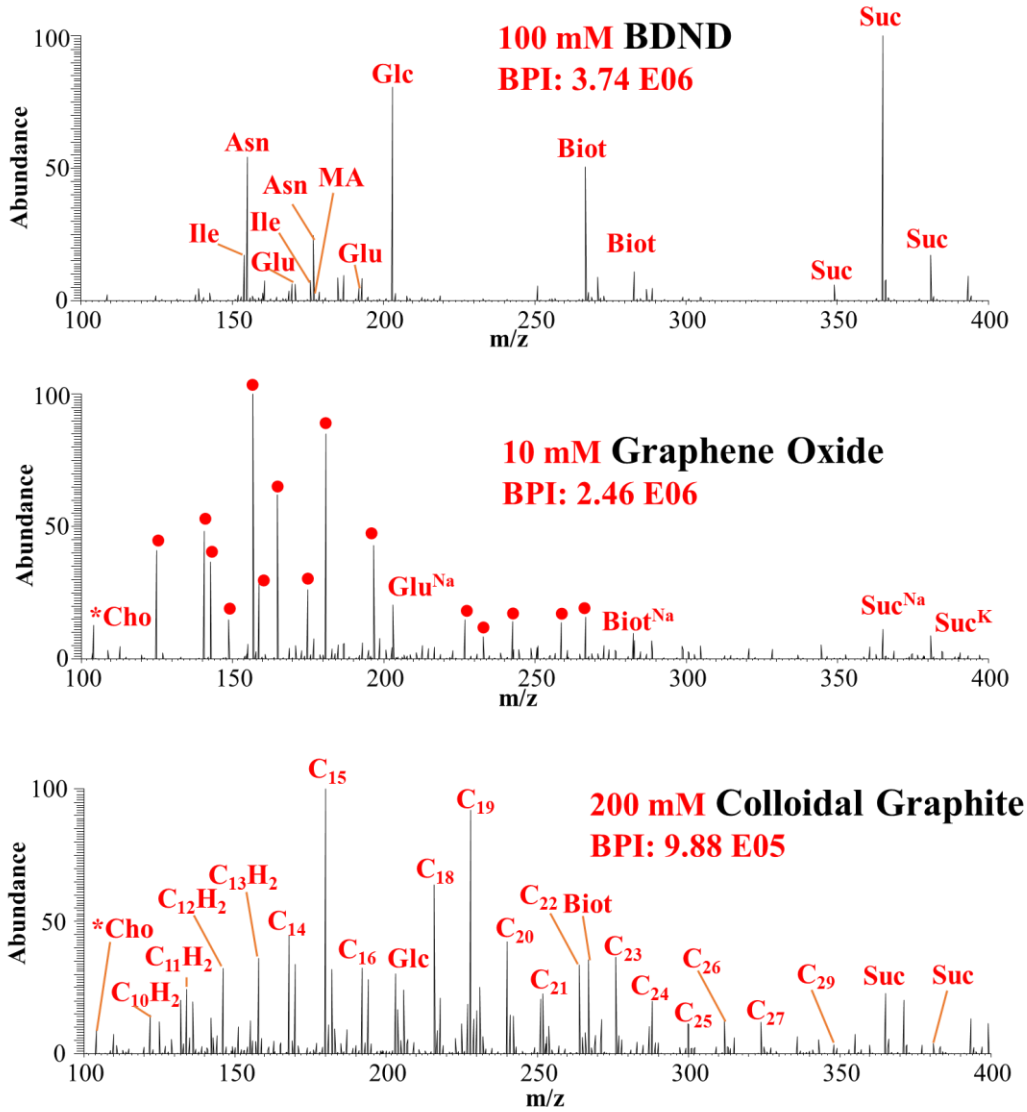

Figure 7: NALDI-MS spectra for water-soluble standards in positive mode obtained with three carbon-based NPs. Water-soluble metabolite ions are primarily detected as alkali metal adducts $[M+Na]^+$, $[M+K]^+$ and $[M+Li]^+$. Low-molecular weight acids, amino acids, vitamin H and coenzyme A fragments are also detected as di-alkali metal adducts. *Cho, Glc, Suc and Biot represents choline fragment of phosphocholine, glucose, sucrose, and biotin (vitamin-H), respectively. The high carbon clusters background $C_{10}H_2$, $C_{11}H_2$, C_{14}, C_{15}…etc. was observed with colloidal graphite. In graphene oxide high intensity phosphate fragments with alkali metal adducts were observed and are represented by ●. BPI is base peak intensity.

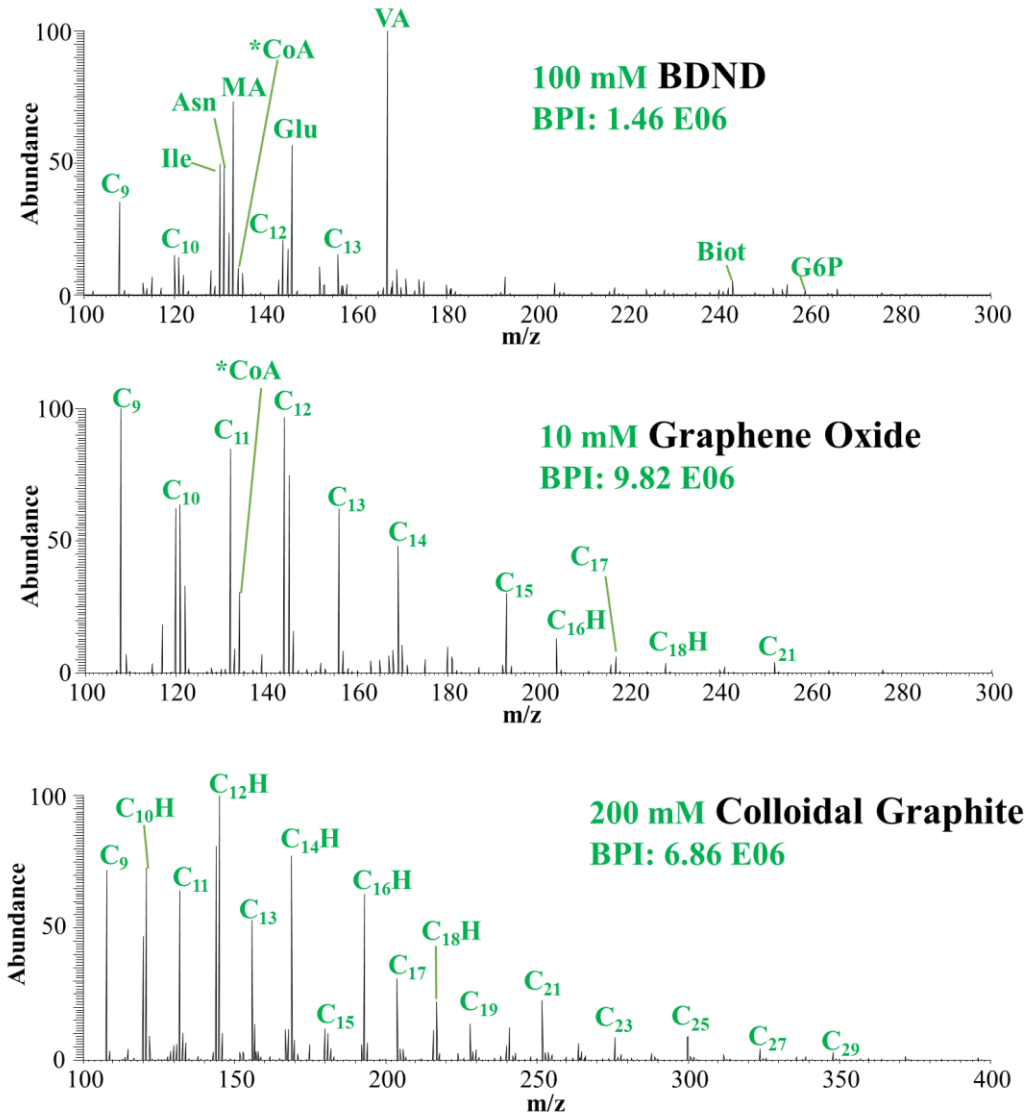

Figure 8: NALDI-MS spectra for water-soluble standards in negative mode obtained with three carbon-based NPs. *CoA, VA, MA, AA, Ile, Asn, Glu, G6P, Biot and CoA represent adenine fragment of co-enzyme A, vanillic acid, malic acid, ascorbic acid, isoleucine, asparagine, glutamic acid, glucose 6-phosphate biotin (vitamin-H) and co-enzyme A, respectively. The high carbon clusters background C_9, $C_{10}H$, C_{11}…etc was observed with colloidal graphite and graphene oxide. BPI is base peak intensity.

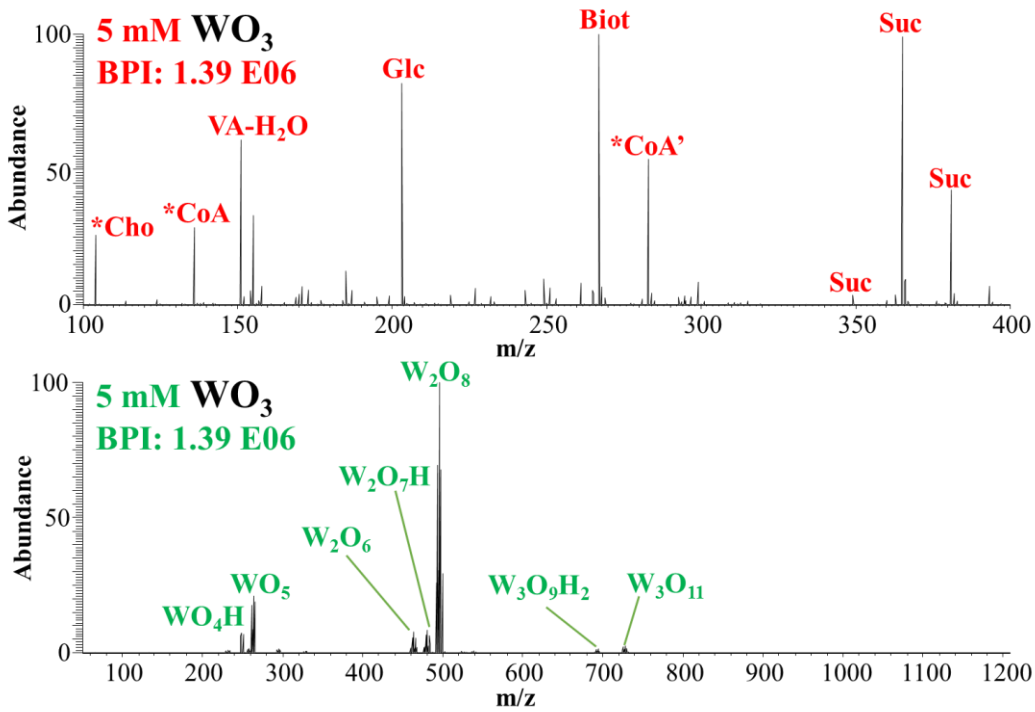

Figure 9: NALDI-MS spectra using WO_3 NPs as matrices to compare ionization efficiency for standard water-soluble metabolites in positive mode and negative mode. In positive mode water-soluble metabolite ions are primarily detected as alkali metal adducts $[M+Na]^+$, $[M+K]^+$ and $[M+Li]^+$. Low-molecular weight acids, amino acids, vitamin H and coenzyme A fragments are also detected as di-alkali metal adducts. *Cho, *CoA, *CoA', VA, MA, AA, Ile, Asn, Glu, Glc, Suc, G6P and Biot represents choline fragment of phosphocholine, adenine fragment of co-enzyme A, slide chain fragment of fragment of co-enzyme A, vanillic acid, malic acid, ascorbic acid, isoleucine, asparagine, glutamic acid, glucose, sucrose, glucose 6-phosphate, and biotin (vitamin-H). In negative mode high background of oxide cluster such as WO_4H, WO_5, W_2O_6, W_2O_7H, W_3O_8, W3O9H2, W_3O_{11} etc. observed. BPI is base peak intensity.

Table 1: Optimized nanoparticle concentrations used in this study

Nanoparticles	Water Soluble		Water Insoluble	
	Positive	Negative	Positive	Negative
WO_3	5.0	-	5.0	-
TiO_2	5.0	5.0	10.0	5.0
Fe_3O_4	5.0	5.0	5.0	5.0
ZnO	10.0	5.0	10.0	5.0
AZO	5.0	10.0	10.0	10.0
SnO_2	10.0	10.0	10.0	10.0
BDND	100.0	100.0	100.0	100.0
Colloidal Graphite	150.0	150.0	150.0	150.0
Graphene Oxide	10.0	10.0	10.0	10.0
Platinum	10.0	2.5	10.0	5.0
Gold	10.0	5.0	10.0	10.0
Silver	5.0	5.0	2.5	2.5
Copper	20.0	5.0	20.0	20.0

Table 2: Threshold and optimum laser energy for each NP. Energy defined by % of maximum pump diode current.

Nanoparticles	Threshold Energy		Optimum Energy	
	Positive	Negative	Positive	Negative
WO_3	80.50	-	82.50	-
TiO_2	80.50	81.00	83.0	83.50
Fe_3O_4	80.00	80.00	82.50	83.50
ZnO	80.50	81.00	82.50	85.00
AZO	80.00	80.00	82.50	83.50
SnO_2	80.50	83.00	85.00	85.00
BDND	81.00	80.50	83.00	84.00
Colloidal Graphite	80.00	80.00	83.00	84.00
Graphene Oxide	80.50	80.00	82.00	83.00
Platinum	80.50	81.50	85.00	87.50
Gold	81.50	82.00	85.00	87.50
Silver	80.00	80.50	83.00	84.00
Copper	80.50	81.00	83.50	84.00

Table 3: Summary of nanoparticle screening in positive mode. Ion signals are compared and presented in a heat map with the maximum ion signal in red for each analyte. All compounds are detected as alkali metal adducts, except PC, phosphocholine, and choline fragments in a molecular ion form and DAG fragment as a protonated form. Low-molecular weight acids, amino acids, vitamin H and Co-enzyme-A fragments are also detected as di-alkali metal adducts. All ion signals from various proton and alkali metal adducts are summed into a single value. * represents fragment ions. PA: phosphatidic acid, PC: phosphatidylcholine, TAG: triacylglycerol, AZO: aluminum-doped zinc oxide, DHB: 2,5-dihydroxybenzoic acid, DAN: 1,5-diaminonaphthalene.

Positive	Water Soluble															Water Insoluble							
	LMW Acid			Phospho Metabolites					Sugars		Amino Acids			Co Enzyme					Lipids				
Nanoparticles	Malic Acid	Vanillic Acid	Ascorbic Acid	Phosphocholine	*Choline	Phosphoenolpyruvic Acid	Glycerol 3-Phosphate	Glucose 6-Phospate	Glucose	Sucrose	Asparagine	Glutamic Acid	Iso-leucine	*Co Enxyme-A (Adenine)	*Co Enzyme-A	Biotin (Vitamin H)	*Phosphocholine (PC)	Parthenolide (Terpene)	Oleic Acid (Fatty Acid)	*DAG	DAG	PA	PC	TAG
WO3	2E+04	1E+04	5E+04	2E+04	4E+05	1E+03	1E+05	3E+04	1E+06	2E+06	6E+05	7E+04	8E+04	5E+05	1E+06	2E+06	2E+06	5E+02	5E+02	7E+05	9E+01	4E+02	4E+02	4E+05
TiO2	7E+02	2E+05	1E+03	4E+02	3E+04	6E+03	4E+05	4E+03	3E+05	4E+05	8E+05	1E+04	9E+05	3E+05	2E+06	5E+06	4E+05	2E+06	1E+05	1E+06	1E+05	4E+02	4E+02	7E+05
Fe3O4	1E+05	2E+05	6E+04	1E+04	5E+05	2E+04	2E+05	1E+05	4E+06	8E+06	3E+06	3E+05	5E+05	7E+04	4E+05	3E+06	1E+06	2E+04	7E+02	5E+05	1E+02	2E+04	1E+03	1E+06
AZO	6E+04	3E+04	3E+04	1E+03	4E+05	6E+03	7E+04	7E+04	2E+06	4E+06	2E+06	2E+05	3E+05	1E+05	2E+06	2E+06	8E+05	3E+03	4E+02	3E+05	1E+02	9E+02	4E+02	2E+05
ZnO	1E+04	2E+04	7E+03	3E+02	5E+03	4E+02	2E+03	2E+03	6E+05	1E+06	4E+05	4E+04	3E+05	7E+03	1E+05	2E+06	2E+05	6E+02	1E+03	1E+05	1E+02	4E+02	4E+02	7E+04
SnO2	1E+04	2E+03	2E+03	3E+02	7E+03	3E+02	7E+03	3E+03	3E+05	5E+05	2E+05	2E+04	7E+04	8E+03	7E+03	4E+05	5E+05	4E+02	3E+02	1E+05	2E+02	4E+02	4E+02	2E+04
Diamond	3E+05	1E+05	2E+03	6E+02	3E+03	8E+03	1E+05	1E+04	4E+06	5E+06	4E+06	5E+05	1E+06	3E+04	3E+04	3E+06	2E+04	2E+06	3E+03	1E+05	1E+02	4E+02	4E+02	4E+04
Coll. Graphite	4E+04	5E+03	3E+03	6E+02	8E+04	3E+02	1E+04	1E+03	4E+05	3E+05	2E+05	1E+04	6E+04	2E+05	5E+04	7E+05	2E+05	9E+03	2E+02	1E+05	1E+02	4E+02	4E+02	4E+04
Graphene Oxi.	1E+05	3E+04	3E+03	9E+04	3E+05	2E+04	5E+05	3E+05	6E+05	5E+05	6E+05	9E+04	9E+04	8E+04	3E+05	8E+05	2E+05	1E+06	6E+03	2E+05	9E+01	1E+03	5E+02	2E+05
Platinum	2E+04	1E+05	2E+04	3E+02	9E+03	3E+02	5E+03	5E+03	1E+06	1E+06	5E+05	1E+05	6E+05	3E+04	1E+04	7E+05	1E+04	2E+02	2E+02	2E+05	1E+02	4E+02	4E+02	3E+04
Gold	2E+04	1E+04	7E+03	6E+02	1E+04	2E+02	4E+04	1E+04	3E+05	6E+05	3E+05	4E+04	1E+05	4E+04	2E+04	5E+05	1E+05	1E+03	3E+02	1E+05	9E+01	4E+02	4E+02	3E+04
Silver	8E+04	4E+03	2E+04	4E+03	7E+04	6E+03	2E+05	6E+04	8E+05	8E+05	7E+05	8E+04	9E+04	2E+05	5E+04	8E+05	5E+04	1E+06	2E+05	5E+05	1E+02	4E+02	4E+02	7E+02
Copper	6E+04	6E+04	1E+04	2E+03	2E+05	1E+04	7E+04	4E+04	3E+06	6E+06	1E+06	1E+05	3E+05	8E+04	1E+05	3E+06	9E+04	4E+03	2E+02	2E+05	9E+01	4E+02	4E+02	9E+04
DHB	5E+03	5E+02	7E+03	6E+04	3E+06	3E+02	4E+04	1E+04	1E+05	3E+05	1E+05	8E+03	9E+03	1E+05	4E+04	3E+05	9E+05	2E+04	2E+02	3E+04	1E+02	2E+04	1E+04	5E+02
DAN	6E+02	6E+02	5E+02	1E+06	2E+06	2E+02	8E+02	5E+02	8E+03	3E+04	3E+03	2E+04	1E+03	3E+04	1E+05	4E+04	8E+05	7E+03	2E+02	6E+03	9E+01	5E+02	5E+02	3E+02

Table 4: Summary of nanoparticle screening in negative mode, presented in a heat map with the maximum ion signal in green for each analyte**.** All compounds are detected as a deprotonated form. PE: phosphatidylethanolamine, PG: phosphatidylglycerol, PI: phosphatidylinositol.

Negative	Water Soluble														Water Insoluble						
	LMW Acid			Phospho Metabolites				Amino Acids			Co Enzyme						Phospho Lipids				
Nanoparticles	Malic Acid	Vanillic Acid	Ascorbic Acid	Phosphoenolpyruvic Acid	Glycerol 3-Phosphate	Glucose 6-Phospate	Sucrose (Sugar)	Asparagine	Glutamic Acid	Iso-leucine	*Co Enxyme-A (Adenine)	*Co Enzyme-A	Co Enzyme-A	Biotin (Vitamin H)	Parthenolide (Terpene)	Oleic Acid (Fatty Acid)	Lyso- PI	PA	PE	PG	PI
TiO2	1E+04	3E+05	1E+02	5E+04	1E+02	3E+02	1E+03	4E+04	2E+04	7E+04	2E+06	9E+01	8E+01	8E+04	3E+04	3E+05	6E+02	8E+02	1E+03	1E+02	4E+02
Fe3O4	1E+05	6E+04	2E+05	7E+04	4E+04	5E+04	4E+03	6E+04	7E+04	8E+03	1E+06	1E+02	9E+01	2E+04	9E+01	2E+05	3E+04	9E+02	6E+02	8E+01	1E+04
AZO	2E+04	5E+04	9E+04	2E+04	8E+02	2E+04	1E+03	4E+04	3E+04	1E+04	4E+05	9E+01	1E+02	9E+03	9E+01	4E+04	4E+04	7E+02	4E+02	8E+01	2E+04
ZnO	4E+04	3E+05	9E+04	6E+02	3E+03	4E+02	5E+03	8E+04	7E+04	2E+05	2E+05	2E+02	9E+01	9E+04	9E+01	1E+05	9E+02	4E+02	4E+02	1E+02	4E+02
SnO2	1E+05	6E+04	7E+04	4E+02	2E+04	1E+03	9E+02	3E+04	4E+04	4E+04	6E+04	2E+02	9E+01	2E+04	1E+02	6E+04	2E+03	6E+02	5E+02	1E+02	5E+02
Diamond	1E+06	1E+06	7E+04	2E+03	9E+04	1E+04	3E+04	7E+05	8E+05	7E+05	2E+05	1E+02	1E+02	9E+04	7E+02	5E+04	6E+02	5E+02	4E+02	9E+01	4E+02
Coll. Graphite	7E+05	8E+05	4E+05	5E+04	2E+05	4E+03	3E+04	4E+05	5E+05	4E+05	6E+05	2E+02	9E+01	2E+05	2E+02	2E+05	3E+04	6E+02	2E+03	1E+02	9E+03
Graphene Oxi.	4E+05	6E+05	4E+05	2E+05	3E+05	1E+04	9E+03	2E+05	2E+05	2E+05	6E+06	1E+02	9E+01	8E+04	9E+03	6E+05	4E+04	2E+03	3E+03	1E+02	2E+04
Platinum	2E+04	2E+05	4E+04	3E+02	5E+03	3E+02	1E+03	3E+04	3E+04	2E+05	3E+05	9E+01	9E+01	4E+04	9E+01	1E+05	1E+03	5E+02	5E+02	1E+02	1E+03
Gold	1E+05	2E+05	1E+05	1E+03	2E+04	6E+02	5E+02	4E+04	5E+04	1E+05	2E+05	1E+02	9E+01	5E+04	1E+02	2E+05	4E+03	5E+02	1E+03	1E+02	1E+03
Silver	1E+06	4E+05	2E+06	3E+05	4E+05	1E+05	2E+02	2E+05	3E+05	1E+05	5E+06	8E+01	1E+02	3E+04	3E+02	8E+05	9E+04	4E+03	1E+04	2E+02	4E+04
Copper	3E+04	5E+04	4E+04	1E+03	2E+03	4E+02	1E+02	1E+04	1E+04	4E+04	2E+05	1E+02	1E+02	2E+03	1E+02	1E+05	2E+03	6E+02	4E+02	1E+02	1E+04
9-AA	2E+04	2E+04	2E+04	6E+04	1E+04	1E+03	7E+02	1E+03	2E+03	1E+03	2E+05	4E+02	7E+02	2E+03	9E+01	7E+04	8E+04	4E+03	2E+03	1E+02	1E+05
DAN	3E+06	2E+06	2E+06	3E+05	5E+05	2E+05	1E+05	6E+05	1E+06	4E+05	2E+05	2E+04	2E+05	2E+05	3E+02	3E+05	1E+05	1E+04	9E+04	2E+03	1E+05

Table 5: Nanoparticle size used in this study and bulk physical properties. [131-143]

NPs	Size (nm)	ε Absorbance Coefficient	Energy Gap (eV)	Density (ρ) kg/ m^3	Heat Capacity (CP) J /kg K	Heat Conductivity (λ) W/ m K	Melting Point K	Ionization Energy K J/mol	Electro-negativity	Electron Affinity K J/mol
WO3	23-65	4.00E+04	3.20	7160	318	1.63	1746	20592	6.6	321
TiO2	10	1.77E+05	3.20	4300	683	11.7	2116	9269	5.8	418
Fe3O4	11	3.60E+05	2.20	5170	653	27.4	1870	-	-	-
ZnO	5-6'	1.60E+05	3.20	5600	497	23.4	2248	2770	5.7	415
AZO	15	1.00E+05	3.35	5600	497	23.4	2248	714	-	396
SnO2	2	1.00E+05	3.47	6950	349	40	1903	9295	5.8	463
BDND	3-10'	5.00+E04	3.5-5.5	3500	509	42	3823	1087	2.6	122
Coll. Graphite	1000 (Flake)	-	0.40	2200	686	470	3970	1087	2.6	122
Graphene Oxi.	554 (1-1.2)	-	0.40	1900	686	470	3970	1087	2.6	122
Platinum	3-7'	8.77E+05	4.70-5.74	21500	133	71.6	2042	870	2.3	205
Gold	15	6.12E+05	2.38	19300	129	317	1338	890	2.5	119
Silver	20	5.02E+05	3.10	10500	235	429	1235	731	1.9	126
Copper	40	6.62E+05	2.10	8960	385	401	1357	746	1.9	223

Table 6: Thickness calculation for each nanoparticle at their optimal concentration.

NPs	Concentration (mM)	Volume (mL)	Density ($\mu g/cm^3$)	Area (cm^2)	Molecular Weight (g)	Mass (µg)	Volume (cm^3) M/ρ	Thickness (µm)
WO3	5.00	0.5	7.16E+06	2.54	231.84	5.80E+02	8.09E-05	0.318
TiO2	10.00	0.5	4.30E+06	2.54	79.87	3.99E+02	9.29E-05	0.365
Fe3O4	5.00	0.5	5.17E+06	2.54	231.53	5.79E+02	1.12E-04	0.440
ZnO	10.00	0.5	5.60E+06	2.54	81.41	4.07E+02	7.27E-05	0.286
AZO	10.00	0.5	5.60E+06	2.54	81.41	4.07E+02	7.27E-05	0.286
SnO2	10.00	0.5	6.95E+06	2.54	150.71	7.54E+02	1.08E-04	0.426
Diamond	100.00	0.5	3.50E+06	2.54	12.00	6.00E+02	1.71E-04	0.674
Coll. Graphite	150.00	0.5	2.20E+06	2.54	12.00	9.00E+02	4.09E-04	1.608
Graphene Oxi.	10.00	0.5	2.20E+06	2.54	28.00	1.40E+02	6.36E-05	0.250
Platinum	10.00	0.5	2.15E+07	2.54	195.08	9.75E+02	4.54E-05	0.178
Gold	10.00	0.5	1.93E+07	2.54	196.97	9.85E+02	5.10E-05	0.201
Silver	5.00	0.5	1.05E+07	2.54	107.87	2.70E+02	2.57E-05	0.050
Copper	20.00	0.5	8.96E+06	2.54	63.55	6.35E+02	7.09E-05	0.279

Table 7: Temperature calculations using revised thermal model. Nanoparticles for which the sum of heat diffusion length and half the penetration depth (d_{diff} + 1/2ε) is higher than thickness of spared NPs are in bold. ΔT' is the temperature calculated using NP thickness as depth, while ΔT" is the temperature calculated using the sum of heat diffusion length and half the penetration depth as depth

NPs	Heat Diffusion Length D_{diff} (um)	Penetration Depth 1/ε (um)	D_{diff} + 1/2ε um	Thickness of Sprayed NPs (μm)	ΔT' (K)	Δ T" (K)
WO3	0.107	0.250	0.232	**0.3183**	3013	-
TiO2	0.252	0.057	0.281	**0.3651**	1930	-
Fe3O4	0.360	0.028	0.374	**0.4402**	1260	-
ZnO	0.367	0.063	**0.398**	0.2858	-	741
AZO	0.367	0.100	**0.417**	0.2858	-	741
SnO2	0.514	0.100	**0.564**	0.4263	-	667
BDND	0.614	0.200	**0.714**	0.6740	-	624
Coll. Graphite	2.232	-	-	1.6084		
Graphene Oxi.	2.402	-	-	0.2502		
Platinum	0.633	0.011	**0.639**	0.1784	-	739
Gold	1.427	0.016	**1.435**	0.2006	-	722
Silver	1.668	0.020	**1.678**	0.0505	-	870
Copper	1.364	0.015	**1.371**	0.2788	-	597

.

CHAPTER 5

SOLVENT-FREE METAL NANOPARTICLE APPLICATION AND COMPARISON FOR NANOPARTICLE-ASSISTED LASER DESORPTION/IONIZATION-MASS SPECTROMETRY OF PLANT METABOLITES

Gargey B. Yagnik and Young Jin Lee

Abstract

We have compared two metal nanoparticle (NP) application techniques – solvent-free sputter coating (physical vapor deposition [PVD]) and spraying using an oscillating capillary nebulizer (OCN) – for nanoparticle-assisted laser desorption/ionization-mass spectrometry (NALDI-MS) to detect low-molecular weight (LMW) plant metabolites and for eventual application to NALDI-MS imaging. This study shows that metal nanoparticles such as gold have a strong tendency to aggregate, which limits their efficiency in desorption/ionization of various classes of plant metabolites. Solvent-free argon sputter coating was found to be an effective and homogeneous method for NP application that avoided this aggregation problem. It was also found that intermediate-pressure sputter coating oxidized some metals such as copper, and reduced their efficacy as matrices. Overall, this study serves as an extension of our empirical matrix screening to find effective matrices to ionize particular classes of plant metabolites which are difficult to ionize using traditional organic matrices. It also provides insight into the NALDI-MS ionization mechanism.

Introduction

As discussed in the previous chapter (Chapter 4), various nanoparticles (NPs) have been utilized for NALDI-MS for the detection of low-molecular weight (LMW) compounds. Compared to conventional matrices such as 2,5-dihydroxybenzoic acid (DHB) 1,5-diaminonaphthalene (DAN), and 9-aminoacridine (9-AA), advantages of NP matrices include: low background signal, higher absorptivity, non-volatility, and homogeneous applicability. In our previous study we performed a large-scale screening of NPs for their effectiveness in ionizing a wide variety of low-molecular weight plant metabolites. The NPs in our previous study include various metal, metal oxide, and carbon-based NPs. The standard metabolite compounds used for the screening in that work represent various classes of plant metabolites such as small organic acids, sugars, amino acids, a vitamin, a co-enzyme, glycerolipids (including phospholipids), fatty acids and terpenes.

As an extension to this prior work, the work described here compares metal NPs applied as a suspension to metal NPs deposited on a sample via sputter coating (physical vapor deposition, PVD). As mentioned in Chapter 4, metal NPs such Au[14, 92] [90, 91, 94-98, 100], Ag[14, 59, 101-103], and Cu[14] have become popular nanoparticle matrices, and in some studies, metal NPs such as Ag[144, 145] and Au[29, 146, 147] have been applied by sputter coating. To our knowledge there has been no comparative study between metal NPs applied as a liquid suspension and metal NPs applied by sputter coating. In NALDI-MS and NALDI-MS imaging analysis, it is difficult to keep NPs suspended in solution and apply them homogeneously to the sample surface. Metal NPs like gold

tend to aggregate at the bottom of the suspension during the spraying process. PVD circumvents this suspension and enables homogeneous application of metal NPs.

The metals employed in this study for NPs are gold (Au), silver (Ag) and copper (Cu). Plant metabolites used for the screening are the same as those in Chapter 4, which include: small organic acids (malic acid, vanillic acid, ascorbic acid phosphoenolpyruvic acid, glycerol 3-phosphate, phosphocholine), sugars (sucrose, glucose 6-phosphate), amino acids (glutamic acid, isoleucine, asparagine), biotin (vitamin H), co-enzyme A, glycerolipids (including phospholipids), a fatty acid (oleic acid), and a terpene (parthenolide). We expect that this metabolite screening comparison of metal NPs applied via two different methods, in conjunction with the physical and chemical properties of the metal nanoparticles, might also be helpful in further understanding the NALDI-MS ionization mechanism.

Experimental

Materials

Metal NPs Au (99.95%, 15 nm), Ag (99.99%, 20 nm), and Cu (99.90%, 40 nm) were purchased from US Research Nanomaterials, Inc. (Houston, TX, USA). The metal sputtering targets gold (99.99% Au, Ø57mm x 0.1mm), silver (99.99% Ag, Ø57mm x 0.1mm) and copper (99.99% Cu, Ø57mm x 0.1mm) were purchased from Ted Pella, Inc. (Redding, CA, USA). The organic matrices 2,5-dihydroxybenzoic acid (98.0%), 1,5-diaminonaphthalene (97.0%) and 9-aminoacridine hydrochloride monohydrate (98.0%) were purchased from Sigma Aldrich (St. Louis, MO, USA). The metabolite standards malic acid, glucose, glucose 6-phosphate, sucrose, asparagine, glutamic acid,

isoleucine, coenzyme-A trilithum salt, biotin (vitamin-H), glycerol tripalmitate, vanillic acid (Fluka) and oleic acid (Fluka) were purchased from Sigma Aldrich (St. Louis, MO, USA). Ascorbic acid was purchased from Fisher Science Education (Nazareth, PA, USA). Phosphoenolpyruvic acid monopotassium salt was purchased from Alfa-Aesar (Ward Hill, MA, USA). Rac-Glycerol 1-phosphate disodium salt hexahydrate was purchased from Santa Cruz Biotechnology, Inc. (Dallas, TX, USA). Phosphocholine chloride sodium salt hydrate was purchased from Tokyo Chemical Industry Co. Ltd (Philadelphia, PA, USA). Parthenolide was purchased from TORIS Bioscience (Bristol, United Kingdom). Phospholipid mixture [L-α-Phosphatidylcholine, 20% (Soy) (Soy Total Lipid Extract)] was purchased from Avanti Polar Lipids, Inc. (Alabaster, AL, USA)

Sample Preparation for Plant Metabolite Standard Analysis

Nanoparticle Suspension and Plant Metabolite Standard Application

For analysis, metal nanoparticles were suspended at various concentrations in isopropanol to determine optimal NP concentration. Optimal concentrations are 5 to 10 mM for Au NPs, 2.5 to 5 for Ag NPs mM, and 20 mM for Cu NPs (Chapter 4). Each NP suspension was mixed with a standard solution containing either water-soluble standards (malic acid, vanillic acid, ascorbic acid, phosphoenolpyruvic acid, glycerol 3-phosphate, phosphocholine, glucose, sucrose, glucose 6-phosphate, glutamic acid, isoleucine, asparagine, vitamin H (biotin) and co-enzyme A) in water, or water-insoluble standards (glycerol tripalmitate, assorted phospholipids, oleic acid and parthenolide) in chloroform. The NP suspensions were mixed with standard solutions at a 10:1 volume ratio, yielding a 100 µM final concentration of standards. The metabolite standard and

NP suspension mixture was sprayed onto stainless steel MALDI target plates using a modified airbrush as an oscillating capillary nebulizer (OCN).

Complete details of the application are presented in Chapter 4, and a more detailed description of the OCN has been published previously.[121] Briefly, the NP-standard mixture was sprayed onto a stainless steel sample plate from a distance of 8-10 cm, with a nebulizing gas (N_2) pressure of 40 psi and a flow rate of 50 µL/min. A total of 500 µL of the NP-standard mixture was applied for each sample, providing uniform coverage of an area ~2 cm in diameter.

Metal Sputter Coating on Plant Metabolite Standard

For application of metals via physical vapor deposition, 45µL of 1.0 mM water-soluble standards in water or 45µL of 1.0 mM water-insoluble standards in chloroform were first sprayed by the OCN onto a glass slide. Metals were then applied using a Cressington 108 auto sputter coater instrument from Ted Pella, Inc. (Redding, CA, USA). As shown in the schematic diagram (Figure 1), the distance between the metal target and the sample was ~5 cm during sputtering. The chamber was flushed with argon gas twice before sputtering to remove oxygen. Sputtering current and argon pressure were set at 40 mA and at 0.04–0.05 mbar, respectively. Sputtering time was individually optimized for each type of nanoparticle. Various sputter coating times were studied for each metal. The time range for each particular metal was based on reported optimal sputtering times in the literature. Times tested were 5, 10, 15, 20 and 25 seconds for gold ; 5, 10, 20, 30, 40 and 50 seconds for silver; and 20, 30, 40, 50, 60, 70 and 80 seconds for copper. Absolute ion intensities for metabolite standards were

compared, and the optimal sputtering times were found to be 5-10 seconds for Au and 40-50 seconds for Cu. In the case of Ag NPs, optimal sputtering time was found to be different for water-soluble standards (5-10 seconds) and water-insoluble standards (50 seconds).

MS Data Acquisition and Analysis

A linear ion trap-orbitrap mass spectrometer with a MALDI ion source (MALDI LTQ-Orbitrap Discovery; Thermo Scientific, San Jose, CA, USA) was used for the current study. The instrument was modified to use an external, frequency-tripled, diode-pumped Nd:YAG laser operating at 355 nm and 60 Hz (UVFQ; Elforlight Ltd., Daventry, UK). Conditions such as laser energy and number of shots were individually optimized for each type of NP, and 250 spectra were collected in raster fashion with 100 µm step size. Three replicates were collected from two independent samples for each NP concentration (Chapter 4) and for each sputtering time. The laser spot size was estimated to be ~20 µm as determined from laser burn marks on a thin film of α-cyanohydroxycinnamic acid. Orbitrap scans were acquired over the *m/z* range of 50 to 1200. The signal was then averaged over the entire scan and samples were compared based upon their absolute intensities for ions of interest.

SEM Imaging

Au and Ag NPs were imaged by SEM using an FEI Quanta 250 in the Materials Analysis and Research Laboratory at Iowa State University. For SEM imaging of NPs applied by OCN, 500 µL of NP suspension (2.5 mM Ag or 10 mM Au) was sprayed onto

a silicon chip attached to a carbon stub. For SEM imaging of nanoparticles deposited by PVD, Ag was sputtered for 5s and 50s, while Au was sputtered for 10s. All application conditions (e.g. nebulizing pressure, flow rate, Ar pressure, and sputter current) were the same as described above.

Results and Discussion

Results

In positive mode, most metabolite standards were detected as alkali metal adducts, primarily $[M+Na]^+$ and $[M+K]^+$. Some compounds also showed appreciable lithium adduct signal, $[M+Li]^+$, likely due to the lithium present as a counter-ion in the co-enzyme A standard. In the case of Ag NPs, oleic acid and parthenolide were also detected as the $[M+Ag]^+$ species. For ion yield comparisons in positive mode, alkali adduct and protonated signals were summed. In negative-mode analyses, all metabolite standards were detected as $[M-H]^-$.

Absolute ion intensities for positive-mode screening of water-soluble and water-insoluble metabolite standards are presented in Table 1. The Au sputter coating produced high signal for LMW acids, amino acids, sugars, biotin (vitamin H) and TAGs in positive mode. The Au NP suspension did not produce high-intensity signal for any metabolites in positive mode. Ag suspension and sputter coating produced comparable signals. In contrast to results obtained for Au, Cu suspension produced high signals for LMW acids, sugars, amino acid and biotin (vitamin H) in positive mode (see Figure 3, Chapter 4) and Cu sputter coating did not produce high signal for any metabolite standard in positive mode. Figures 2 and 3 compare spectra between Au suspension

and sputter coating for water-soluble and water-insoluble metabolites in positive mode. The positive mode results for both Ag PVD and NPs suspension spray show silver adduct for oleic acid and parthenolide. Further studies will be conducted for analysis of wax ester standards to understand silver adduct formation at the unsaturation site of molecules.

Absolute ion intensities for negative-mode screening of water-soluble and water-insoluble metabolite standards are presented in Table 2. Both Ag suspension application and Ag sputter coating produced high signals for LMW acids, phosphate sugars and acids. Figure 4 and 5 present a comparison of spectra obtained from Ag suspension and sputter coating for water-soluble and water-insoluble metabolites in negative mode. From Table 2 it is clear that Au sputter coating produces high signal for LMW acids, relative to suspension spraying in negative mode also. Cu did not efficiently desorb/ionize plant metabolites in negative mode by either application method. The organic matrix DAN was found to be the most efficient matrix in ionizing LMW acids, phosphate compounds, sugars, amino acids, vitamin H (biotin), and co-enzyme-A.

Gold sputter coating is more effective in ionizing LMW plant metabolites vs. NP suspensions and other metal NPs because gold NPs aggregate and are difficult to keep in suspension, while sputter coating applies Au homogenously over samples. Figures 6 and 7 show a comparison of SEM images of sputter coated and OCN-sprayed nanoparticles on silicon chips. The SEM images shows that for both Au and Ag, sputter coating applied NPs in a homogeneous layer. This homogeneous application increases NP efficiency and minimizes sweet spot[2] formation in NALDI-MSI. Silver PVD and NPs are similarly effective in ionizing LMW water-soluble plant metabolites. Relative to all

other NPs, Ag suspension produces high intensity signals for phospholipids in negative mode. Interestingly, sputter coated silver does not produce high intensity signals for phospholipids. The reason for this unusual result is unknown and requires further investigation. Copper suspension outperforms sputter coated copper for all analytes, possibly due to copper oxide formation as a result of trace oxygen in the sputtering chamber.

Conclusion

We have compared solvent-free sputter coating and suspension spraying by OCN as methods of application of nanoparticle matrices for NALDI-MS. This study shows sputter coating is very effective for homogenous application of noble metal nanoparticles. This is preferable to spraying because metal NPs such as gold have a strong tendency to aggregate, settling out of suspension. This aggregation of Au NPs is a limiting factor for NALDI-MS efficiency as it complicates application and can lead to 'sweetspots' on the sample surface. It was also found that intermediate-pressure sputter coating is not suitable for transition metal NPs like Cu, as it can lead to oxidation of the metal surfaces.

Future efforts will extend this study to other noble metals such as platinum and transition metals like iron. It is expected that iron sputter coating under intermediate pressure will form iron oxide. We have previously found magnetite (Fe_3O_4) to be the most efficient of several tested nanoparticle matrices for analysis of both water-soluble and water-insoluble plant metabolite in positive mode (Chapter 4). The sputter coating

will be helpful for homogeneous application of iron and trace oxygen present in the sputtering chamber should oxidize the iron to iron oxide.

Overall, sputter coting is a very homogeneous application technique for noble metal NPs and transition metal oxide NPs. The future studies with various metals will be helpful developing novel sputtered metal matrices for NALDI-MS and –MSI.

Acknowledgements

We acknowledge Dr. Wu Yue in the Chemical & Biological Engineering Department at Iowa State University for allowing us access to the sputter coating instrument. This work was supported by the U.S. Department of Energy (DOE), Office of Basic Energy Sciences, Division of Chemical Sciences, Geosciences and Biosciences. The Ames Laboratory is operated by Iowa State University under DOE Contract DE-AC02-07CH11358.

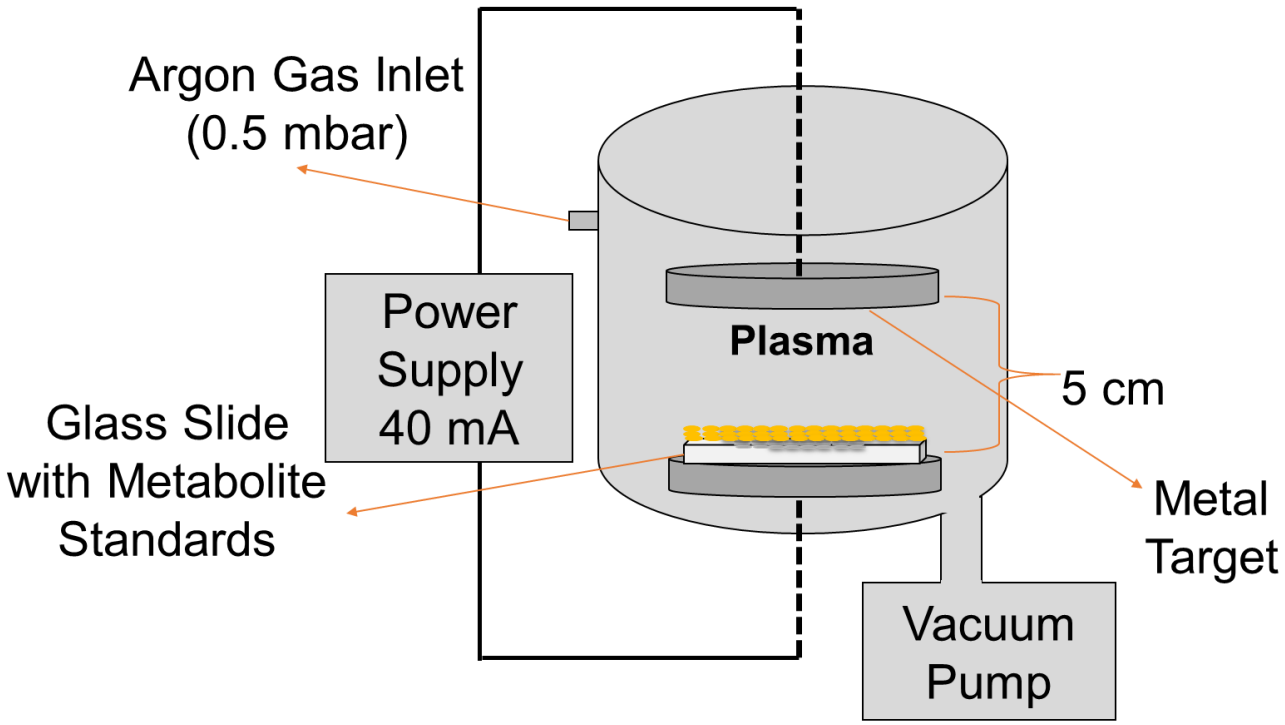

Figure 1: Schematic Diagram of 108auto sputter coater from Ted Pella, Inc.

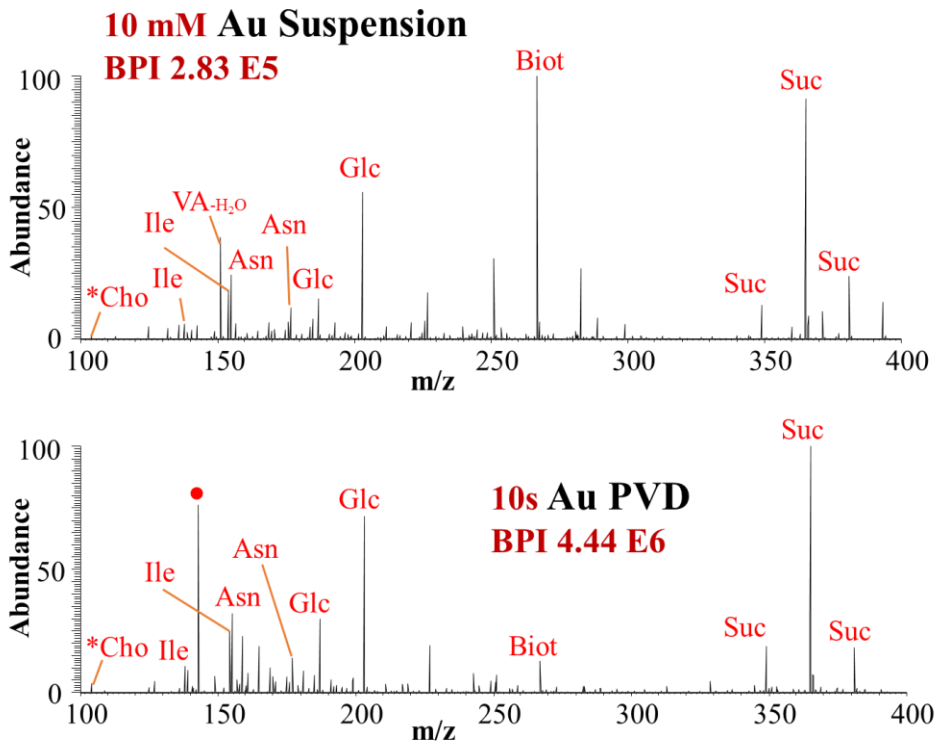

Figure 2: NALDI-MS spectra using gold NPs (Au Suspension) and gold sputter coating (Au PVD) as matrices to compare ionization efficiency for standard water-soluble metabolites in positive mode. Water-soluble metabolite ions are primarily detected as alkali metal adducts $[M+Na]^+$, $[M+K]^+$ and $[M+Li]^+$. Low-molecular weight acids, amino acids, vitamin H and coenzyme A fragments are also detected as di-alkali metal adducts. *Cho, VA, MA, AA, Ile, Asn, Glu, Glc, Suc and Biot represent choline fragment of phosphocholine, vanillic acid, malic acid, ascorbic acid, isoleucine, asparagine, glutamic acid, glucose, sucrose and biotin (vitamin-H), respectively. The phosphate fragments with alkali metal adducts were observed and are represented by ●. The contamination peak from DAN is represented by +. BPI denotes the base peak intensity.

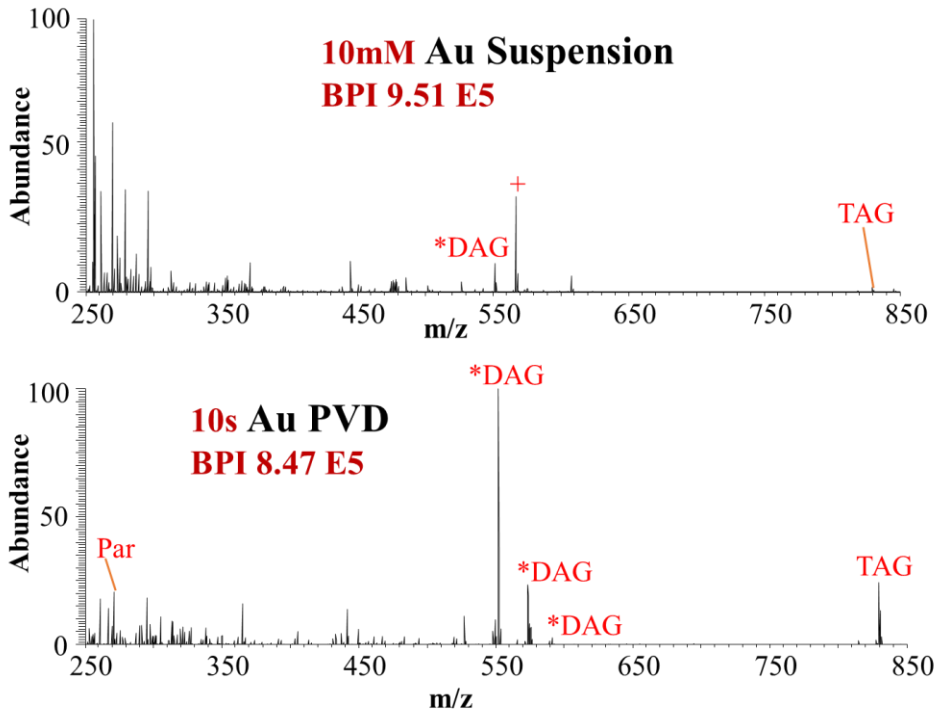

Figure 3: NALDI-MS spectra using gold NPs (Au Suspension) and gold sputter coating (Au PVD) as matrix to compare ionization efficiency for standard water-insoluble metabolites in positive mode. Water-insoluble metabolite ions are primarily detected as alkali metal adducts $[M+Na]^+$, and $[M+K]^+$. Par, *DAG and TAG represent parthenolide, diacylglycerol fragments and triacylglycerol, respectively. Contamination ions are represented with +. BPI denotes the base peak intensity.

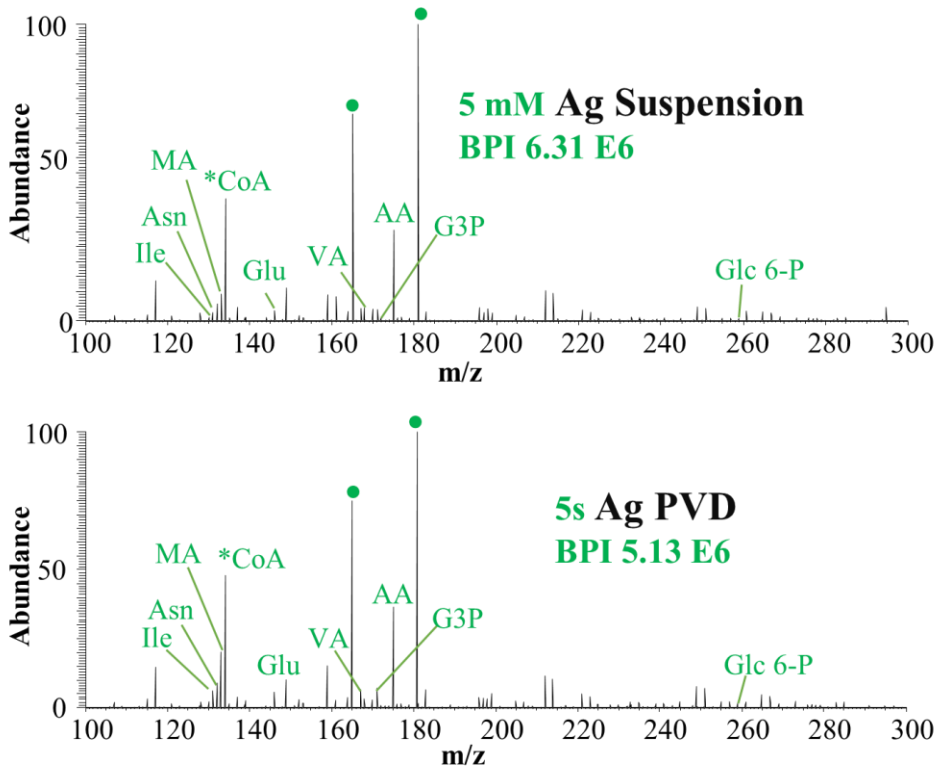

Figure 4: NALDI-MS spectra using silver NPs (Ag Suspension) and silver sputter coating (Ag PVD) as matrix to compare ionization efficiency for standard water-soluble metabolites in negative mode. All water-soluble metabolites ions are detected as $[M-H]^-$. *CoA, VA, MA, AA, Ile, Asn, Glu and G6P represent adenine fragment of co-enzyme A, vanillic acid, malic acid, ascorbic acid, isoleucine, asparagine, glutamic acid and glucose 6-phosphate, respectively. Phosphate fragments with alkali metal adducts were observed and are represented by ●. BPI denotes the base peak intensity.

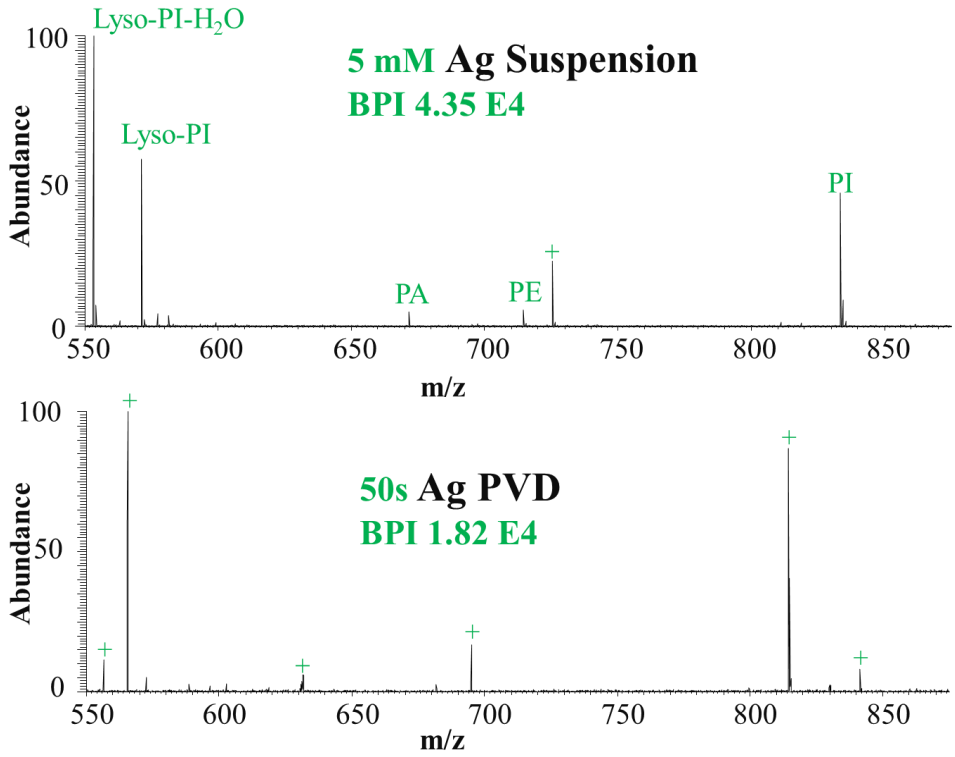

Figure 5: NALDI-MS spectra using silver NPs (Ag Suspension) and silver sputter coating (Ag PVD) as matrix to compare ionization efficiency for standard water-insoluble metabolites in negative mode. All water-insoluble metabolites ions are detected as [M-H]-. PA PE, PI and Lyso-PI represent phosphatidic acid, phosphatidylethanolamine, phosphatidylinositol and lyso-phosphatidylinositol, respectively. Contamination ions are represented with +. BPI denotes the base peak intensity.

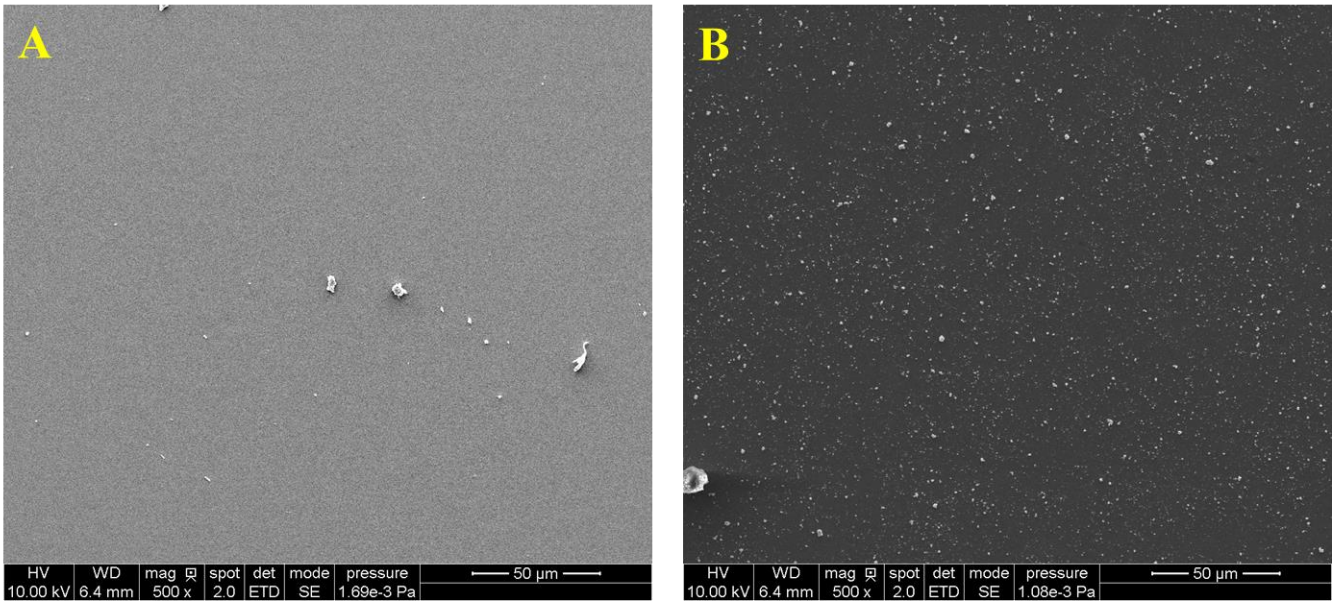

Figure 6: SEM images A and B are 50 seconds sputter coated Ag on silicon chip and 2.5 mM suspended Ag NPs 500 µL sprayed on silicon chip, respectively.

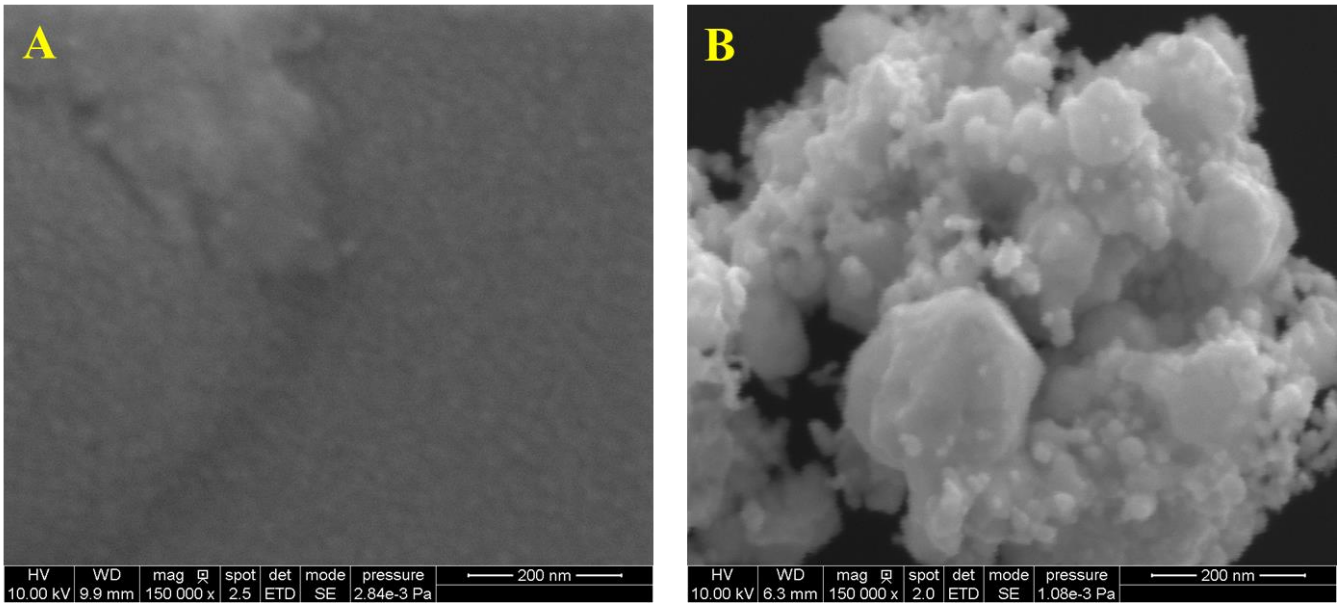

Figure 7: SEM images A and B are 10 seconds sputter coated Au on silicon chip and 10 mM suspended Au NPs 500 µL sprayed on silicon chip, respectively.

.

Table 1: Absolute ion signal intensity comparison of standard water-soluble and water-insoluble metabolites for NP screening in positive mode. Water-soluble metabolite ions are primarily detected as alkali metal adducts $[M+Na]^+$, $[M+K]^+$ and $[M+Li]^+$. Water-insoluble metabolite ions are detected mostly as alkali metal adducts $[M+Na]^+$ and $[M+K]^+$. Parthenolide and oleic acid are also detected as $[M+Ag]^+$ in silver NP spectra. Low-molecular weight acids, amino acids, vitamin H and Co-enzyme-A fragments are also detected as di-alkali metal adducts. This table represents the sum of all signals from different alkali metal adduct ions and includes the (typically weak) protonated ion species. Phosphocholine and choline fragments are detected as molecular ions. In water-insoluble metabolite standards, phosphocholine fragments and phosphatidylcholine are also detected as molecular ions and DAG fragments ions are detected as protonated species. PA represents phosphatidic acid and the metabolite fragments ions are represented with *.

Positive	**Water Soluble**																**Water Insoluble**							
	LMW Acid			**Phospho Metabolites**					**Sugars**		**Amino Acids**			**Co Enzyme**						**Lipids**				
Nanoparticles	**Malic Acid**	**Vanillic Acid**	**Ascorbic Acid**	**Phosphocholine**	***Choline**	**Phosphoenolpyruvic Acid**	**Glycerol 3-Phosphate**	**Glucose 6-Phospate**	**Glucose**	**Sucrose**	**Asparagine**	**Glutamic Acid**	**Iso-leucine**	***Co Enxyme-A (Adenine)**	***Co Enzyme-A**	**Vitamin H**	***Phosphocholine (PC)**	**Parthenolide**	**Oleic Acid**	***DAG**	**DAG**	**PA**	**PC**	**TAG**
Au Suspension	2E+04	1E+04	7E+03	6E+02	1E+04	2E+02	4E+04	1E+04	3E+05	6E+05	3E+05	4E+04	1E+05	4E+04	2E+04	5E+05	1E+05	1E+03	3E+02	1E+05	9E+01	4E+02	4E+02	3E+04
Ag Suspension	8E+04	3E+04	2E+04	1E+04	7E+04	6E+03	2E+05	6E+04	1E+06	9E+05	1E+06	1E+05	4E+05	7E+05	1E+05	1E+06	5E+04	1E+06	2E+05	5E+05	1E+02	4E+02	4E+02	7E+02
Cu Suspension	6E+04	6E+04	1E+04	2E+03	2E+05	1E+04	7E+04	4E+04	3E+06	6E+06	1E+06	1E+05	3E+05	8E+04	1E+05	3E+06	9E+04	4E+03	2E+02	2E+05	9E+01	4E+02	4E+02	9E+04
Au PVD	4E+05	7E+05	4E+05	2E+03	2E+05	1E+04	4E+05	1E+05	5E+06	6E+06	3E+06	6E+05	2E+06	2E+05	1E+05	1E+06	2E+04	2E+05	9E+04	1E+06	2E+04	4E+02	4E+02	2E+05
Ag PVD	2E+05	3E+04	4E+04	2E+03	2E+05	3E+04	4E+05	7E+04	2E+06	1E+06	2E+06	2E+05	4E+05	4E+05	1E+05	3E+05	4E+02	2E+05	8E+05	2E+05	1E+02	4E+02	3E+02	1E+03
Cu PVD	1E+04	1E+05	1E+03	9E+02	2E+05	6E+03	4E+04	8E+03	1E+06	1E+06	7E+05	4E+04	3E+05	3E+04	3E+03	2E+05	3E+02	2E+04	2E+03	2E+05	3E+02	5E+02	5E+02	6E+03
DHB	5E+03	5E+02	7E+03	6E+04	3E+06	3E+02	4E+04	1E+04	1E+05	3E+05	1E+05	8E+03	9E+03	1E+05	4E+04	3E+05	9E+05	2E+04	2E+02	3E+04	1E+02	2E+04	1E+04	5E+02
DAN	6E+02	6E+02	5E+02	1E+06	2E+06	2E+02	8E+02	5E+02	8E+03	3E+04	3E+03	2E+04	1E+03	3E+04	1E+05	4E+04	8E+05	7E+03	2E+02	6E+03	9E+01	5E+02	5E+02	3E+02

Table 2: Absolute ion signal intensity comparison of standard water-soluble and water-insoluble metabolites for NP screening in negative mode. All metabolite ions are detected as $[M-H]^-$. . PA PE, PG and PI represent phosphatidic acid, phosphatidylethanolamine, phosphatidylglycerol and phosphatidylinositol, respectively.

Negative	Water Soluble														Water Insoluble						
	LMW Acid			Phospho Metabolites				Amino Acids			Co Enzyme						Phospho Lipids				
Nanoparticles	Malic Acid	Vanillic Acid	Ascorbic Acid	Phosphoenolpyruvic Acid	Glycerol 3-Phosphate	Glucose 6-Phospate	Sucrose (Sugar)	Asparagine	Glutamic Acid	Iso-leucine	*Co Enxyme-A (Adenine)	*Co Enzyme-A	Co Enzyme-A	Biotin (Vitamin H)	Parthenolide (Terpene)	Oleic Acid (Fatty Acid)	Lyso- PI	PA	PE	PG	PI
Au Suspension	1E+05	2E+05	1E+05	1E+03	2E+04	8E+02	3E+02	4E+04	5E+04	1E+05	2E+05	9E+01	9E+01	5E+04	1E+02	2E+05	4E+03	5E+02	1E+03	1E+02	1E+03
Ag Suspension	1E+06	4E+05	2E+06	3E+05	4E+05	1E+05	2E+02	2E+05	3E+05	1E+05	5E+06	8E+01	1E+02	3E+04	3E+02	8E+05	9E+04	4E+03	1E+04	2E+02	4E+04
Cu Suspension	3E+04	5E+04	4E+04	1E+03	2E+03	4E+02	1E+02	1E+04	1E+04	4E+04	2E+05	1E+02	1E+02	2E+03	1E+02	1E+05	2E+03	6E+02	4E+02	1E+02	1E+04
Au PVD	8E+05	1E+05	1E+06	2E+05	3E+05	2E+05	4E+02	9E+04	2E+05	1E+04	9E+05	9E+01	1E+02	3E+03	7E+02	1E+06	2E+03	5E+02	4E+02	9E+01	5E+02
Ag PVD	4E+05	2E+05	1E+06	7E+04	2E+05	5E+04	8E+01	1E+05	2E+05	6E+04	3E+06	9E+01	9E+01	3E+03	1E+04	9E+06	1E+03	1E+03	5E+02	1E+02	8E+02
Cu PVD	1E+04	1E+05	4E+04	5E+03	4E+03	5E+02	1E+02	1E+04	5E+03	2E+04	4E+05	1E+02	1E+02	3E+02	1E+02	1E+06	7E+02	5E+02	4E+02	9E+01	4E+02
DHB	2E+04	2E+04	2E+04	6E+04	1E+04	1E+03	7E+02	1E+03	2E+03	1E+03	2E+05	4E+02	7E+02	2E+03	9E+01	7E+04	8E+04	4E+03	2E+03	1E+02	1E+05
DAN	3E+06	2E+06	2E+06	3E+05	5E+05	2E+05	1E+05	6E+05	1E+06	4E+05	2E+05	2E+04	2E+05	2E+05	3E+02	3E+05	1E+05	1E+04	9E+04	2E+03	1E+05

CHAPTER 6

SUMMARY AND FUTURE DIRECTION

Multiplex Imaging of LFP

In Chapter 2, we have successfully demonstrated the utility of multiplex MS imaging that combines high-resolution mass spectrometry with tandem mass spectrometry for chemical imaging of latent fingerprints (LFP). This technique is valuable when the available sample is limited, which is often the case with LFP. We could detect and image the chemical distributions of both endogenous and exogenous compounds. In this experiment we have chosen three compounds for MS/MS, but structural information for more compounds can be obtained by utilizing nine spiral steps to acquire more MS/MS images and/or one can also incorporate data-dependent scans to obtain MS/MS spectra of non-targeted compounds for identification in LFP for forensic and medical purposes.

In addition to molecular accurate mass information from high-mass resolution MS and structural information from MS/MS, we were also able to resolve partially overlapped fingerprints. Figure 1 shows an experiment where two partially overlapped LFP were deposited on a glass slide, one with tobacco snuff and one without. As shown in figure 1A, we were able detect exogenous compounds BDDA, DDA, and nicotine, in figure 1B, we were able to detect endogenous compounds cholesterol, palmitoleic acid, DAG and TAG, and in figure 1C, we were able to create combination images of DDA and nicotine, DAG and nicotine, and TAG and nicotine on LFP. In the future, different matrices can be used for MSI of a variety of endogenous and exogenous compounds.

Recently, gender-specific and individual-specific compounds have been detected in sweat[32]. In future experiments with different matrices (including nanoparticles) we can image a variety of chemically and forensically interesting compounds.

Fracturing and Imprinting Sample Preparation Methods

In Chapter 3, to study the chemical interfaces in plant-pest (rice-*Xoo*) interactions, we have adopted and developed novel sample preparation methods: imprinting and fracturing. These methods were developed with this particular application in mind, but imprinting is efficient for the analysis of a range of cytoplasmic hydrophilic compounds that can be "squeezed out" of the tissue under pressure. The advantage of this method is its applicability to almost any plant leaves, regardless of their size or surface roughness. The critical limitation, however, is that membrane-bound molecules or other hydrophobic compounds cannot be analyzed because they are not efficiently extracted. To analyze hydrophobic diterpenes produced against *Xoo* infection, we applied the fracturing method. This method is effective in exposing compounds underneath the leaf surface in plant tissue, including phospholipids and chlorophylls that cannot be analyzed with the imprinting technique. In rice leaf, we exposed the mesophyll layers surrounding the veins; therefore, this fracturing method can be applicable to study other plant pathogen interaction and/or other metabolites underneath the leaf surface. This can also be applied to fracture open other types of tissues, which are too thin to reliably cryosection.

The selection of matrices that can ionize the analyte of interest efficiently is the most critical factor in MS imaging. In this study, we demonstrated the use of Fe_3O_4 and

TiO_2 nanoparticles to efficiently ionize diterpene compounds that cannot be detected using traditional matrices. This application and effectiveness of nanoparticles as NALDI–MSI matrices to ionize specific classes of plant metabolites was the main motivation for development of nanoparticle matrices. The above results led us to perform a large-scale screening of various nanoparticles from different classes using a wide range of plant metabolites as standards, to further understand ionization mechanisms and provide empirical information for rational selection of matrices.

Nanoparticle Screening for NALDI-MS of Plant Metabolites

The use of nanoparticles as matrices instead of organic compounds is receiving increased interest because nanoparticles typically exhibit high laser absorptivity, low volatility, matrix homogeneity, and low background signals.[12],[90],[91] The developments in nanotechnology have made NPs of various sizes, shapes and compositions commercially available or easily synthesized.[12]. In addition to that, we have successfully developed and demonstrated the use of Fe_3O_4 and TiO_2 NPs to efficiently ionize diterpenoid phytoalexin compounds that cannot otherwise be analyzed (Chapter 3). This study was the main motivation behind the empirical nanoparticle screening for desorption/ionization of low molecular weight compounds. We employed thirteen NPs of three common classes (metal, metal oxide semiconductors and carbon-based), and compared them with three common organic matrices (DAN, DHB and 9-AA) for nanoparticle/matrix-assisted laser desorption/ionization-mass spectrometry for the detection of low molecular weight metabolites. Plant metabolites used for NP screening include: small organic acids and sugars (including phospho metabolites), amino acids, a

vitamin, a co-enzyme and various lipids. In addition to this empirical screening of nanoparticles, we calculated desorption temperatures for NPs using physical properties and corrected the existing thermal model.

The screening results of NPs showed that Fe_3O_4, BDND, TiO_2 and graphene oxide NPs are the most efficient for desorption/ionization of plant metabolites. The extensive fragmentation of metabolites with WO_3 NPs and desorption/ionization efficiency of Fe_3O_4 and TiO_2 were supported by this revised thermal model. In negative mode, BDND, graphene oxide and silver NPs were effective for selected classes of metabolites. Future work will be focused on theoretical calculations for comparison of carbon-based NPs and understanding the thermal desorption mechanism employing the corrected model. The revised thermal model presented here provides a more accurate calculation of the desorption temperature range, enabling rational selection of NP matrices for the thermally-driven NALDI process. We expect that this empirical study, along with the theoretical calculations, will be very helpful for future selection/prediction of particular nanoparticle matrices for ionization of low-molecular weight compounds.

Suspension vs. Physical Vapor Deposition

This work was an extension of the nanoparticle screening study in Chapter 4. Here, we compared two metal nanoparticle application techniques for nanoparticle-assisted laser desorption/ionization-mass spectrometry to detect low-molecular weight plant metabolites – solvent-free sputter coating (physical vapor deposition) and spraying using an oscillating capillary nebulizer. One critical observation from Chapter 4 was that gold and platinum nanoparticles were difficult to keep suspended and they settled down

to the bottom of the syringe. The strong tendency of gold NPs to aggregate was confirmed by SEM imaging of the sprayed gold suspension. This significantly limits the efficiency of these NPs to desorb/ionize plant metabolites. The SEM imaging results confirmed that solvent-free argon sputter is an effective and homogeneous method for NP application and the screening results show gold NPs are the most efficient matrix among metal NPs. It was also found that intermediate-pressure sputter coating oxidized some metals such as copper, and reduced their efficacy as matrices. Future efforts will extend this study to other noble and transition metals. The theoretical calculation for Chapter 4 indicated that platinum nanoparticles have the potential to be an effective matrix if they can be applied homogeneously. The finding from Chapter 4 also shows magnetite (Fe_3O_4) to be the most efficient of several tested NPs matrices for analysis of both water-soluble and water-insoluble plant metabolite in positive mode. Therefore, we propose to use sputter coating for homogeneous application of iron with trace oxygen present in the sputtering chamber. It is hoped that this will create a homogenous layer of iron oxide on the sample surface. This homogeneous application of efficient matrix will be helpful developing novel sputtered metal and metal oxide matrices for NALDI-MS imaging.

The results of Chapter 4 and 5 will be helpful to develop novel matrices and adopt homogeneous application methods for MALDI/NALDI-MS imaging of low-molecular weight plant metabolites which are difficult to desorb/ionize otherwise. These developments will be helpful to study a wide variety of plant tissues to solve important biological questions.

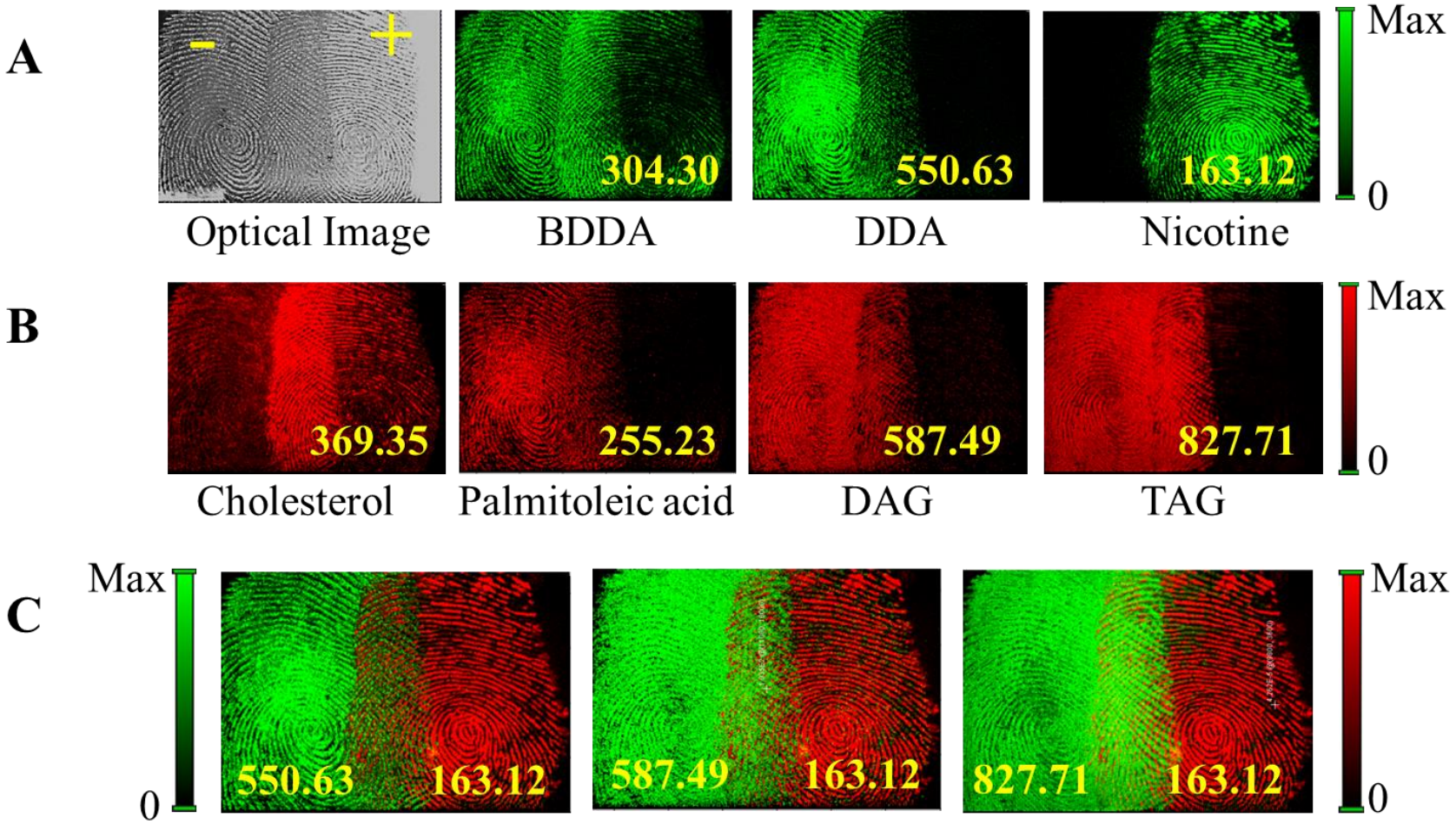

Figure 1: Partially Overlapped LFP With and Without Tobacco Snuff

REFERENCES

[1] J. H. Jungmann, R. M. Heeren,Emerging technologies in mass spectrometry imaging *Journal of proteomics* **2012**, *75*, 5077.

[2] A. Svatoš,Mass spectrometric imaging of small molecules *Trends in biotechnology* **2010**, *28*, 425.

[3] N. Zaima, T. Hayasaka, N. Goto-Inoue, M. Setou,Matrix-assisted laser desorption/ionization imaging mass spectrometry *International journal of molecular sciences* **2010**, *11*, 5040.

[4] Y. J. Lee, D. C. Perdian, Z. Song, E. S. Yeung, B. J. Nikolau,Use of mass spectrometry for imaging metabolites in plants *The Plant Journal* **2012**, *70*, 81.

[5] P. M. Angel, R. M. Caprioli,Matrix-assisted laser desorption ionization imaging mass spectrometry: in situ molecular mapping *Biochemistry* **2013**, *52*, 3818.

[6] A. T. Klein, G. B. Yagnik, J. D. Hohenstein, Z. Ji, J. Zi, M. D. Reichert, G. C. MacIntosh, B. Yang, R. J. Peters, J. Vela,Investigation of the Chemical Interface in the Soybean-Aphid and Rice-Bacteria Interactions Using MALDI-Mass Spectrometry Imaging *Analytical chemistry* **2015**.

[7] G. B. Yagnik, A. R. Korte, Y. J. Lee,Multiplex mass spectrometry imaging for latent fingerprints *Journal of Mass Spectrometry* **2013**, *48*, 100.

[8] K. Hanhineva, I. Rogachev, H. Kokko, S. Mintz-Oron, I. Venger, S. Kärenlampi, A. Aharoni,Non-targeted analysis of spatial metabolite composition in strawberry (Fragaria× ananassa) flowers *Phytochemistry* **2008**, *69*, 2463.

[9] I. Ahuja, R. Kissen, A. M. Bones,Phytoalexins in defense against pathogens *Trends in Plant Science* **2012**, *17*, 73.

[10] T. Toyomasu,Recent advances regarding diterpene cyclase genes in higher plants and fungi *Bioscience, biotechnology, and biochemistry* **2008**, *72*, 1168.

[11] D. Cartwright, P. Langcake, R. Pryce, D. Leworthy,Chemical activation of host defence mechanisms as a basis for crop protection *Nature* **1977**, *267*, 511.

[12] C.-K. Chiang, W.-T. Chen, H.-T. Chang,Nanoparticle-based mass spectrometry for the analysis of biomolecules *Chemical Society Reviews* **2011**, *40*, 1269.

[13] M. Schürenberg, K. Dreisewerd, F. Hillenkamp,Laser desorption/ionization mass spectrometry of peptides and proteins with particle suspension matrixes *Analytical Chemistry* **1999**, *71*, 221.

[14] T. Yonezawa, H. Kawasaki, A. Tarui, T. Watanabe, R. Arakawa, T. Shimada, F. Mafune,Detailed investigation on the possibility of nanoparticles of various metal elements for surface-assisted laser desorption/ionization mass spectrometry *Analytical Sciences* **2009**, *25*, 339.

[15] K. Tanaka, H. Waki, Y. Ido, S. Akita, Y. Yoshida, T. Yoshida, T. Matsuo,Protein and polymer analyses up to m/z 100 000 by laser ionization time? of? flight mass spectrometry *Rapid communications in mass spectrometry* **1988**, *2*, 151.

[16] H.-W. Tang, K.-M. Ng, W. Lu, C.-M. Che,Ion desorption efficiency and internal energy transfer in carbon-based surface-assisted laser desorption/ionization mass spectrometry: Desorption mechanism (s) and the design of SALDI substrates *Analytical chemistry* **2009**, *81*, 4720.

[17] R. Wolstenholme, R. Bradshaw, M. R. Clench, S. Francese,Study of latent fingermarks by matrix-assisted laser desorption/ionisation mass spectrometry imaging of endogenous lipids *Rapid communications in mass spectrometry* **2009**, *23*, 3031.

[18] S. Yang, C. F. Wang, S. Chen,A Release-Induced Response for the Rapid Recognition of Latent Fingerprints and Formation of Inkjet-Printed Patterns *Angewandte Chemie* **2011**, *123*, 3790.

[19] H. Faulds,On the skin-furrows of the hand *Nature* **1880**, *22*, 605.

[20] AuAdvances in fingerprint technologythor, *Advances in fingerprint technology*, CRC press, **2001**.

[21] M. Zhang, H. H. Girault,SECM for imaging and detection of latent fingerprints *Analyst* **2009**, *134*, 25.

[22] R. Leggett, E. E. Lee-Smith, S. M. Jickells, D. A. Russell,“Intelligent” Fingerprinting: Simultaneous Identification of Drug Metabolites and Individuals by Using Antibody-Functionalized Nanoparticles *Angewandte Chemie* **2007**, *119*, 4178.

[23] A. Y. Lim, J. Seviour,Doped silica nanoparticles for the detection of pharmaceutical terbinafine in latent fingerprints by mass spectrometry *Analytical Methods* **2012**, *4*, 1983.

[24] L. Ferguson, R. Bradshaw, R. Wolstenholme, M. Clench, S. Francese,Two-step matrix application for the enhancement and imaging of latent fingermarks *Analytical chemistry* **2011**, *83*, 5585.

[25] M. Tahtouh, S. A. Scott, J. R. Kalman, B. J. Reedy,Four novel alkyl 2-cyanoacylate monomers and their use in latent fingermark detection by mid-infrared spectral imaging *Forensic science international* **2011**, *207*, 223.

[26] R. M. Connatser, S. M. Prokes, O. J. Glembocki, R. L. Schuler, C. W. Gardner, S. A. Lewis, L. A. Lewis,Toward Surface-Enhanced Raman Imaging of Latent Fingerprints* *Journal of forensic sciences* **2010**, *55*, 1462.

[27] R. S. Croxton, M. G. Baron, D. Butler, T. Kent, V. G. Sears,Development of a GC-MS Method for the Simultaneous Analysis of Latent Fingerprint Components* *Journal of forensic sciences* **2006**, *51*, 1329.

[28] Advanced fingerprint analysis project fingerprint constituentsG. M. Mong, C. Petersen, T. Clauss, Pacific Northwest National Lab., Richland, WA (US), **1999**.

[29] H.-W. Tang, W. Lu, C.-M. Che, K.-M. Ng,Gold nanoparticles and imaging mass spectrometry: Double imaging of latent fingerprints *Analytical chemistry* **2010**, *82*, 1589.

[30] D. R. Ifa, J. M. Wiseman, Q. Song, R. G. Cooks,Development of capabilities for imaging mass spectrometry under ambient conditions with desorption electrospray ionization (DESI) *International Journal of Mass Spectrometry* **2007**, *259*, 8.

[31] M. Szynkowska, K. Czerski, J. Grams, T. Paryjczak, A. Parczewski,Preliminary studies using imaging mass spectrometry TOF-SIMS in detection and analysis of fingerprints *The Imaging Science Journal* **2007**, *55*, 180.

[32] D. J. Penn, E. Oberzaucher, K. Grammer, G. Fischer, H. A. Soini, D. Wiesler, M. V. Novotny, S. J. Dixon, Y. Xu, R. G. Brereton,Individual and gender fingerprints in human body odour *Journal of The Royal Society Interface* **2007**, *4*, 331.

[33] L. S. Ferguson, F. Wulfert, R. Wolstenholme, J. M. Fonville, M. R. Clench, V. A. Carolan, S. Francese,Direct detection of peptides and small proteins in fingermarks and determination of sex by MALDI mass spectrometry profiling *Analyst* **2012**, *137*, 4686.

[34] D. C. Perdian, Y. J. Lee,Imaging MS Methodology for More Chemical Information in Less Data Acquisition Time Utilizing a Hybrid Linear Ion Trap−Orbitrap Mass Spectrometer *Analytical Chemistry* **2010**, *82*, 9393.

[35] J. A. Hankin, R. M. Barkley, R. C. Murphy,Sublimation as a method of matrix application for mass spectrometric imaging *Journal of The American Society for Mass Spectrometry* **2007**, *18*, 1646.

[36] J. Gidden, R. Liyanage, B. Durham, J. O. Lay,Reducing fragmentation observed in the matrix-assisted laser desorption/ionization time-of-flight mass spectrometric analysis of triacylglycerols in vegetable oils *Rapid communications in mass spectrometry* **2007**, *21*, 1951.

[37] L. Sun, S.-Q. Zhang, D.-F. Zhong,In vitro identification of metabolites of verapamil in rat liver microsomes *Acta Pharmacol Sin* **2004**, *25*, 121.

[38] N. C. d. C. Borges, G. D. Mendes, R. E. Barrientos-Astigarraga, P. Galvinas, C. H. Oliveira, G. De Nucci,Verapamil quantification in human plasma by liquid chromatography coupled to tandem mass spectrometry: an application for bioequivalence study *Journal of Chromatography B* **2005**, *827*, 165.

[39] W. Byrdwell, W. E. Neff,Dual parallel electrospray ionization and atmospheric pressure chemical ionization mass spectrometry (MS), MS/MS and MS/MS/MS for the analysis of triacylglycerols and triacylglycerol oxidation products *Rapid communications in mass spectrometry* **2002**, *16*, 300.

[40] J. A. Hankin, S. E. Farias, R. M. Barkley, K. Heidenreich, L. C. Frey, K. Hamazaki, H.-Y. Kim, R. C. Murphy,MALDI mass spectrometric imaging of lipids in rat brain injury models *Journal of the American Society for Mass Spectrometry* **2011**, *22*, 1014.

[41] S. A. Hogenhout, J. I. B. Bos,Effector proteins that modulate plant–insect interactions *Current Opinion in Plant Biology* **2011**, *14*, 422.

[42] P. N. Dodds, J. P. Rathjen,Plant immunity: towards an integrated view of plant–pathogen interactions *Nat Rev Genet* **2010**, *11*, 539.

[43] J. D. G. Jones, J. L. Dangl,The plant immune system *Nature* **2006**, *444*, 323.

[44] J. Bohlmann, G. Meyer-Gauen, R. Croteau,Plant terpenoid synthases: Molecular biology and phylogenetic analysis *Proc. Natl. Acad. Sci. USA* **1998**, *95*, 4126.

[45] T. Sana, S. Fischer, G. Wohlgemuth, A. Katrekar, K.-h. Jung, P. Ronald, O. Fiehn,Metabolomic and transcriptomic analysis of the rice response to the bacterial blight pathogen Xanthomonas oryzae pv. oryzae *Metabolomics* **2010**, *6*, 451.

[46] W. E. Riedell, E. A. Beckendorf, M. A. Catangui,Soybean Aphid Injury Effects on Shoot Nitrogen Components in Glycine max *Crop Sci.* **2013**, 232.

[47] D. Sato, M. Sugimoto, H. Akashi, M. Tomita, T. Soga,Comparative metabolite profiling of foxglove aphids (Aulacorthum solani Kaltenbach) on leaves of resistant and susceptible soybean strains *Molecular BioSystems* **2014**, *10*, 909.

[48] M. E. Studham, G. C. MacIntosh,Multiple Phytohormone Signals Control the Transcriptional Response to Soybean Aphid Infestation in Susceptible and Resistant Soybean Plants *Molecular Plant-Microbe Interactions* **2012**, *26*, 116.

[49] M. Schad, R. Mungur, O. Fiehn, J. Kehr,Metabolic profiling of laser microdissected vascular bundles of Arabidopsis thaliana *Plant methods* **2005**, *1*, 2.

[50] J. Fang, B. Schneider,Laser Microdissection: a Sample Preparation Technique for Plant Micrometabolic Profiling *Phytochemical Analysis* **2013**.

[51] D. Eikel, M. Vavrek, S. Smith, C. Bason, S. Yeh, W. A. Korfmacher, J. D. Henion,Liquid extraction surface analysis mass spectrometry (LESA-MS) as a novel profiling tool for drug distribution and metabolism analysis: the terfenadine example *Rapid Communications in Mass Spectrometry* **2011**, *25*, 3587.

[52] J. G. Swales, J. W. Tucker, N. Strittmatter, A. Nilsson, D. Cobice, M. R. Clench, C. L. Mackay, P. E. Andren, Z. Takats, P. J. H. Webborn, R. J. A. Goodwin,Mass Spectrometry Imaging of Cassette-Dosed Drugs for Higher Throughput Pharmacokinetic and Biodistribution Analysis *Analytical Chemistry* **2014**, *86*, 8473.

[53] I. Sparkes, F. Brandizzi,Fluorescent protein-based technologies: shedding new light on the plant endomembrane system *The Plant Journal* **2012**, *70*, 96.

[54] R. M. Caprioli, T. B. Farmer, J. Gile,Molecular imaging of biological samples: Localization of peptides and proteins using MALDI-TOF MS *Analytical Chemistry* **1997**, *69*, 4751.

[55] H. Wei, K. Nolkrantz, D. H. Powell, J. H. Woods, M. C. Ko, R. T. Kennedy,Electrospray sample deposition for matrix-assisted laser desorption/ionization (MALDI) and atmospheric pressure MALDI mass spectrometry with attomole detection limits *Rapid Communications in Mass Spectrometry* **2004**, *18*, 1193.

[56] Y. J. Lee, D. C. Perdian, Z. Song, E. S. Yeung, B. J. Nikolau,Use of mass spectrometry for imaging metabolites in plants *Plant Journal* **2012**, *70*, 81.

[57] N. Bjarnholt, B. Li, J. D'Alvise, C. Janfelt,Mass spectrometry imaging of plant metabolites - principles and possibilities *Natural Product Reports* **2014**, *31*, 818.

[58] P. J. Horn, K. D. Chapman,Lipidomics in situ: Insights into plant lipid metabolism from high resolution spatial maps of metabolites *Progress in Lipid Research* **2014**, *54*, 32.

[59] J. H. Jun, Z. Song, Z. Liu, B. J. Nikolau, E. S. Yeung, Y. J. Lee,High-spatial and high-mass resolution imaging of surface metabolites of Arabidopsis thaliana by laser desorption-ionization mass spectrometry using colloidal silver *Analytical Chemistry* **2010**, *82*, 3255.

[60] P. J. Horn, A. R. Korte, P. B. Neogi, E. Love, J. Fuchs, K. Strupat, L. Borisjuk, V. Shulaev, Y.-J. Lee, K. D. Chapman,Spatial Mapping of Lipids at Cellular Resolution in Embryos of Cotton *The Plant Cell* **2012**, *24*, 622.

[61] A. R. Korte, Z. Song, B. J. Nikolau, Y. J. Lee,Mass spectrometric imaging as a high-spatial resolution tool for functional genomics: Tissue-specific gene

expression of TT7 inferred from heterogeneous distribution of metabolites in Arabidopsis flowers *Analytical Methods* **2012**, *4*, 474.

[62] J. Thunig, S. H. Hansen, C. Janfelt,Analysis of Secondary Plant Metabolites by Indirect Desorption Electrospray Ionization Imaging Mass Spectrometry *Analytical Chemistry* **2011**, *83*, 3256.

[63] E. Cabral, D. Ifa, in *BDESI Imaging of Small Molecules in Biological Tissuesook DESI Imaging of Small Molecules in Biological Tissues, Vol. 1203* (Ed.: L. He), Springer New York, **2015**, pp. 63.

[64] D. I. Campbell, C. R. Ferreira, L. S. Eberlin, R. G. Cooks,Improved spatial resolution in the imaging of biological tissue using desorption electrospray ionization *Analytical and Bioanalytical Chemistry* **2012**, *404*, 389.

[65] V. Kertesz, G. J. Van Berkel,Improved imaging resolution in desorption electrospray ionization mass spectrometry *Rapid Communications in Mass Spectrometry* **2008**, *22*, 2639.

[66] P. J. Roach, J. Laskin, A. Laskin,Nanospray desorption electrospray ionization: an ambient method for liquid-extraction surface sampling in mass spectrometry *Analyst* **2010**, *135*, 2233.

[67] C. Li, Z. Wang, A. D. Jones,Chemical imaging of trichome specialized metabolites using contact printing and laser desorption/ionization mass spectrometry *Analytical and Bioanalytical Chemistry* **2014**, *406*, 171.

[68] R. Shroff, F. Vergara, A. Muck, A. Svatoš, J. Gershenzon,Nonuniform distribution of glucosinolates in Arabidopsis thaliana leaves has important consequences for plant defense *Proceedings of the National Academy of Sciences* **2008**, *105*, 6196.

[69] R. Shroff, K. Schramm, V. Jeschke, P. Nemes, A. Vertes, J. Gershenzon, A. Svatoš,Quantification of plant surface metabolites by MALDI mass spectrometry imaging: glucosinolates on Arabidopsis thaliana leaves *The Plant Journal* **2015**.

[70] G. Hamm, V. Carré, A. Poutaraud, B. Maunit, G. Frache, D. Merdinoglu, J.-F. Muller,Determination and imaging of metabolites from Vitis vinifera leaves by laser desorption/ionisation time-of-flight mass spectrometry *Rapid Communications in Mass Spectrometry* **2010**, *24*, 335.

[71] Y. Li, J. Zou, M. Li, D. D. Bilgin, L. O. Vodkin, G. L. Hartman, S. J. Clough,Soybean defense responses to the soybean aphid *New Phytologist* **2008**, *179*, 185.

[72] M. V. Chiozza, M. E. O'Neal, G. C. MacIntosh,Constitutive and Induced Differential Accumulation of Amino Acid in Leaves of Susceptible and Resistant Soybean Plants in Response to the Soybean Aphid (Hemiptera: Aphididae) *Environmental Entomology* **2010**, *39*, 856.

[73] J. Diaz-montano, J. C. Reese, W. T. Schapaugh, L. R. Campbell,Chlorophyll Loss Caused by Soybean Aphid (Hemiptera: Aphididae) Feeding on Soybean *Journal of Economic Entomology* **2007**, *100*, 1657.

[74] A. Evidente, V. Venturi, M. Masi, G. Degrassi, A. Cimmino, L. Maddau, A. Andolfi,In Vitro Antibacterial Activity of Sphaeropsidins and Chemical Derivatives toward Xanthomonas oryzae pv. oryzae, the Causal Agent of Rice Bacterial Blight *Journal of Natural Products* **2011**, *74*, 2520.

[75] E. A. Schmelz, A. Huffaker, J. W. Sims, S. A. Christensen, X. Lu, K. Okada, R. J. Peters,Biosynthesis, elicitation and roles of monocot terpenoid phytoalexins *Plant J* **2014**, *79*, 659.

[76] T. Akatsuka, O. Kodama, H. Sekido, Y. Kono, S. Takeuchi,Novel phytoalexins (oryzalexins A, B, and C) isolated from rice blast leaves infected with *Pyricularia oryzae*. Part I: Isolation, characterization and biological activities of oryzalexins *Agric. Biol. Chem.* **1985**, *49*, 1689.

[77] S. Taira, Y. Sugiura, S. Moritake, S. Shimma, Y. Ichiyanagi, M. Setou,Nanoparticle-assisted laser desorption/ionization based mass imaging with cellular resolution *Analytical Chemistry* **2008**, *80*, 4761.

[78] K. Shrivas, T. Hayasaka, Y. Sugiura, M. Setou,Method for Simultaneous Imaging of Endogenous Low Molecular Weight Metabolites in Mouse Brain Using TiO2 Nanoparticles in Nanoparticle-Assisted Laser Desorption/Ionization-Imaging Mass Spectrometry *Analytical Chemistry* **2011**, *83*, 7283.

[79] J. Bai, S.-H. Choi, G. Ponciano, H. Leung, J. E. Leach,Xanthomonas oryzae pv. Oryzae Avirulence Genes Contribute Differently and Specifically to Pathogen Aggressiveness *Molecular Plant-Microbe Interactions* **2000**, *13*, 1322.

[80] D. Tian, J. Wang, X. Zeng, K. Gu, C. Qiu, X. Yang, Z. Zhou, M. Goh, Y. Luo, M. Murata-Hori, F. F. White, Z. Yin,The Rice TAL Effector–Dependent Resistance Protein XA10 Triggers Cell Death and Calcium Depletion in the Endoplasmic Reticulum *The Plant Cell* **2014**.

[81] P. Berger, N. B. Adelman, K. J. Beckman, D. J. Campbell, A. B. Ellis, G. C. Lisensky,Preparation and Properties of an Aqueous Ferrofluid *Journal of Chemical Education* **1999**, *76*, 943.

[82] J. Wei, H. Li, M. P. Barrow, P. B. O'Connor,Structural characterization of chlorophyll-a by high resolution tandem mass spectrometry *Journal of The American Society for Mass Spectrometry* **2013**, *24*, 753.

[83] AuInorganic nanoparticles: synthesis, applications, and perspectivesthor, *Inorganic nanoparticles: synthesis, applications, and perspectives*, CRC Press, **2010**.

[84] C. R. Martin, D. T. Mitchell,Peer reviewed: nanomaterials in analytical chemistry *Analytical chemistry* **1998**, *70*, 322A.

[85] AuMetal nanoparticles for catalysis: advances and applicationsthor, *Metal nanoparticles for catalysis: advances and applications, Vol. 17*, Royal society of chemistry, **2014**.

[86] F. P. Zamborini, L. Bao, R. Dasari,Nanoparticles in measurement science *Analytical chemistry* **2011**, *84*, 541.

[87] M. J. Ruedas-Rama, J. D. Walters, A. Orte, E. A. Hall,Fluorescent nanoparticles for intracellular sensing: a review *Analytica chimica acta* **2012**, *751*, 1.

[88] D. Wan, M. Gao, Y. Wang, P. Zhang, X. Zhang,A rapid and simple separation and direct detection of glutathione by gold nanoparticles and graphene-based MALDI–TOF-MS *Journal of separation science* **2013**, *36*, 629.

[89] S. Taira, D. Kaneko, Y. Kawamura-Konishi, Y. Ichiyanagi,Application of Functionalized Nanoparticle for Mass Spectrometry *Journal of nanoscience and nanotechnology* **2014**, *14*, 3155.

[90] Y.-F. Huang, H.-T. Chang,Nile red-adsorbed gold nanoparticle matrixes for determining aminothiols through surface-assisted laser desorption/ionization mass spectrometry *Analytical chemistry* **2006**, *78*, 1485.

[91] N. C. Chiang, C. K. Chiang, Z. H. Lin, T. C. Chiu, H. T. Chang,Detection of aminothiols through surface-assisted laser desorption/ionization mass spectrometry using mixed gold nanoparticles *Rapid Communications in Mass Spectrometry* **2009**, *23*, 3063.

[92] C.-K. Chiang, N.-C. Chiang, Z.-H. Lin, G.-Y. Lan, Y.-W. Lin, H.-T. Chang,Nanomaterial-based surface-assisted laser desorption/ionization mass spectrometry of peptides and proteins *Journal of the American Society for Mass Spectrometry* **2010**, *21*, 1204.

[93] H. Kawasaki, T. Yonezawa, T. Watanabe, R. Arakawa,Platinum nanoflowers for surface-assisted laser desorption/ionization mass spectrometry of biomolecules *The Journal of Physical Chemistry C* **2007**, *111*, 16278.

[94] J. Tang, Y. Liu, D. Qi, G. Yao, C. Deng, X. Zhang,On-plate-selective enrichment of glycopeptides using boronic acid-modified gold nanoparticles for direct MALDI-QIT-TOF MS analysis *Proteomics* **2009**, *9*, 5046.

[95] Y.-F. Huang, H.-T. Chang,Analysis of adenosine triphosphate and glutathione through gold nanoparticles assisted laser desorption/ionization mass spectrometry *Analytical chemistry* **2007**, *79*, 4852.

[96] J. A. McLean, K. A. Stumpo, D. H. Russell,Size-selected (2-10 nm) gold nanoparticles for matrix assisted laser desorption ionization of peptides *Journal of the American Chemical Society* **2005**, *127*, 5304.

[97] W.-T. Chen, C.-K. Chiang, Y.-W. Lin, H.-T. Chang,Quantification of captopril in urine through surface-assisted laser desorption/ionization mass spectrometry using 4-mercaptobenzoic acid-capped gold nanoparticles as an internal standard *Journal of the American Society for Mass Spectrometry* **2010**, *21*, 864.

[98] C.-L. Su, W.-L. Tseng,Gold nanoparticles as assisted matrix for determining neutral small carbohydrates through laser desorption/ionization time-of-flight mass spectrometry *Analytical chemistry* **2007**, *79*, 1626.

[99] Y. W. Lin, W. T. Chen, H. T. Chang,Exploring the interactions between gold nanoparticles and analytes through surface-assisted laser desorption/ionization mass spectrometry *Rapid Communications in Mass Spectrometry* **2010**, *24*, 933.

[100] J. R. Lee, J. Lee, S. K. Kim, K. P. Kim, H. S. Park, W. S. Yeo,Mass Spectrometry Signal Amplification Method for Attomolar Detection of Antigens Using Small-Molecule-Tagged Gold Microparticles *Angewandte Chemie International Edition* **2008**, *47*, 9518.

[101] T.-C. Chiu, L.-C. Chang, C.-K. Chiang, H.-T. Chang,Determining estrogens using surface-assisted laser desorption/ionization mass spectrometry with silver nanoparticles as the matrix *Journal of the American Society for Mass Spectrometry* **2008**, *19*, 1343.

[102] S. Cha, Z. Song, B. J. Nikolau, E. S. Yeung,Direct profiling and imaging of epicuticular waxes on Arabidopsis thaliana by laser desorption/ionization mass spectrometry using silver colloid as a matrix *Analytical chemistry* **2009**, *81*, 2991.

[103] T. Hayasaka, N. Goto-Inoue, N. Zaima, K. Shrivas, Y. Kashiwagi, M. Yamamoto, M. Nakamoto, M. Setou,Imaging mass spectrometry with silver nanoparticles reveals the distribution of fatty acids in mouse retinal sections *Journal of the American Society for Mass Spectrometry* **2010**, *21*, 1446.

[104] The use of nanomaterials for mass spectrometry can be uplifting for analyte detectionJ. Li, R. Lipson, in *ELECTRONIC, PHOTONIC, PLASMONIC, PHONONIC AND MAGNETIC PROPERTIES OF NANOMATERIALS, Vol. 1590*, AIP Publishing, **2014**, pp. 119.

[105] T. Watanabe, H. Kawasaki, T. Yonezawa, R. Arakawa,Surface-assisted laser desorption/ionization mass spectrometry (SALDI-MS) of low molecular weight organic compounds and synthetic polymers using zinc oxide (ZnO) nanoparticles *Journal of mass spectrometry* **2008**, *43*, 1063.

[106] K. H. Lee, C. K. Chiang, Z. H. Lin, H. T. Chang,Determining enediol compounds in tea using surface-assisted laser desorption/ionization mass spectrometry with titanium dioxide nanoparticle matrices *Rapid communications in mass spectrometry* **2007**, *21*, 2023.

[107] P. Lorkiewicz, M. C. Yappert,Titania microparticles and nanoparticles as matrixes for in vitro and in situ analysis of small molecules by MALDI-MS *Analytical chemistry* **2009**, *81*, 6596.

[108] Y. Gholipour, S. L. Giudicessi, H. Nonami, R. Erra-Balsells,Diamond, titanium dioxide, titanium silicon oxide, and barium strontium titanium oxide nanoparticles as matrixes for direct matrix-assisted laser desorption/ionization mass spectrometry analysis of carbohydrates in plant tissues *Analytical chemistry* **2010**, *82*, 5518.

[109] C.-Y. Lo, J.-Y. Lin, W.-Y. Chen, C.-T. Chen, Y.-C. Chen,Surface-assisted laser desorption/ionization mass spectrometry on titania nanotube arrays *Journal of the American Society for Mass Spectrometry* **2008**, *19*, 1014.

[110] K.-Y. Wang, S.-A. Chuang, P.-C. Lin, L.-S. Huang, S.-H. Chen, S. Ouarda, W.-H. Pan, P.-Y. Lee, C.-C. Lin, Y.-J. Chen,Multiplexed immunoassay: quantitation and profiling of serum biomarkers using magnetic nanoprobes and MALDI-TOF MS *Analytical chemistry* **2008**, *80*, 6159.

[111] X. Kong, L. Huang, C.-M. Hsu, W.-H. Chen, C.-C. Han, H.-C. Chang,High-affinity capture of proteins by diamond nanoparticles for mass spectrometric analysis *Analytical chemistry* **2005**, *77*, 259.

[112] S. Cha, E. S. Yeung,Colloidal graphite-assisted laser desorption/ionization mass spectrometry and MS n of small molecules. 1. Imaging of cerebrosides directly from rat brain tissue *Analytical chemistry* **2007**, *79*, 2373.

[113] C. Shi, J. Meng, C. Deng,Enrichment and detection of small molecules using magnetic graphene as an adsorbent and a novel matrix of MALDI-TOF-MS *Chem. Commun.* **2012**, *48*, 2418.

[114] C. Shi, J. Meng, C. Deng,Facile synthesis of magnetic graphene and carbon nanotube composites as a novel matrix and adsorbent for enrichment and detection of small molecules by MALDI-TOF MS *Journal of Materials Chemistry* **2012**, *22*, 20778.

[115] J. Liu, Y. Liu, M. Gao, X. Zhang,High throughput detection of tetracycline residues in milk using graphene or graphene oxide as MALDI-TOF MS matrix *Journal of the American Society for Mass Spectrometry* **2012**, *23*, 1424.

[116] Y. Liu, J. Liu, P. Yin, M. Gao, C. Deng, X. Zhang,High throughput identification of components from traditional Chinese medicine herbs by utilizing graphene or graphene oxide as MALDI-TOF-MS matrix *Journal of Mass Spectrometry* **2011**, *46*, 804.

[117] J. Lee, Y.-K. Kim, D.-H. Min,Laser desorption/ionization mass spectrometric assay for phospholipase activity based on graphene oxide/carbon nanotube double-layer films *Journal of the American Chemical Society* **2010**, *132*, 14714.

[118] X. Zhou, Y. Wei, Q. He, F. Boey, Q. Zhang, H. Zhang,Reduced graphene oxide films used as matrix of MALDI-TOF-MS for detection of octachlorodibenzo-p-dioxin *Chem. Commun.* **2010**, *46*, 6974.

[119] T. R. Northen, H.-K. Woo, M. T. Northen, A. Nordström, W. Uritboonthail, K. L. Turner, G. Siuzdak,High surface area of porous silicon drives desorption of intact molecules *Journal of the American Society for Mass Spectrometry* **2007**, *18*, 1945.

[120] Y. Wada, T. Yanagishita, H. Masuda,Ordered porous alumina geometries and surface metals for surface-assisted laser desorption/ionization of biomolecules: possible mechanistic implications of metal surface melting *Analytical chemistry* **2007**, *79*, 9122.

[121] A. R. Korte, G. B. Yagnik, A. D. Feenstra, Y. J. Lee, in *BMultiplex MALDI-MS imaging of plant metabolites using a hybrid MS systemook Multiplex MALDI-MS imaging of plant metabolites using a hybrid MS system*, Springer, **2015**, pp. 49.

[122] A. R. Korte, Y. J. Lee,MALDI-MS analysis and imaging of small molecule metabolites with 1, 5-diaminonaphthalene (DAN) *Journal of Mass Spectrometry* **2014**, *49*, 737.

[123] AuHandbook of carbon, graphite, diamonds and fullerenes: processing, properties and applicationsthor, *Handbook of carbon, graphite, diamonds and fullerenes: processing, properties and applications*, William Andrew, **2012**.

[124] AuCarbon nanomaterialsthor, *Carbon nanomaterials*, CRC Press, **2013**.

[125] D. Reitze, H. Ahn, M. Downer,Optical properties of liquid carbon measured by femtosecond spectroscopy *Physical Review B* **1992**, *45*, 2677.

[126] A. O. Govorov, H. H. Richardson,Generating heat with metal nanoparticles *Nano today* **2007**, *2*, 30.

[127] H. H. Richardson, Z. N. Hickman, A. O. Govorov, A. C. Thomas, W. Zhang, M. E. Kordesch,Thermooptical properties of gold nanoparticles embedded in ice: characterization of heat generation and melting *Nano letters* **2006**, *6*, 783.

[128] E. Marin,Characteristic dimensions for heat transfer *Latin-American Journal of Physics Education* **2010**, *4*, 56.

[129] K. Y. Chu, S. Lee, M.-T. Tsai, I.-C. Lu, Y. A. Dyakov, Y. H. Lai, Y.-T. Lee, C.-K. Ni,Thermal proton transfer reactions in ultraviolet matrix-assisted laser desorption/ionization *Journal of The American Society for Mass Spectrometry* **2014**, *25*, 310.

[130] K. Dreisewerd,The desorption process in MALDI *Chemical reviews* **2003**, *103*, 395.

[131] AuCRC handbook of chemistry and physicsthor, *CRC handbook of chemistry and physics*, CRC press, **2014**.

[132] M. B. Johansson, G. Baldissera, I. Valyukh, C. Persson, H. Arwin, G. A. Niklasson, L. Österlund,Electronic and optical properties of nanocrystalline WO3 thin films studied by optical spectroscopy and density functional calculations *Journal of Physics: Condensed Matter* **2013**, *25*, 205502.

[133] A. Schlegel, S. Alvarado, P. Wachter,Optical properties of magnetite (Fe3O4) *Journal of Physics C: Solid State Physics* **1979**, *12*, 1157.

[134] J. Muth, R. Kolbas, A. Sharma, S. Oktyabrsky, J. Narayan,Excitonic structure and absorption coefficient measurements of ZnO single crystal epitaxial films deposited by pulsed laser deposition *Journal of Applied Physics* **1999**, *85*, 7884.

[135] M.-S. Kim, K.-G. Yim, J.-S. Son, J.-Y. Leem,Effects of Al concentration on structural and optical properties of Al-doped ZnO thin films *Bulletin of the Korean Chemical Society* **2012**, *33*, 1235.

[136] F. R. Chowdhury, S. Choudhury, F. Hasan, T. Begum,Optical properties of undoped and indium-doped tin oxide thin films *Journal of Bangladesh Academy of Sciences* **2011**, *35*, 99.

[137] C. Walter, C. Hertzler, P. Devynck, G. Smith, J. Peterson,Photodetachment of WO− 3: The electron affinity of WO3 *The Journal of chemical physics* **1991**, *95*, 824.

[138] M. Islam, M. Hakim,Electron affinity and work function of polycrystalline SnO 2 thin film *Journal of materials science letters* **1986**, *5*, 63.

[139] J. I. Sohn, S. N. Cha, B. G. Song, S. Lee, S. M. Kim, J. Ku, H. J. Kim, Y. J. Park, B. L. Choi, Z. L. Wang,Engineering of efficiency limiting free carriers and an interfacial energy barrier for an enhancing piezoelectric generation *Energy & Environmental Science* **2013**, *6*, 97.

[140] X. Wang, G. I. Koleilat, J. Tang, H. Liu, I. J. Kramer, R. Debnath, L. Brzozowski, D. A. R. Barkhouse, L. Levina, S. Hoogland,Tandem colloidal quantum dot solar cells employing a graded recombination layer *Nature Photonics* **2011**, *5*, 480.

[141] H. Wang, Y. Xu, M. Goto, Y. Tanaka, M. Yamazaki, A. Kasahara, M. Tosa,Thermal conductivity measurement of tungsten oxide nanoscale thin films *Materials transactions* **2006**, *47*, 1894.

[142] W. Gajewski, P. Achatz, O. A. Williams, K. Haenen, E. Bustarret, M. Stutzmann, J. A. Garrido,Electronic and optical properties of boron-doped nanocrystalline diamond films *Physical Review B* **2009**, *79*, 045206.

[143] E. Ekimov, V. Ralchenko, A. Popovich,Synthesis of superconducting boron-doped diamond compacts with high elastic moduli and thermal stability *Diamond and Related Materials* **2014**, *50*, 15.

[144] S. N. Jackson, K. Baldwin, L. Muller, V. M. Womack, J. A. Schultz, C. Balaban, A. S. Woods,Imaging of lipids in rat heart by MALDI-MS with silver nanoparticles *Analytical and bioanalytical chemistry* **2014**, *406*, 1377.

[145] M. Dufresne, A. l. Thomas, J. Breault-Turcot, J.-F. o. Masson, P. Chaurand,Silver-assisted laser desorption ionization for high spatial resolution imaging mass spectrometry of olefins from thin tissue sections *Analytical chemistry* **2013**, *85*, 3318.

[146] H. W. Tang, M. Y. M. Wong, W. Lam, Y. C. Cheng, C. M. Che, K. M. Ng,Molecular histology analysis by matrix-assisted laser desorption/ionization imaging mass spectrometry using gold nanoparticles as matrix *Rapid Communications in Mass Spectrometry* **2011**, *25*, 3690.

[147] H.-W. Tang, M. Y.-M. Wong, S. L.-F. Chan, C.-M. Che, K.-M. Ng,Molecular imaging of banknote and questioned document using solvent-free gold nanoparticle-assisted laser desorption/ionization imaging mass spectrometry *Analytical chemistry* **2010**, *83*, 453.